Programming Hierarchical Self-assembly of Anisotropic Colloids

by

Daniel Morphew

A thesis submitted to the
University of Birmingham
for the degree of
DOCTOR OF PHILOSOPHY

School of Chemistry
College of Engineering and Physical Sciences
University of Birmingham
January 2018

Abstract

Colloidal self-assembly promises to be an elegant and efficient route to the bottom-up fabrication of 3-dimensional structures due to the scope for tuning the colloid-colloid interactions. Programming hierarchical schemes for colloid self-assembly has the potential to widen structural diversity and mimic biological complexity. However, it remains a grand challenge to bridge hierarchies of multiple length- and time-scales associated with the structure and dynamics along complex self-assembly pathways.

This thesis employs a variety of computational techniques to address this challenge *in silico*, programming colloidal self-assembly for structural hierarchy in close connection with contemporary experimental research. In a series of studies, the self-assembly of designer charge-stabilised colloidal magnetic particles into a number of supracolloidal polyhedra for size-selected clusters is demonstrated, each displaying a remarkable two-level structural hierarchy. The design space supports self-assembled polyhedra of very different morphologies, namely tubular and hollow spheroidal structures, for which the dominant pathways for self-assembly are elucidated, revealing two distinct mechanisms. Here, it is found that for a staged assembly pathway the structure, which derives the strongest energetic stability from the first stage and the weakest from the second stage, is most kinetically accessible.

Stemming from these findings, a generic design principle exploiting a hierarchy of interaction strengths is introduced. This design principle is subsequently employed to demonstrate the hierarchical self-assembly of triblock patchy colloidal particles into a variety of colloidal crystals via distinct clusters of uniform shape and size, so-called "colloidal molecules". Furthermore, this design framework exhibits a novel bottom-up route to the fabrication of cubic diamond colloidal crystals, which despite being much sought after for their attractive photonic applications, have remained elusive.

Acknowledgments

First, I must convey my sincerest thanks to my Ph.D. supervisor Dr Dwaipayan Chakrabarti. Dr Chakrabarti's unwavering enthusiasm for all aspects scientific research is truly infectious and without his insight, patience and guidance the body of work presented in this thesis would not have been possible. In addition, particular thanks go for the innumerable hours he has given up to discuss all topics – scientific, technical, philosophical and sports related throughout my time here at the University of Birmingham. I regard myself as truly fortunate to have been his first Ph.D. student.

I must also extend my sincere gratitude to my second supervisor Prof. Roy Johnston whose wisdom and academic experience I have greatly benefited from. Furthermore, I would like to thank the various editions of the Chakrabarti and Johnston groups, who have provided a stimulating and entertaining work environment. In particular, I would like to thank Dr Jack Davis, Dr Lewis Smeeton and Dr Sridhar Neelamraju whose good humour and friendship has enriched my time spent in Birmingham. I would also like to thank James Shaw and Christopher Avins for their collaborative efforts with regard to Chapter 6. Support from the Engineering and Physical Sciences Research Council of the UK and the University of Birmingham for funding and BlueBear for HPC facilities is gratefully acknowledged.

I would also like to thank my parents Ian and Marie for their constant encouragement and support throughout my many years of study. Finally, I thank Becky for her love, positivity and understanding.

Contents

List of Figures

Publications

- Hierarchical self-assembly of colloidal magnetic particles into reconfigurable spherical structures, D. Morphew and D. Chakrabarti, *Nanoscale*, 2015, **18**, 8343-8350.

- Supracolloidal reconfigurable polyhedra via hierarchical self-assembly, D. Morphew and D. Chakrabarti, *Soft Matter*, 2016, **12**, 9633-9640.

- Clusters of anisotropic colloidal particles: from colloidal molecules to supracolloidal structures, D. Morphew and D. Chakrabarti, *Curr. Opin. Colloid Interface Sci.*, 2017, **30**, 70-80.

- Programming hierarchical self-assembly of colloids: matching stability and accessibility, D. Morphew and D. Chakrabarti, *Submitted for Publication*, 2018.

- Programming hierarchical self-assembly of patchy particles into colloidal crystals via colloidal molecules, D. Morphew, J. Shaw, C. Avins and D. Chakrabarti, *ACS Nano*, 2018, **12**, 2355-2364.

Chapter 1

Introduction

A colloidal dispersion consists of particles, whose size typically ranges from a few nanometres to a few microns in one of the dimensions, dispersed in the so-called continuous phase. The molecules that comprise the continuous phase are much smaller in size than the dispersed particles, often referred to as colloidal particles, or simply colloids for brevity. The size of the colloidal particles are large enough for each individual particle to be easily visualised using optical microscopy, while still small enough to undergo Brownian motion. Traditionally, colloidal particles have been spherical, experiencing isotropic interparticle interactions. Such colloidal systems have served as useful model systems to study crystallisation, gelation and glass transition,[1] where the colloidal particles are viewed as "big atoms".[2]

Recent advances in synthetic techniques have made a library of colloidal particles with well-defined anisotropic shape and/or anisotropic interparticle interactions available.[3–7] Specificity in the interparticle interactions can also be realised via DNA-mediated binding.[8] A key feature of these colloidal particles that make them attractive building blocks for novel self-assembled materials is that the interparticle interactions can be tuned. The term self-assembly refers to the spontaneous emergence of an ordered structure or pattern from its components without manual intervention.[9] The illustrations of self-assembly are ubiquitous in nature and found at all length scales.[9] In particular, colloidal self-assembly has shown enormous potential as an elegant and efficient bottom-up route to the fabrication of novel structures, especially in 3-dimensions – from clusters to crystals.[3]

Another salient feature of colloidal particles, distinct from atoms, is that their length scale is comparable to the wavelength of visible light. This feature makes colloidal self-assembly

especially attractive for engineering optical properties. In this context, certain colloidal crystals have been at the center of attraction once it was demonstrated that diamond, pyrochlore and other percolating lattices would possess a full omni-directional photonic band gap.[10–14]

A large body of work in recent years has focused on colloidal clusters – finite-size systems of microparticles – as "colloidal molecules" have come to prominence in colloid science alongside the traditional picture, where colloidal particles are viewed as "big atoms".[2,15] "Colloidal molecules" refer to small clusters of colloidal particles, which mimic the symmetry of molecular structures.[15] While colloidal molecules, as molecular analogs on a different length scale, have drawn attention, colloidal clusters are of fundamental and practical interest in their own right. From a fundamental point of view, colloidal clusters provide an attractive platform for investigating the structure, thermodynamics, and kinetics of finite-size systems on the mesoscale.[16] Colloidal clusters have also stimulated interest for their exotic optical properties.[17–19] For example, colloidal clusters can be used as building blocks for isotropic optical metamaterials, known as metafluids, capable of exhibiting optical properties previously non-existent in nature.[17,20,21] Colloidal clusters have also been at the focal point because of remarkable examples of the self-assembly of anisotropic colloidal particles into finite supracolloidal structures.

In the following, a brief overview of the state of the art of colloidal self-assembly is presented before the scope of this thesis is outlined. Since the focus is on *programming* colloidal self-assembly into certain target structures,[8,22] the existing literature is largely presented around certain classes of self-assembled structures, both finite and periodic, with an emphasis on understanding the interplay between the colloidal interactions driving the observed self-assembly. The connections between experimental and computational studies are highlighted wherever appropriate.

1.1 Colloidal Molecules: Mimicking Molecular Structures

In this section a brief historical account describing how the concept of "colloidal molecules" has evolved since its introduction is presented, making reference to clusters of isotropic colloidal particles for the sake of completeness. In one of the early studies of colloidal clusters, Pine

and co-workers demonstrated a route to small colloidal clusters by evaporating oil droplets suspended in water, with equal-sized microspheres adsorbed to the surface of the oil droplets.[23] The packing of $N = 2 - 15$ microspheres, driven by capillary forces, resulted in a variety of polyhedra, including some with fivefold rotational symmetry. Many of these polyhedra were distinct from the polytetrahedral structures typically identified as the global minima on the potential energy surface for small clusters bound by longer-ranged isotropic potentials.[24] The study reported that the packing of the microspheres in this case was governed by the minimisation of the second moment of the mass distribution,[23] which influenced the shape and symmetry of these clusters. The term "colloidal molecule" was coined to refer to these small colloidal clusters mimicking molecular geometry.[15]

A colloidal suspension where depletion attraction promotes aggregation and screened electrostatic repulsion prevents coagulation has gained considerable attention in the context of cluster formation.[25–29] Manoharan and co-workers mapped the free energy landscape in experiments for small colloidal clusters where both depletion attraction and screened electrostatic repulsion are short ranged.[28] In the presence of short-ranged interactions, the energy contribution to the stability is essentially governed by the number of nearest neighbour contacts. The experiments revealed that of the clusters with equal numbers of nearest neighbour contacts, highly symmetric clusters were relatively disfavoured (see **Figure 1.1a**) – a result interpreted theoretically by symmetry considerations, which take into account the entropy cost for highly symmetric clusters.[28] Wales presented the disconnectivity graph representation of the potential energy landscape as well as the free energy landscape for small colloidal clusters, using a short-ranged Morse potential to model the depletion interaction and normal mode analysis to obtain free energies within the harmonic approximation (**Figure 1.1b**).[30] The occupation probabilities calculated at a reduced temperature were in agreement with those reported by Meng *et al.* within a few percent for the Morse range parameter $q = 30$.[28,30] These small colloidal clusters bound by relatively weak interparticle interactions at equilibrium, when conceived as "colloidal molecules", present a picture where the particles are viewed as atoms, the attractive interactions between them as bonds, and the different structures observed at equilibrium as isomers.[31]

In line with this picture, Malins *et al.* considered the yield of clusters of different structures

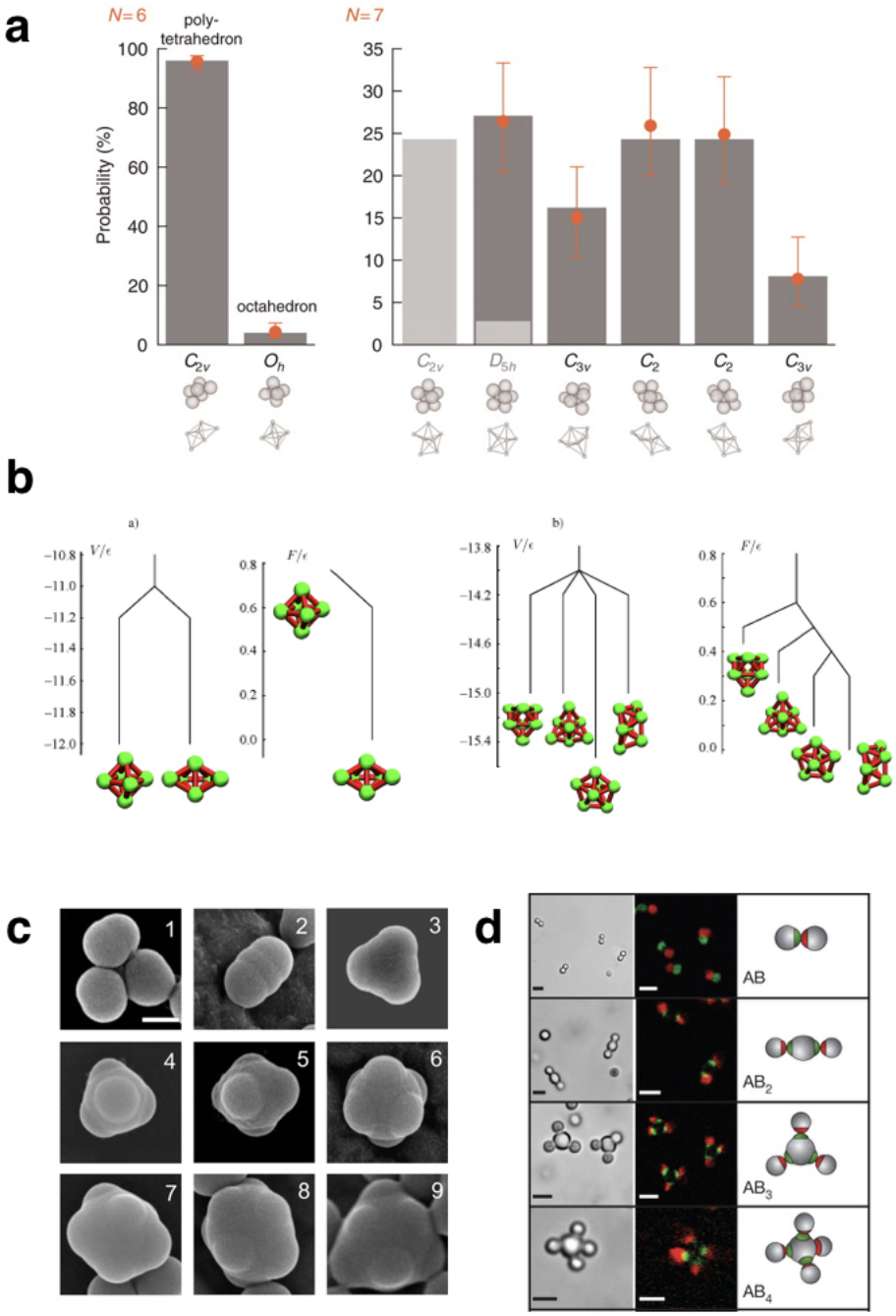

Figure 1.1: **a**. Comparison of probabilities for different structures as observed in experiments (orange dots) and as predicted by theoretical calculations (grey bars) for clusters of size $N = 6$ and 7.[28] Reprinted with permission from AAAS. **b**. Potential (V) and free energy (F), calculated at the reduced temperature of 0.25, disconnectivity graphs for colloidal clusters, bound by the Morse potential with the range parameter $q = 30$ of size $N = 6$ and 7.[30] Reproduced with permission from John Wiley and Sons. **c**. Scanning electron micrographs of colloidal molecules for $N = 1$ to $N = 9$ created by merging liquid protrusions.[32] Copyright (2009) American Chemical Society. **d**. Colloidal molecules self-assembled from patchy particles, as shown in bright-field (left panels), confocal fluorescent (middle panels), and schematic images (right panels).[33] Reprinted with permission from Macmillan Publishers Ltd: Nature, copyright (2012).

as a function of the strength of the interactions in a Brownian dynamics simulation study.[27] They employed the traditional one-component description to study small clusters of ($N = 3-7$, 10, 13) colloidal particles in the presence of a short-ranged attraction and a weak long-ranged electrostatic repulsion. As the strength of the attractive interaction was increased, the average bond lifetime approached the simulation run time, making the system non-ergodic on that time-scale. For $N \geq 7$, a lower yield of the structures that maximise the number of nearest-neighbour contacts were observed in the non-ergodic regime, where it was argued that geometric frustration arising from metastable structures played a significant role and resulted in kinetic trapping. Colloidal clusters thus also serve as a useful test bed to investigate the statistical mechanics of finite-size systems.[29,34–36]

Recent progress in the synthesis of colloidal molecules suggests that they themselves can serve as building blocks with anisotropy attributes for colloidal superstructures.[32,37–41] Kraft *et al.* reported on the synthesis of colloidal molecules with well-controlled shape and tunable patchiness, utilising a variation of the seeded polymerisation technique (**Figure 1.1c**).[32] This method exploits the assembly of cross-linked polystyrene spheres with a liquid protrusion by coalescence of the liquid protrusions. Subsequently, control over the synthesis of colloidal molecules with well-defined bond angles was achieved by adjusting the size of the liquid protrusion.[37] The authors of the latter study concluded that the unique shape was due to a polymerisation-induced aggregation of the seeds inside the liquid droplets.

Malins *et al.* suggested more sophisticated means beyond the spherically symmetric microspheres, such as 'patchy particles', for fabrication of complex colloidal molecules in good yields.[27] In a recent study, patchy colloidal particles with chemically distinct surface patches imitating hybridised atomic orbitals were obtained from the so-called 'minimal-moment' clusters with reproducible symmetries.[33] The patches were functionalised with DNA having single-stranded sticky ends to realise specificity as well as directionality in the interparticle interactions. Such interactions were found to drive the self-assembly of the colloidal particles into "colloidal molecules" with triangular, tetrahedral and other bonding symmetries (**Figure 1.1d**).[33]

1.2 Clusters of Anisotropic Colloidal Particles

Here, we cover a select group of finite-sized examples of colloidal self-assembly, predominantly focusing on anisotropic colloidal particles. This section is organised around certain classes of finite supracolloidal structures, which have appeared as recurrent themes in studies of colloidal clusters, as opposed to focusing on specific types of anisotropic colloidal building blocks. Such an organisation lays a platform for us to highlight the critical role of the intriguing interplay of colloidal interactions, often involving more than one anisotropy attribute,[3] in driving colloidal self-assembly. In this review we restrict ourselves to colloidal particles with size larger than a few tens of nanometres, where the non-additivity of various interparticle interactions is not important.[42] The examples included here are by no means exhaustive and there are recent studies,[43–47] which have notably advanced the field of colloidal clusters, but fall beyond the scope of the work presented here, given the focus on anisotropic colloidal particles.

1.2.1 Micellar Analogues

Janus colloidal particles, named after the two-faced Roman god, can be viewed as a special type of patchy colloidal particles with different surface chemistry on their opposing hemispheres.[48] Amphiphilic Janus colloidal particles, hydrophobic on one hemisphere and charged on the other, have received attention for their ability to form micellar structures. Such Janus particles, albeit rigid for all practical purposes, mimic molecular amphiphiles, such as surfactants, on the mesoscopic scale. In an early study with amphiphilic Janus particles, Granick and co-workers observed the formation of extended worm-like rings via the link-up of small compact clusters, whose structures were analogous to micellar shapes, as the electrostatic screening was enhanced in an aqueous medium by increasing the salt concentration (see **Figure 1.2a**).[49] More recently, experimental fabrication of patchy colloidal particles with one patch offered a model system to study self-assembly into clusters that resemble surfactant micelles.[50] In this study, Kraft *et al.* showed curved, smooth patches on rough colloidal particles to be exclusively attractive due to their different overlap volumes. The patchy particles in this case resembled dumbbells, which had one spherical lobe with a smooth surface while the other spherical lobe had a rough surface. The self-assembly of these particles resulted in finite clusters reminiscent of micelles (**Figure 1.2b**). The cluster size distribution simulated starting from a homogeneous state was found to

be in good agreement with those observed in experiments.[50]

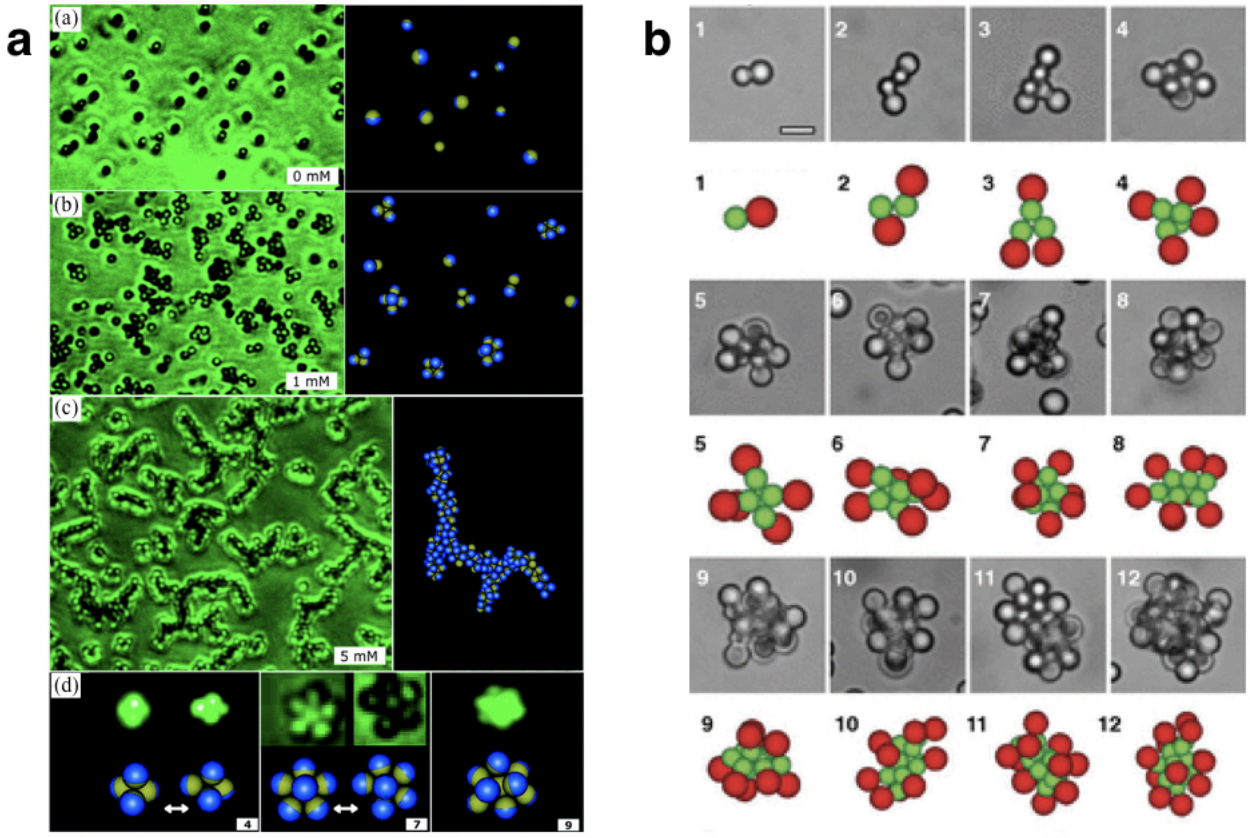

Figure 1.2: **a**. Clusters of various sizes and shapes formed via the self-assembly of amphiphilic Janus colloidal particles at different salt concentrations. The images with green background represent epifluorescence experiments and those with black background are from Monte Carlo simulations, showing cluster formation as the salt concentration increased from (a) to (c). The panel (d) highlights that the structures dynamically interconvert between different shapes as observed both in experiments and simulations. This figure was adapted with permission.[49] Copyright (2008) American Chemical Society. **b**. Typical structures observed for one-patch colloidal particles in experiments (upper rows with grey background) and simulations (lower rows with white background), showing the self-assembly into finite structures resembling micelles; in experiments and simulations,the smaller attractive sides with a smooth surface are located at the interior of the clusters.[50] Copyright (2012) National Academy of Sciences.

Drawing inspiration from the experimental study by Hong *et al.*[49] a simple model representing these Janus particles has been investigated by Sciortino and co-workers in periodic systems,[51,52] for which a cluster phase was observed. The model, introduced by Kern and Frenkel[53] represents Janus particles in terms of hard-core particles with two hemispheres that are attractive and repulsive respectively. A square-well potential describes an attractive patch-patch interaction whenever the attractive hemispheres on two particles face each other. For a relatively large attraction range, a cluster phase of micelles formed at low temperatures and the phase diagram included a colloid-poor (gas) and colloid-rich (liquid) demixing region, which

was increasingly suppressed upon cooling due to the formation of micelles in the gas phase.[51] When the phase behaviour of model colloidal dumbbells described by two identical tangent hard spheres, with the first one surrounded by an attractive square-well interaction, was studied, it was observed that a larger hard-sphere site promoted the formation of clusters, whereas a gas-liquid phase separation took place in the case of a smaller hard-sphere site.[54]

1.2.2 Supracolloidal Chirality

A common thread running through a number of studies in recent years has been the design and control of emergent supracolloidal chirality.[55–60] The term 'chirality' refers to handedness and is a geometric attribute associated with non-superimposable mirror images. Homochirality of biological molecules underpins many spectacular examples of the structure-function relationship in living matter. Zerrouki *et al.* employed asymmetric colloidal silica dumbbells, linked by a paramagnetic ferrofluid belt at the waist, in the presence of an applied magnetic field to realise two competing length scales for interactions, seemingly present in DNA, as a route to chiral colloidal clusters.[55] In the presence of a magnetic field, a linear chain was observed with symmetric dumbbells, while the asymmetry of the dumbbell, *i.e.* the difference in size between its two spherical lobes, forced the chain to coil when this size ratio was between 2 and 3 (**Figure 1.3a**).[55] Drawing motivation from this experimental work, Chakrabarti *et al.* devised a general strategy for the programmed assembly of helical ground state structures with different achiral building blocks, underpinning the physics of emergent chirality in the cases considered in their computational study.[56] This study demonstrated how chirality could emerge from an interplay between two competing length scales for anisotropic interactions, realised, perhaps in the simplest form, with soft oblate ellipsoids of revolution.[56] Using a rare-event simulation technique, the fastest pathway for the reversal of handedness was characterised for a helix assembled from asymmetric dipolar dumbbells in the presence of an external field.[57] The mechanism for switching of handedness involved a boundary between two segments of opposite handedness, which was called a defect, propagating along the helical structure from one end to the other through a sequence of hopping events supported by highly cooperative rearrangements.[57] A more recent computational study by Wales and co-workers demonstrated control over the pitch length of a helical superstructure, obtained via directed self-assembly

of charge-stabilised colloidal magnetic dumbbells in the presence of an applied magnetic field. The study shows that the pitch length can be controlled considerably by varying the salt concentration of the medium, thus modulating the electrostatic screening (see **Figure 1.3b**).[60]

In their experiments, Granick and co-workers exploited the salt concentration as a control parameter to induce the self-assembly of Janus colloidal particles having hydrophobic attractions on one hemisphere and electrostatic repulsions on the other, and elucidated kinetic pathways for self-assembly into supracolloidal architectures and their isomerisation.[58] In particular, they reported the formation of the Bernal spirals[61] also known as triple helices, which are three-stranded helices composed of a chain of face-sharing tetrahedra, as kinetically favoured structures (**Figure 1.3c**).[58] The self-assembly pathway was found to involve the formation of kinetically favoured capped trigonal bipyramidal clusters, which fused together to form the supracolloidal triple helix. The Bernal spiral is a chiral architecture; interestingly, the experiments observed a spontaneous switching of handedness occurring occasionally. The pathway for chirality switching was observed to involve an intermediate structure in which one particle had seven nearest neighbours.[58]

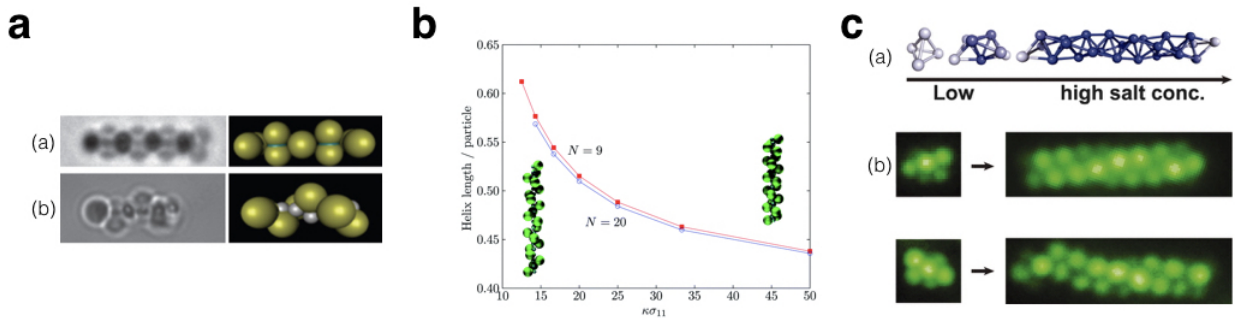

Figure 1.3: **a.** Optical microscopy images and their corresponding schematic representations, showing emergent helicity through the interplay between steric and magnetic interactions, experimentally realised by magnetic dumbbells in the presence of an external magnetic field: (a) a chain formed by symmetric dumbbells; (b) a helical structure formed by asymmetric dumbbells.[55] Reprinted with permission from Macmillan Publishers Ltd: Nature, copyright (2008). **b.** A plot showing the helix pitch length as the inverse Debye screening length was varied for finite supracolloidal helices, obtained via directed self-assembly of charge-stabilised colloidal magnetic dumbbells in the presence of an applied magnetic field, for two different cluster sizes.[60] Reproduced with permission from The Royal Society of Chemistry. **c.** A geometrical representation of the growth of a triple helix (a) and fluorescence images of the chiral structures (both right- and left-handed) as observed in experiments with spherical Janus colloidal particles (b). Triple helices are formed at higher salt concentrations.[58] Reprinted with permission from AAAS.

In a subsequent computational study by Morgan *et al.*[59] a minimalist design rule was derived for thermodynamically favoured Bernal spirals using patchy particles. These colloidal building blocks involved two different types of attractive surface sites, described as complementary patches and antipatches, such that a patch interacted only with antipatches and vice versa. A tailored spatial arrangement for three pairs of patches and antipatches, deduced from the geometry of the Bernal spiral, was shown to produce thermodynamically favoured Bernal spirals. By systematic removal of patches, the designer patchy colloidal particles with only one patch-antipatch pair offset by about 10° from the directly opposite spatial arrangement were then shown to support Bernal spirals as the ground state structures.[59] This minimal design rule presents a realistic target for state-of-the-art experimental fabrication.

1.2.3 Hollow Spheroidal and Tubular Structures

Hollow spheroidal structures at different length scales have many practical applications, especially in drug delivery, predominantly because of their ability to encapsulate guests and deliver cargoes[62] and thus serve as attractive targets for colloidal self-assembly.[63–68] In seminal early work, microcapsules were fabricated by the self-assembly of colloidal particles onto the interface of emulsion droplets.[63] Several studies of targeted self-assembly into hollow spheroidal structures in the absence of a template have drawn motivation from fascinating examples of viral capsid assembly,[64–66,68] which results in a remarkable structural hierarchy via protein subunits.[69] Early models of patchy particles were used as a minimal representation of globular proteins for numerical studies of protein crystallisation.[53,70] Self-assembly into a range of platonic solids has been explored with such models to achieve the control and fidelity of virus capsid assembly in synthetic systems by Doye, Louis and co-workers[64,65] who identify global minima for clusters of $N = 12$, 24, 36 patchy particles, each decorated with five patches, illustrating the propensity to form hollow icosahedra (**Figure 1.4d**). This study found an optimal patch width to be a crucial parameter to strike a balance between structural specificity and kinetic accessibility.[64] It is relevant to note that a recent study has investigated dense packings of up to $N = 60$ polyhedral particles in spherical confinement.[71] The interplay between shape anisotropy of particles and isotropic three-dimensional confinement resulted in a wide variety of symmetries and structures, demonstrating the effects of spherical confinement. For many N

values, icosahedra and dodecahedra form clusters, which surprisingly include layers of optimal spherical codes.[72,73]

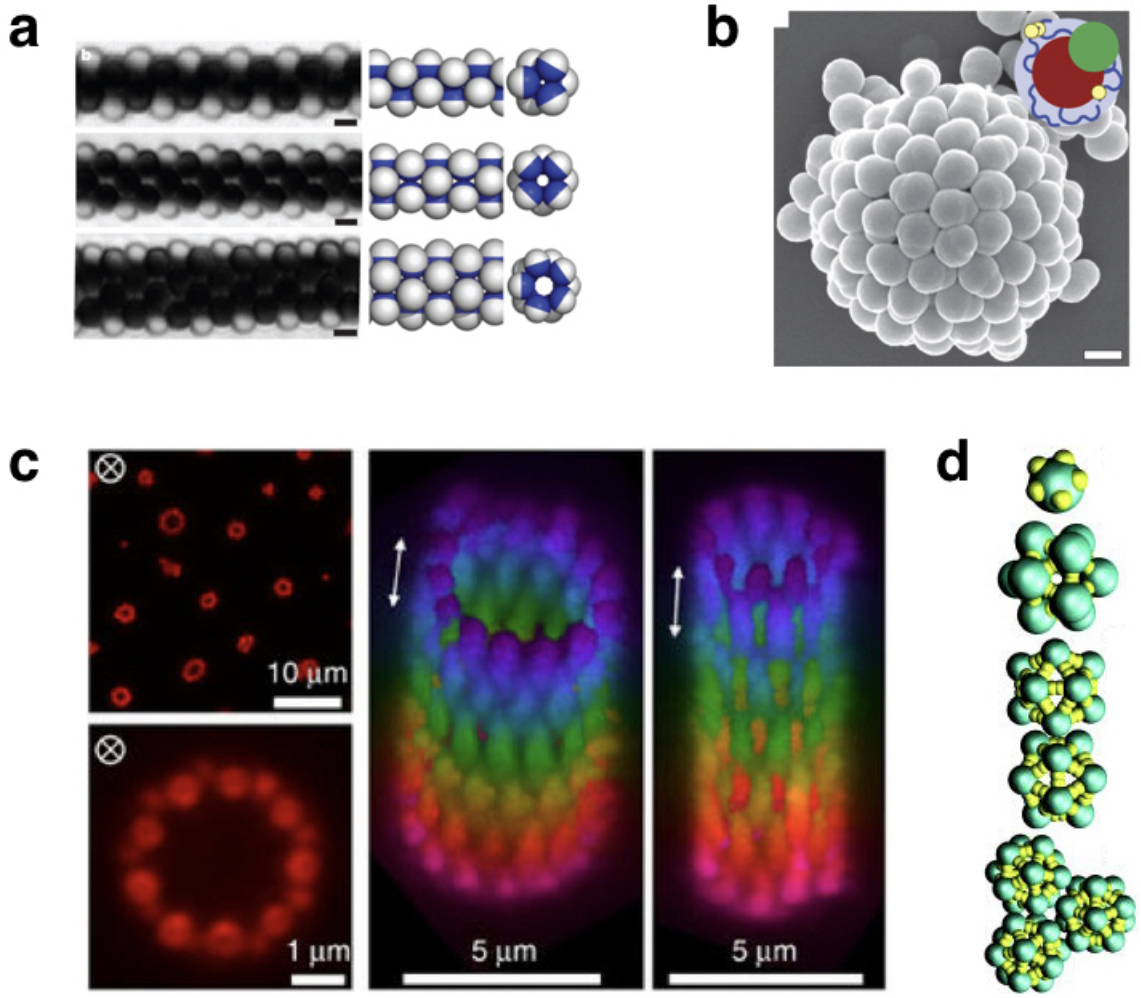

Figure 1.4: **a.** Microtubes formed by self-organisation of magnetic Janus particles in the presence of a precessing magnetic field: (left) observed images and (right) corresponding models (side and end views) of microtubes parallel to the precession axis.[74] Reprinted with permission from Macmillan Publishers Ltd: Nature, copyright (2012). **b.** The scanning electron microscopy (SEM) image of microcapsules formed via self-assembly of deformable, anisotropic, mutually attractive colloidal particles. A schematic representation of the colloidal building block, consisting of a core (red) with hydrophilic (blue) and hydrophobic (yellow) moieties and a rigid protrusion (green).[67] Reprinted by permission from Macmillan Publishers Ltd: Nature, copyright (2008). **c.** 2D images and 3D reconstructions of tubular structures formed via self-assembly of colloidal particles with a prolate ellipsoidal shape when subjected to an alternating electric field.[75] Reprinted under a Creative Commons Attribution 4.0 International License. **d.** A five-patch colloidal particle and the global minima for clusters of $N = 12$, 24 and 36 such particles, showing the formation of hollow icosahedra.[64] Reprinted with the permission of AIP Publishing.

Evers *et al.* recently reported a fascinating realisation of hollow microcapsules via self-assembly of snowman-shaped colloidal particles, which combined shape anisotropy, attractive

interaction and deformability.[67] The particles consisted of a deformable core with a hydrophobic polystyrene-rich interior and a hydrophilic poly(acrylic acid)-rich outer layer onto which a rigid protrusion was grown by swelling with additional styrene. The presence of hydrophobic polystyrene groups also in the outer layer imparted mutual attraction to these particles. Evers *et al.* demonstrated that all three attributes were necessary for the colloidal building blocks they synthesised to self-assemble into microcapsules, which they observed using both scanning electron microscopy and optical microscopy (see **Figure 1.4b**).[67]

A variety of colloidal self-assembly routes have recently shown to lead to finite tubular structures.[68,74,75] By applying a precessing magnetic field, where the precession angle was used as the control parameter, Yan *et al.* demonstrated the self-organisation of magnetic Janus particles into microtubes (**Figure 1.4a**).[74] In this study, the colloidal particles were observed to rotate and oscillate continuously, but their motion was synchronised. In this case, the formation of the microtubes, which can be viewed as staggered stacks of regular polygons, followed a nucleation-and-growth scheme.[74] In another route, Crassous *et al.* demonstrated the self-assembly of colloidal particles with a prolate ellipsoidal shape into regular tubular structures when subjected to an alternating electric field (**Figure 1.4c**).[75] Their experimental state diagram shows that tubular structures were formed for moderate values of the aspect ratio and relatively large values for the electric field strength.[75] The tubes were found to have a highly regular structure with a circular cross-section, single-particle wall and a periodic arrangement of the aligned particles. The study identified the interplay between the shape anisotropy and the polarisation effects to be the key factor for the hollow tubes with curved surfaces to emerge via self-assembly.

1.3 Colloidal Crystals

Colloidal crystals are of principal interest for programmed colloidal self-assembly. The potential applications of colloidal crystals, in particular the photonic properties of low-coordinated colloidal crystals, make the design and fabrication of colloidal lattices tremendously attractive. However, early studies of colloidal matter have focused on addressing altogether more fundamental questions, for example, those concerning phase diagrams and the kinetics of crystallisation.[1] A remarkable example is the experimental realisation of the phase behaviour of

the hard-sphere system with sterically stabilised colloidal polymethylmethacrylate particles by Pusey and van Megen, as shown in **Figure 1.5**.[76,77] The phase behaviour includes an entropy-driven fluid-to-crystal phase transition that was predicted by Alder and Wainwright,[78] and also by Wood and Jacobson,[79] in computational studies in the 1950s nearly two decades before the experimental realisation.

Figure 1.5: The phase behaviour of hard-sphere colloids.[77] Adapted with permission from the Royal Society.

The system of hard-sphere colloids, in particular, has been investigated extensively to probe the kinetics of crystallisation both in simulations and experiments.[1,80–83] In the context of a first-order fluid-to-crystal phase transition observed for this system, the classical nucleation theory is often invoked.[84] Since crystal nucleation is a rare event, sophisticated simulation techniques are usually employed.[80] The key questions concern the structure, size and shape of the crystal nuclei and the rate at which they form. While computer simulation studies have provided valuable insight into mechanistic understanding of crystal nucleation,[80] direct real space imaging has proved crucial for resolving some of these questions.[82]

In recent years, significant advances in the ability to synthesise colloidal particles with a variety of shapes and rich surface chemistry in a controlled way have brought about a paradigm shift in the field of colloidal self-assembly.[3–7] The focus is now on exploiting the library of complex colloidal particles to programme the self-assembly of novel functional materials. In this context, colloidal crystals have received great attention due to their potential applications in plasmonics, magnetics, photonics and metamaterials. The fabrication of geometrically well defined, non-close packed crystal structures is critical to many of these applications. However, attaining long-range order for low-coordinated structures has proven to be difficult.

Glotzer and co-workers were among the first to utilise the potential of "patchy" colloids to stabilise low-coordinated colloidal crystals such as a diamond crystal in computer simulations.[85] The model system studied by Zhang *et al.* consisted of spherical particles with a hard core, decorated with a tetrahedral arrangement of attractive surface patches, hereafter referred to as tetrahedral patchy particles. The pair-potential used involved a square-well modulated by an angular term, given by Kern and Frenkel.[53] Zhang *et al.* observed the self-assembly of a diamond crystal in Monte Carlo simulations upon cooling, as shown in **Figure 1.6a**.[85] Since then, a number of *in silico* studies have investigated tetrahedral patchy particles.[11,86–92] Romano *et al.* sought optimal conditions for spontaneous crystallisation of open crystal structures for tetrahedral patchy particles.[11] These authors examined the effects of varying patch width and interaction range on the equilibrium phase behaviour and kinetics of crystallisation in competition with glass formation. They observed spontaneous formation of open crystal structures for patch width values smaller than about 30°, nearly independent of the interaction range studied.[11] In this computational study, a detailed analysis was presented to distinguish between a cubic diamond lattice and a hexagonal diamond lattice, the two common open crystals formed by four-coordinated tetrahedral particles. The six-membered rings in the perfect cubic diamond structure are only in 'chair' conformation, while they include both 'chair' and 'boat' conformations in the perfect hexagonal diamond structure. In spite of the promise of tetrahedral patchy particles as building blocks for a colloidal cubic diamond lattice, their synthetic realisation with precise control over the patch position and patch width has eluded experimentalists. In a significant step forward, Sacanna and co-workers very recently devised a new strategy, which the authors referred to as colloidal fusion, for the synthesis of patchy particles.[93] The method

produced particles with liquid surface patches or a faceted liquid compartment in a tunable and scalable manner.[93] The authors envisaged manufacturing materials with unprecedented microstructural complexity by exploiting this method.[93]

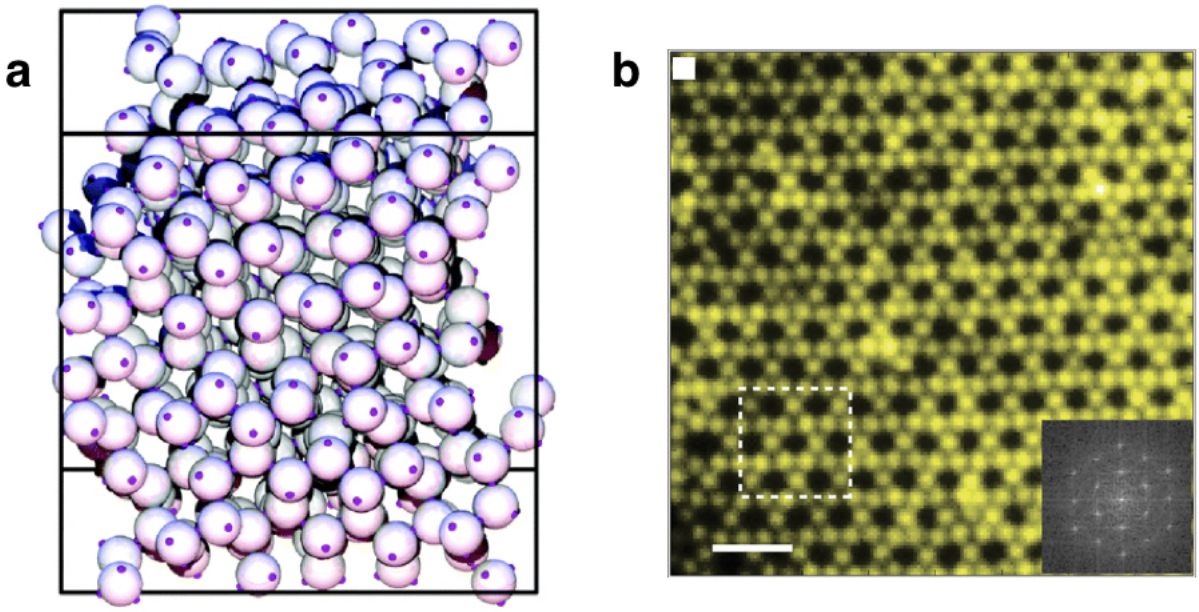

Figure 1.6: **a.** Monte Carlo simulation results, obtained using a slow cooling rate, exhibiting the diamond structure formed via 'patchy' colloids with tetrahedrally ordered attractive surface patches.[85] Copyright (2005) American Chemical Society. **b.** Fluorescence microscopy image of the kagome lattice and its fast Fourier transform image (bottom right). Scale bar is 4 μm. The colloidal lattice shown is formed of triblock Janus colloids which have two equal-sized hydrophobic patches at either pole separated by an charged middle band.[94] Reprinted with permission from Macmillan Publishers Ltd: Nature, copyright (2011).

While tetrahedral patchy colloidal particles have, until very recently, remained difficult to synthesise, triblock patchy colloidal particles, have been synthesised in large quantities via the glancing angle deposition (GLAD) technique.[5,94,95] Granick and co-workers used the GLAD method to deposit thin films of titanium and gold onto latex sphere of sulphate polystyrene on opposite poles, which were rendered hydrophobic by subsequent thiol surface functionalisation;[94] they referred to the particles with two hydrophobic patches at either pole separated by a charged middle band as "triblock Janus" particles. Chen *et al.* demonstrated the self-assembly of the triblock Janus particles into a colloidal kagome lattice in a quasi two-dimensional system, as shown in **Figure 1.6b**.[94] The assembly was switched on by adding salt to the colloidal suspension; the electrostatic repulsion between the charged middle bands was thus effectively screened, allowing the hydrophobic attractions to come to the fore and drive the assembly.[94]

The geometrical arrangement of neighbouring particles is limited by the patch size and the desire to avoid energetically unfavourable contacts between the charged middle bands. The GLAD synthesis method used here was able to offer strict control over the patch width, with a half-angle of 65° – critical for the geometrical arrangement observed for a kagome lattice. Chen *et al.* also followed the self-assembly of the kagome lattice utilising fluorescence imaging.[94] The pathway they observed was reminiscent of two-step nucleation in protein solutions, where a dense amorphous state is a precursor of the ordered state.[94]

The synthesis and self-assembly of triblock Janus particles stimulated a number of computational studies concerning them.[92,96] The computational study by Romano and Sciortino captured the self-assembly of the open Kagome lattice at low temperatures and pressures, and predicted a close-packed hexagonal lattice at high pressures.[96] Sciortino and co-workers provided further evidence of this in a consequent numerical study.[92] The authors here focused on designing patch shape and symmetry for triblock Janus particles so that they selectively self-assemble into a particular three-dimensional crystal structure, thus avoiding undesired polymorphs. In this study, triblock Janus particles patterned with staggered and eclipsed triangular patches were shown to self-assemble into a cubic tetrastack lattice and a clathrate-like crystal structure, respectively. Such a design helped the selection of local geometry, which cleaned up the self-assembly pathway into a select crystal structure.[92]

Chen *et al.* subsequently studied triblock patchy particles whose patches differed in their size.[97] The ionic strength of the medium was increased in two steps to sequentially trigger the activation of "bonds" formed by the hydrophobic attractions between the patches.[97] In the first stage of assembly, the bonds are formed by the larger patches, leading to small three-dimensional clusters, which the authors referred to as "metastructures". When the salt concentration in the medium was increased further, higher-order structures were then formed via attractive interactions between the smaller hydrophobic patches.[97] However, the clusters produced in the first stage showed distribution in size, which was not conducive for crystal formation in the next stage. A porous network structure was envisaged instead via staged self-assembly, leading to structural, and potentially functional hierarchy.[97]

In a notable contribution, Miszta *et al.* demonstrated two-level hierarchical self-assembly of monodisperse colloidal octapod-shaped nanocrystals into three-dimensional superstructures

via linear chains of interlocked octapods.[98] The shape was crucial in this case to encode the hierarchical self-assembly information. In a computer simulation study, Grunwald *et al.* showed the assembly of finite clusters of well-defined structure and composition from a mixture of spherical particles with short-range isotropic interactions by controlling only their sizes and a small number of binding affinities.[99] These finite clusters, referred to as "metaparticles", exhibited emergent patchiness. In order to study the next stage of assembly of these metaparticles exploiting their patchiness, the metaparticles were treated as rigid bodies and were shown to assemble into a variety of complex superstructures, including filamentous networks, ordered sheets, and highly porous crystals (**Figure 1.7a**.[99])

In recent work Crocker and co-workers demonstrated the potential for realising structural hierarchy via a variety of colloidal clusters with distinct symmetries formed using colloidal crystal templates and programmable DNA interactions.[100,101] They employed a templating approach with a closed-packed "host" lattice of DNA-functionalised microspheres containing "impurity" species at substitutional or interstitial defect sites. The colloidal crystal includes DNA bridges between the two species formed by enzymatic ligation. Upon melting the colloidal crystal, colloidal clusters consisting of a single impurity particle surrounded by host particles were produced. By adjusting the size ratio of the two types of spheres and the timing of the ligation, colloidal clusters having the symmetry of tetrahedra, octahedra, cuboctahedra, triangular orthobicupola, and icosahedra, were produced from single type of the host lattice as the template. These colloidal clusters exhibited multiple binding sites for DNA-mediated directional interactions, which could drive the next stage of self-assembly.[101] In fact, a more recent computational study by Zanjani *et al.* demonstrated a self-assembly scheme for pre-assembled cubic, tetrahedral, and octahedral clusters into superstructures in which the clusters are connected to each other indirectly via "bond spheres", shown in **Figure 1.7b**.[102]

The colloidal analogue of $MgCu_2$, one of the three AB_2 crystals known as Laves structures, has elicited attention in the context of programmed colloidal self-assembly because the crystal structure involves diamond and pyrochlore sublattices.[103–105] Dijkstra and co-workers employed pre-assembled colloidal clusters in their recent computational study to design an alternate route to the fabrication of colloidal crystals.[104] In this study, the authors considered a binary mixture of hard tetrahedral clusters and hard spheres and calculated the phase diagram. The phase

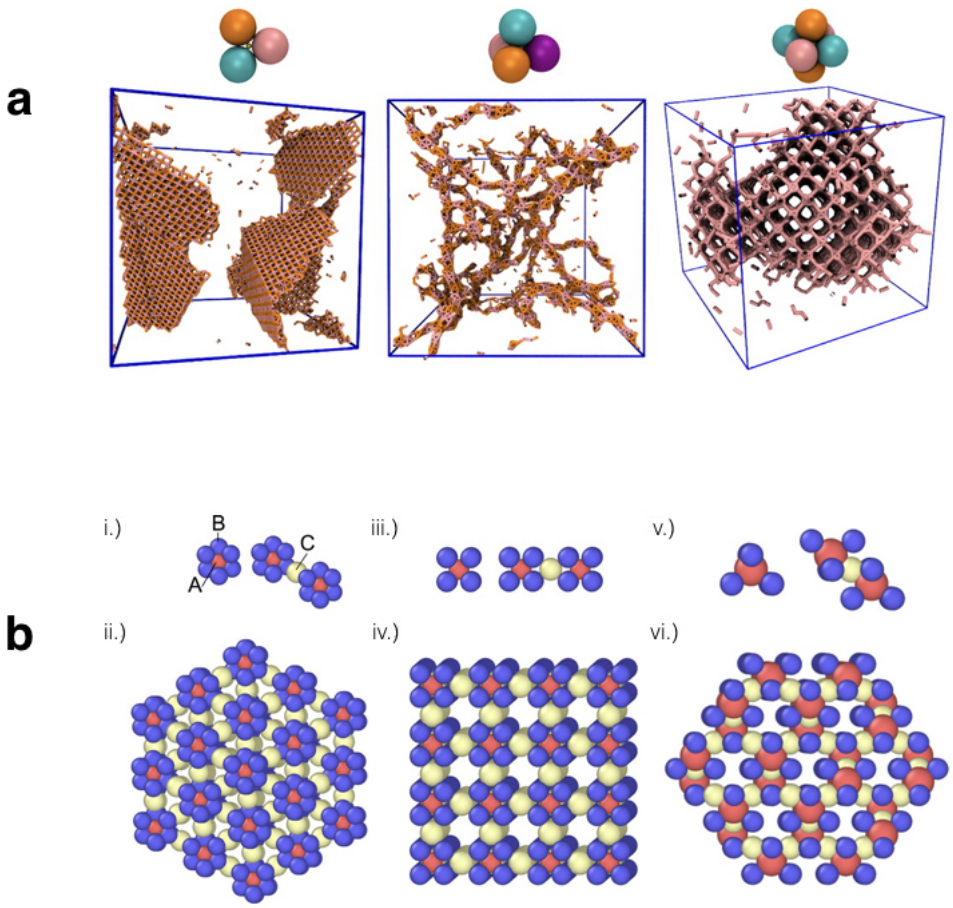

Figure 1.7: **a.** (top) The different metastructures formed in high yield during the first stage of self-assembly once the size ration and binding affinities between 'glue particles' and monomers has been appropriately tuned. (bottom) Each simulation box highlights an example of the kind of colloidal superstructure that can be produced in the second stage of self-assembly, ordered sheets, filamentous networks and colloidal crystals respectively.[99] Reprinted under a Creative Commons Attribution 4.0 International License. **b.** The colloidal molecules, formed of a centre sphere (red) and surrounding halo spheres (blue), and the expected, corresponding, ordered structures whose formation is mediated by spherical bond spheres (yellow). (i) octahedra, (ii) body-centred cubic lattice, (iii) cubes, (iv) simple cubic lattice, (v) tetrahedra, (vi) diamond cubic lattice.[102] Copyright (2016) American Chemical Society.

diagram shows that a thermodynamically stable colloidal analogue of the $MgCu_2$ Laves phase (**Figure 1.8b**), known to serve as a precursor to photonic band gap structures,[103] exists over a large region.[104] In the $MgCu_2$ Laves phase, the tetrahedral clusters occupy the sites of the pyrochlore lattice and the spheres occupy the cubic diamond sites. The computational study also revealed a relatively large coexistence region between the fluid and the $MgCu_2$ Laves phase, which should be experimentally accessible.[104] Pine and co-workers indeed experimentally realised the $MgCu_2$ Laves phase among a number of colloidal superstructures from pre-assembled colloidal tetrahedra and spheres (**Figure 1.8a**).[105] The experimental study, however, also ex-

ploited DNA-mediated interactions by coating the pre-assembled tetrahedra and spheres with complementary strands of DNA.[105] Ducrot *et al.* noted the versatility of their approach in the sense that almost any material could be used to make the colloidal particles, DNA-mediated interactions being the driver for the self-assembly. This feature would be crucial for selective removal of one or the other sublattice via etching, burning or dissolution.[105]

Wang *et al.* further demonstrated the potential of DNA-mediated colloidal crystal assembly in a recent study, which combined simulation and experiment.[106] In this study, the authors exploited a binary system of microspheres having slightly different sizes and complementary DNA strands grafted onto their surfaces for self-assembly into a "double diamond" crystal – a periodic structure with two interpenetrating diamond lattices, as shown in (**Figure 1.8c**).[106] The self-assembly was driven by short-ranged attractions due to DNA bridge formation. In a double diamond crystal structure, the second diamond lattice, formed by the smaller colloidal spheres, interpenetrates and acts as a 'scaffold' for the first diamond lattice formed by compositionally distinct colloidal spheres. Wang *et al.* suggested that by crosslinking such crystals and dissolving the smaller scaffold species, diamond crystals could be obtained. However, in Brownian Dynamics simulations designed to match the experiments, the nucleation or growth of such double diamond crystals was not observed, suggesting non-classical mechanisms for both processes.[106]

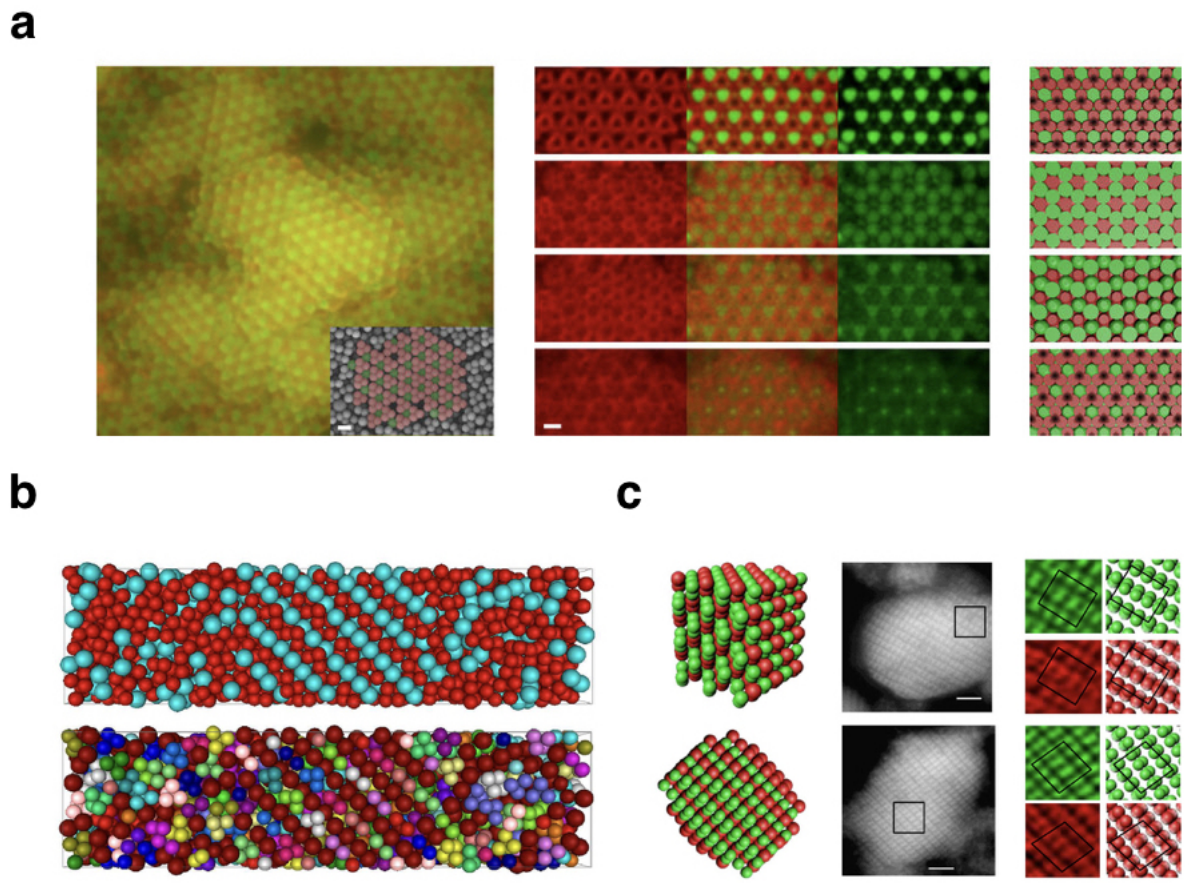

Figure 1.8: **a.** (left) Fluorescent microscope image of the $MgCu_2$ Laves phase formed by a binary mixture of larger colloidal spheres and rigid tetrahedral colloidal molecules. Inset is a electron microscope image of the $MgCu_2$ crystal, with false colours used to clearly distinguish the two colloidal species present. (centre) Confocal images of the $MgCu_2$ crystal parallel to the [111] plane. Successive layers of the crystal structure along the [111] plane are shown moving from top to bottom. Throughout, dye contained within the DNA coatings of the tetrahedral colloidal molecules and the bulk of the larger colloidal spheres, gives rise to the red and green colours observed respectively. The left column of the image shows the red channel with only tetrahedra visible, in the right column the green channel is shown, thus only the larger colloidal spheres are visible. (right) Rendering of the corresponding successive planes in the perfect $MgCu_2$.[105] Reprinted with permission from Macmillan Publishers Ltd: Nature, copyright (2017). **b.** Representative final configurations showing the coexistence of the fluid and $MgCu_2$ Laves phase seen in simulation. (top) Rigid tetrahedral colloidal molecules shown in red and larger colloidal spheres shown in blue. (bottom) Larger colloidal spheres shown in red, with colour coding to highlight the different tetramers.[104] Reprinted under a Creative Commons Attribution 4.0 International License. **c.** (left) Two differing schematic views of the double-diamond lattice. (middle) Confocal images taken from two different crystallites both in the [211] viewing direction. (right) Zoomed into the box regions shown in the corresponding confocal images, the two species of colloidal spheres present and their double-diamond structure are highlighted.[106] Reprinted with permission from Macmillan Publishers Ltd: Nature, copyright (2017).

1.4 Thesis Outline

It is apparent from the literature surveyed here that the hierarchical schemes for colloidal building blocks, while enormously promising as a bottom-up means for structure fabrication, are only at an early stage of exploration. In this context, the computational study undertaken in this thesis sought to encode structural hierarchy in anisotropic colloidal particles. The study considered certain target structures, both finite-size and periodic, for programmed self-assembly, designing hierarchical self-assembly schemes for colloidal particles. A particular emphasis was placed on furthering our understanding of how a multitude of colloidal interactions in the presence of more than one anisotropy attribute can be manipulated to ensure that the target structure is not only thermodynamically favourable, but also kinetically accessible.

Chapter 2 presents an overview of methodology, describing a variety of computational techniques employed in the body of work presented in this thesis. In **Chapter 3**, the remarkable hierarchical self-assembly of rationally designed charge-stabilised magnetic colloidal particles into hollow spheroidal structures is demonstrated for size-selected clusters. **Chapter 4** describes the design of a series of supracolloidal polyhedra and characterises the dominant pathways for self-assembly into these polyhedra revealing two distinct mechanisms. **Chapter 5** examines the kinetic accessibility of a series of hollow spheroidal structures with a two-level structural hierarchy self-assembled from charge-stabilised colloidal magnetic particles and derives an optimal design rule for a staged assembly pathway. Building on these findings, **Chapter 6** introduces and validates a generic design principle that exploits a hierarchy of interaction strengths to programme hierarchical self-assembly. The application of the the design principle realised with triblock patchy particles results in an extraordinary display of hierarchical self-assembly into a variety of colloidal crystals via distinct "colloidal molecules" of uniform size and shape. In particular, the open colloidal crystal of cubic diamond structure, much sought-after for their attractive photonic properties, are self-assembled via tetrahedral clusters. Finally, **Chapter 7** concludes with a summary and an outlook.

Chapter 2

Methodology

2.1 Computer simulations of colloidal matter

Computer simulations have become an indispensable tool for soft matter research.[107,108] In particular, the study of colloidal model systems by a variety of simulation techniques has provided invaluable insight into the structure, thermodynamics and kinetics of colloidal matter. Many such model systems have been subsequently realised in the laboratory, thus validating predictions made in computational studies, a classic example being the entropy-driven freezing of hard-sphere colloids.[76,78,79] This success is remarkable given that the wide discrepancy in the length- and time-scales associated with the mesoscopic colloidal particles and the solvent molecules necessitates a coarse-grained approach in order to efficiently simulate colloidal matter.[109]

Coarse-graining is a theoretical tool, derived from a statistical mechanical description of the system under consideration. In the context of simulating colloidal matter, the conventional coarse-graining approach involves a one-component description with an effective potential between the slow-moving colloidal particles, where the fast solvent degrees of freedom are projected out.[109] Here, when the phenomena occurring at the mesoscopic scale is of primary interest, the influence of the vast number of fast solvent degrees of freedom are captured by a statistical mechanical description rather than in microscopic detail. The effective potential between mesoscopic colloidal particles therefore involves parameters, often related to the solvent degrees of freedom. Coarse-graining is, however, not just a tool to simplify problems, for which the computational burdens are prohibitively expensive; it is also a useful tool for identifying

minimal conditions required for certain emergent properties of interest.

A basic question pertinent to a colloidal dispersion concerns its stability. The mesoscopic particles of a colloidal dispersion tend to undergo an irreversible aggregation due to ubiquitous van der Waals attractions, unless a stabilisation mechanism is in place. There are two common stabilisation mechanisms: charge stabilisation and steric stabilisation, either of which brings in a repulsive interaction. Here the charge stabilisation technique is discussed in some detail as throughout this thesis charge-stabilised colloidal particles are considered.

The surfaces of charge-stabilised colloidal particles dispersed in a polar solvent acquire a net charge, arising from the dissociation of ionisable groups at the colloid surface to a variable degree. Subsequently, counterions diffuse in the solvent maintain an average charge "cloud", of opposite sign to that of the surface charge, surrounding the colloidal particles. This results in an electric double layer, composed of counterions and including ions from the dissociation of any added electrolyte. The electric double layer screens the electrostatic repulsion between colloidal particles.

The seminal work by Derjaguin and Landau,[110] and independently by Verwey and Overbeek,[111] provides a theoretical framework to explain the charge stabilisation mechanism. The DLVO theory, named after them, is regarded as a cornerstone of colloid science. The DLVO theory describes the effective interaction between a pair of charged, spherical colloidal particles at a separation r as a combination of screened electrostatic repulsion and van der Waals attraction. The screened electrostatic repulsion is given by

$$V_{\mathrm{SER}} = \left(\frac{Z_0 e \exp(\kappa\sigma/2)}{1+\kappa\sigma/2} \right)^2 \frac{\exp(-\kappa r)}{\epsilon_r r} \tag{2.1}$$

which could be envisaged as emerging from a screened Coulomb interaction between a pair of particles, each carrying a charge

$$Ze = Z_0 e \frac{\exp(\kappa\sigma/2)}{1+\kappa\sigma/2}. \tag{2.2}$$

Here, $Z_0 e$ is the bare charge present on the surface of the colloidal particle and the factor multiplying $Z_0 e$ enhances the bare charge accounting for the finite size of the colloidal particle;

σ is the diameter of the spherical particles. The inverse Debye screening length is given by

$$\kappa = \left(\frac{4\pi}{\epsilon k_{\mathrm{B}} T} \sum_i \rho_i (z_i e)^2 \right)^{1/2} \tag{2.3}$$

summing over all ionic species, where the species i carries a charge $z_i e$ and is present with a number density ρ_i. The parameter κ enters this theoretical framework as the Poisson-Boltzmann equation, used in the treatment of electrostatic interactions, is linearised in the Debye-Hückel limit, which corresponds to the weak coupling regime. The Debye screening length $\lambda \equiv \kappa^{-1}$ provides an estimate for the thickness of the electric double layer. Equation 2.1 provides a reasonably accurate description in the case of relatively dilute dispersions, where the particles are well separated. Equation 2.1 has the form of the so-called Yukawa potential, which is given with a hard core as follows:

$$v(r) = \begin{cases} \infty, & r < \sigma \\ \epsilon_{\mathrm{Y}} \frac{\exp[-\kappa(r-\sigma)]}{r/\sigma}, & r \geq \sigma \end{cases} \tag{2.4}$$

where ϵ_{Y} is the contact potential given by

$$\epsilon_{\mathrm{Y}} = \frac{Z_0^2}{(1+\kappa\sigma/2)^2} \frac{\lambda_{\mathrm{B}}}{\sigma} k_{\mathrm{B}} T. \tag{2.5}$$

Here $\lambda_{\mathrm{B}} = e^2/(\epsilon_{\mathrm{r}} k_{\mathrm{B}} T)$ is the Bjerrum length of the solvent with the dielectric constant ϵ_{r}. The repulsive Yukawa potential is widely used in computational studies of charge-stabilised colloidal particles,[112–116] and the results have been found to largely agree with experimental observations.[117–119]

A rigid-body description is widely used to model colloidal particles, especially in the presence of one or more anisotropy attributes.[120] Chasles' theorem states that the most general displacement of a rigid body can be described as a translation plus a rotation.[121] This statement guides us to a minimal set of rigid-body co-ordinates. While the translational co-ordinates are typically represented by the centre-of-mass Cartesian co-ordinates, the rotation of a rigid body can be described by several representations. For a cylindrically symmetric rigid body a unit-vector description defining the orientation of the symmetry axis in the space-fixed frame is sufficient. However, for a rigid body with arbitrary symmetry, a more involved representation is

necessary, corresponding to its three orientational degrees of freedom. Euler angles, angle-axis variables and quaternions are three common representations for the orientational degrees of freedom for rigid bodies with an arbitrary symmetry. Careful consideration is necessary while making the choice for representation.

2.1.1 Rigid-body Rotation

The treatment of rigid-body rotation differs in the choice of representation for orientational degrees of freedom. Here we consider *active* rotations, in which rotations are performed counterclockwise in a fixed right-handed co-ordinate system. For practically all operational purposes a 3×3 rotational matrix $\mathbf{R}$ is generated corresponding to the chosen parameterisation. The rotation matrix $\mathbf{R}$, when acting on a vector $\mathbf{v}$, returns the transformed vector $\mathbf{v}'$ in the fixed basis corresponding to a rotation. The rotation matrix is an orthogonal real matrix with the determinant $\det \mathbf{R} = 1$ and describes a rotation about an axis by an angle. One of the eigenvalues for every 3×3 rotational matrix $\mathbf{R}$ is equal to 1, while the other two eigenvalues are complex conjugates of each other. The eigenvector corresponding to the real eigenvalue with unit magnitude defines the axis of rotation; the angle of rotation θ satisfies the relationship: $\mathrm{Tr}\, \mathbf{R} = 1 + 2\cos\theta$.

A primitive representation for rigid-body rotation consists of a set of three Euler angles, each of which corresponds to an angle of rotation about a fixed axis, either defined in the space-fixed frame or in the body-fixed frame. The set of three Euler angles are typically denoted as α, β, and γ or ϕ, θ, and ψ. The sequence of rotation matters and a complete description of orientation requires the corresponding axes to be specified as well, unless implied by the convention followed. The rotation matrix $\mathbf{R}$ corresponding to the sequence of these three rotations is the product of the individual rotation matrices, which do not commute.

Although the Euler angles provide an intuitive way of describing the orientation of a rigid body, the use of Euler angles is limited due to the phenomenon, called "gimble lock", which refers to the situation where one of the rotational degrees of freedom is lost. Numerical treatment of the equations of motion expressed in terms of this set of angles thus suffers from serious issues.

Euler's theorem, which states that the general displacement of a rigid body with one point

fixed is a rotation about some axis running through that point,[121] underlies an alternative representation for rigid-body rotation in terms of a single axis and angle. The angle-axis representation consists of a unit vector $\hat{\boldsymbol{p}}$ defining the axis of rotation and an angle θ describing the magnitude of rotation about this axis. A three-parameter representation can be obtained by considering the unnormalised rotation vector:

$$\mathbf{p} = [p_1, p_2, p_3] = \theta\hat{\boldsymbol{p}}. \tag{2.6}$$

Given a rotation vector $\mathbf{p}$, the corresponding 3×3 rotation matrix $\mathbf{R}$ can be obtained using Rodrigues' rotation formula:

$$\mathbf{R} = \mathbf{I} + (1 - \cos\theta)\,\tilde{\boldsymbol{p}}\tilde{\boldsymbol{p}} + \sin\theta\tilde{\boldsymbol{p}} \tag{2.7}$$

where $\mathbf{I}$ is a 3×3 identity matrix and $\tilde{\boldsymbol{p}}$ is the skew-symmetric matrix obtained from $\mathbf{p}$:

$$\tilde{\boldsymbol{p}} = \frac{1}{\theta}\begin{pmatrix} 0 & -p_3 & p_2 \\ p_3 & 0 & -p_1 \\ -p_2 & p_1 & 0 \end{pmatrix} \tag{2.8}$$

Equation 2.7 is the key to the matrix formulation, which underpinned a robust and efficient geometry optimisation scheme implemented in the software `GlOSP` developed in-house.[122] This scheme provides a flexible, user-friendly interface to treat any rigid-body system governed by site–site isotropic or anisotropic potentials with analytic derivatives.[123]

Using a notation to denote derivatives of a matrix $\mathbf{A}$, $\partial\mathbf{A}/\partial p_k$, by $\mathbf{A}_k$ $(k = 1, 2, 3)$, we have[123]

$$\begin{aligned} \mathbf{R}_k &= \frac{p_k \sin\theta}{\theta}\widetilde{\mathbf{p}}^2 + (1 - \cos\theta)(\widetilde{\mathbf{p}}_k\widetilde{\mathbf{p}} + \widetilde{\mathbf{p}}\widetilde{\mathbf{p}}_k) \\ &+ \frac{p_k \cos\theta}{\theta}\widetilde{\mathbf{p}} + \sin\theta\widetilde{\mathbf{p}}_k. \end{aligned} \tag{2.9}$$

In the limit as $\theta \to 0$, the formulation in Equation 2.7 reduces to a 3×3 identity matrix. A Taylor expansion up to the second order terms can then be considered to obtain analytic derivatives of the rotation matrix with respect to the elements of $\mathbf{p}$.

Let us consider a site-site isotropic potential in order to illustrate how this formulation works out the analytic derivatives. Denoting the co-ordinates of two rigid bodies using the superscripts I and J, and the sites within each rigid body by the subscripts i and j, the total potential energy is given by

$$U = \sum_{I} \sum_{J<I} \sum_{i \in I} \sum_{j \in J} f_{ij}(r_{ij}), \tag{2.10}$$

where $r_{ij} = |\mathbf{r}_{ij}| = |\mathbf{r}_i - \mathbf{r}_j|$ and $f_{ij} \equiv U_{ij}^{IJ}$ is the pair potential between sites i and j. If ζ represents one of the six co-ordinates of rigid body I, then the first derivative of the potential energy is

$$\frac{\partial U}{\partial \zeta} = \sum_{J \neq I} \sum_{i \in I} \sum_{j \in J} f'_{ij}(r_{ij}) \frac{\partial r_{ij}}{\partial \zeta}, \tag{2.11}$$

where $f'_{ij} = df_{ij}(r_{ij})/dr_{ij}$. In this prescription

$$\frac{\partial r_{ij}}{\partial \mathbf{r}^I} = \hat{\mathbf{r}}_{ij}, \tag{2.12}$$

and

$$\frac{\partial r_{ij}}{\partial p_k^I} = \hat{\mathbf{r}}_{ij} \cdot \frac{\partial \mathbf{r}_{ij}}{\partial p_k^I} = \hat{\mathbf{r}}_{ij} \cdot (\mathbf{R}_k^I \mathbf{r}_i^0), \tag{2.13}$$

where we have used

$$\mathbf{r}_{ij} = \mathbf{r}^I + \mathbf{R}^I \mathbf{r}_i^0 - \mathbf{r}^J - \mathbf{R}^J \mathbf{r}_j^0. \tag{2.14}$$

Alternatively, quaternions provide a 4-parameter description of rigid-body rotation.[124] The quaternion representation has emerged as a popular choice in the context of molecular modelling for its singularity-free description of rigid-body rotation and the elegance of quaternion algebra for the manipulation of rotations.[125] A quaternion $\mathbf{Q}$ is an ordered set of four real quantities, which can also be viewed as a combination of a scalar and a three-dimensional vector:

$$\mathbf{Q} = [q_0, q_1, q_2, q_3] = [q_0, \mathbf{q}]\,. \tag{2.15}$$

A unit quaternion satisfies the unit-norm constraint:

$$q_0^2 + q_1^2 + q_2^2 + q_3^2 = 1. \tag{2.16}$$

A quaternion representation equivalent to the angle-axis parameterisation is $Q = (q_0, q_1, q_2, q_3) \equiv (q_0, \mathbf{q}) = (\cos(\theta/2), \hat{\mathbf{p}}\sin(\theta/2))$, and the reverse transformation is straightforward. The elements of the 3×3 rotation matrix $\mathbf{R}$ corresponding to the unit quaternion Q are given by

$$\mathbf{R} = \begin{bmatrix} 1 - 2q_2^2 - 2q_3^2 & 2q_1 q_2 - q_0 q_3 & 2q_1 q_3 + 2q_0 q_2 \\ 2q_1 q_2 + 2q_0 q_3 & 1 - 2q_1^2 - 2q_3^2 & 2q_2 q_3 - 2q_0 q_1 \\ 2q_1 q_3 - 2q_0 q_2 & 2q_2 q_3 + 2q_0 q_1 & 1 - 2q_1^2 - 2q_2^2 \end{bmatrix}. \tag{2.17}$$

The rotation matrix can thus be derived from a unit quaternion computationally in a more efficient way compared to Euler angles due to the absence of trigonometric functions and the requirement of fewer multiplications to be evaluated. Although quaternions are widely used to represent rigid-body rotation in particle-based simulation, the unit-norm constraint introduces added complexity in the context of certain simulations techniques, such as geometry optimisation.[123]

2.2 The Potential Energy Surface

The concept of the potential energy surface (PES) underpins a useful computational framework to understand the structure, thermodynamics and kinetics of a system from the perspective of the energy landscape.[126] In the one-component treatment with an effective potential, a PES for a system of colloidal particles can be defined describing how the potential energy (V) changes as a function of the positional and orientational co-ordinates. In a compact notation, these co-ordinates are denoted here by $\mathbf{x}$. While the entropy plays a crucial role in governing colloidal self-assembly, evaluating the potential energy landscape can also provide important information with regard to colloidal self-assembly.

The stationary points on the PES, where the gradient vanishes, i.e.

$$\nabla V(\mathbf{x}) = 0 \quad \text{where} \nabla \equiv \Big(\frac{\partial}{\partial x_1}, ..., \frac{\partial}{\partial x_N}\Big)^T, \tag{2.18}$$

are of particular interest. The importance of stationary points on the PES can be understood

by considering the relationship between the potential energy V and the force $\mathbf{F}$, where

$$\mathbf{F}(\mathbf{x}) = -\nabla V(\mathbf{x}). \tag{2.19}$$

The stationary points are therefore also the points at which the total force acting on the system vanishes leaving the system in mechanical equilibrium. However, mechanical equilibrium does not guarantee mechanical stability. The mechanical stability of a stationary point can be assessed by considering its local environment or local surface curvature. If the local environment is such that a small perturbation in any direction leads to a restorative force, acting to draw the system back to its initial state, the stationary point is deemed mechanically stable.

The Hessian, a square matrix whose elements are the second-order partial derivatives of V with respect to the coordinates, i.e.

$$H_{ij}(\mathbf{x}) = \frac{\partial^2 V(\mathbf{x})}{\partial x_i \partial x_j}, \tag{2.20}$$

carries the information of the surface curvature. The stationary points are classified into minima and saddle points depending of the number of negative eigenvalues. If $\mathbf{b}_\alpha$ is an eigenvector corresponding to the eigenvalue ϵ_α^2 of the Hessian matrix evaluated at a stationary point $\mathbf{x}_0$, then

$$\mathbf{H}(\mathbf{x}_0)\mathbf{b}_\alpha = \epsilon_\alpha^2 \mathbf{b}_\alpha. \tag{2.21}$$

Minima are stationary points with no negative Hessian eigenvalues. A stationary point with n negative Hessian eigenvalues is called a n-th order saddle point. A transition state has a single negative Hessian eigenvalue, and is thus a first-order saddle point.

One can describe the PES in the proximity of a stationary point $\mathbf{x}_0$ by considering a Taylor expansion of $V(\mathbf{x})$ around it:

$$V(\mathbf{x}) = V(\mathbf{x}_0) + \nabla V(\mathbf{x}_0)^T(\mathbf{x} - \mathbf{x}_0) + \frac{1}{2}(\mathbf{x} - \mathbf{x}_0)^T \mathbf{H}(\mathbf{x}_0)(\mathbf{x} - \mathbf{x}_0) + ... \tag{2.22}$$

In the quadratic approximation to the PES around the stationary point, the Taylor series is truncated beyond the second-order term. Since the gradient vanishes at a stationary point, one

can then write

$$V(\mathbf{x}) = V(\mathbf{x}_0) + \frac{1}{2}(\mathbf{x} - \mathbf{x}_0)^T \mathbf{H}(\mathbf{x}_0)(\mathbf{x} - \mathbf{x}_0). \tag{2.23}$$

Hence

$$\mathbf{F}(\mathbf{x}) = -\mathbf{H}(\mathbf{x}_0)(\mathbf{x} - \mathbf{x}_0). \tag{2.24}$$

The displacement $\mathbf{x} - \mathbf{x}_0$ can be expressed as a linear combination of the projections on the basis spanned by the eigenvectors of the Hessian matrix $\mathbf{H}(\mathbf{x}_0)$:

$$\mathbf{x} - \mathbf{x}_0 = \sum_\alpha b_\alpha \mathbf{b}_\alpha, \tag{2.25}$$

which when substituted in Equation (2.24) yields

$$\mathbf{F}(\mathbf{x}) = -\mathbf{H}(\mathbf{x}_0) \sum_\alpha b_\alpha \mathbf{b}_\alpha = -\sum_\alpha \epsilon_\alpha^2 b_\alpha \mathbf{b}_\alpha. \tag{2.26}$$

The above equation describes the force acting on a system in the neighbourhood of a stationary point in terms of the eigenvalues and eigenvectors of the Hessian $\mathbf{H}(\mathbf{x})$. If $\epsilon_\alpha^2 \geq 0$ for all α, then the total force acts as a restoring force pointing towards the stationary point. A stationary point with no negative Hessian eigenvalues is therefore mechanically stable and referred to as a minimum on the PES. The lowest energy minimum on the PES is known as the global minimum. The global optimisation methods are focused on finding the global minimum.

To obtain maximum information regarding the system of interest it would be ideal to locate all local minima on the PES. However, as the system size increases so does the number of minima, in an exponential fashion.[127] In terms of computational complexity, identifying the global minimum on a PES is non-trivial and belongs to a class of problems described as "NP-hard" for which there is no known solution to calculate the global minimum in a time frame that scales as a power of the system size.[128] However, this presents a worst case scenario, in reality the ease at which the global minimum is found largely depends on the size and nature of the search space concerned.[126] Several sophisticated search strategies have been developed to efficiently search for and identify the global minimum on the PES.[129–131] Throughout this

thesis one such strategy, namely the basin-hopping global optimisation method,[24,132] is used to identify the global minima in the context of structure prediction for colloidal clusters.

2.2.1 Basin-hopping Global Optimisation

The basin-hopping global optimisation method relies upon a hypersurface deformation, which undertakes the following transformation:

$$\tilde{V}(\mathbf{x}) = \min\{V(\mathbf{x})\}, \tag{2.27}$$

which implies that every point on the original PES $\mathbf{x}$ is mapped to its nearest local minimum whose catchment basin includes it. This transformation results in a reduced PES, $\tilde{V}(\mathbf{x})$, spanned only by the minima of the original PES. The reduces PES is then explored by a search strategy to find the lowest-lying minimum. A simple yet effective approach is to use Monte Carlo-like walk to "hop" between basins.

The body of work presented in this thesis used the basin-hopping global optimisation method as implemented in the software `GlOSP` – a program for Global Optimisation for Structure Prediction, developed in-house.[122] The implementation follows the steps below:

1. Perform a local minimisation from an arbitrary starting configuration.

2. Propose a random move or a perturbation $\Delta\mathbf{x}$ in both the positional and orientational co-ordinates, away from the current minimum $\mathbf{x}_a$ with potential energy V_a.

3. Perform a local minimisation from the perturbed configuration, resulting in the minimum $\mathbf{x}_b$ with potential energy V_b.

4. Make a decision to accept or the reject the proposed step. If $V_b < V_a$, the move to the new minimum is accepted. Otherwise the new minimum is accepted only if $\xi < \exp[-\Delta V/(k_\mathrm{B}T)]$, where ξ is a random number taken from a uniform distribution between 0 and 1. Here $\Delta V = V_b - V_a$ and T is a fictitious temperature used to allow for uphill steps with some probability. Upon acceptance of the move, the new minimum becomes the current minimum. If the proposed step is rejected, the current minimum, the one with $V = V_a$, does not change.

5. Return to step 2 and repeat steps 2-4.

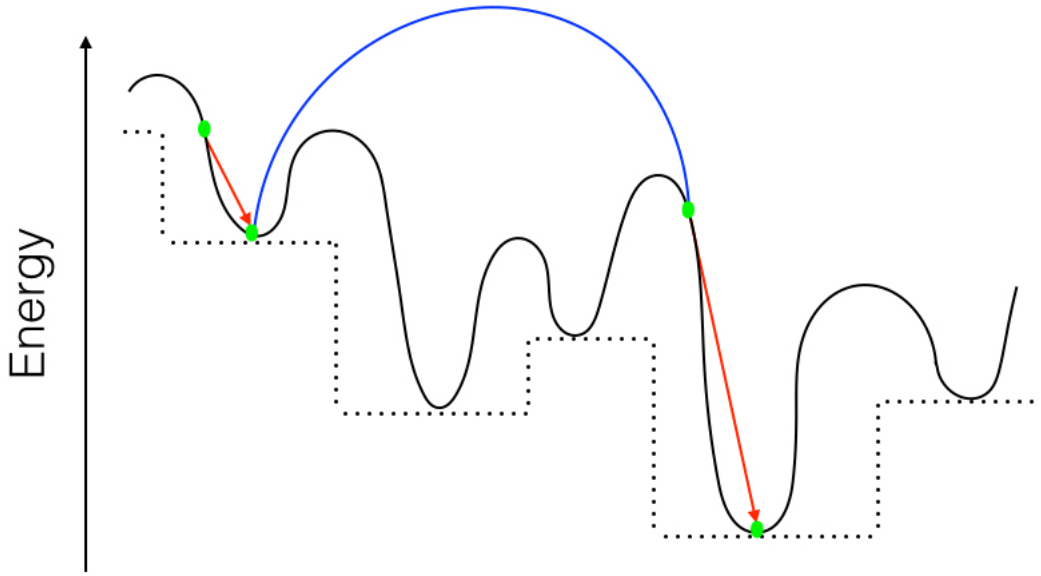

Figure 2.1: A schematic diagram of the basin-hopping procedure on a one-dimensional potential energy surface (solid line). The transformed potential energy surface (dotted line), local minimisations (red arrows) and random Monte Carlo step (blue line).

A basin-hopping step consists of a random move followed by local minimisation. A basin-hopping run is typically terminated after carrying out a certain preset number of basin-hopping steps. As the objective here is to frequently step ("hop") between basins, the step sizes are larger than those typically used for Monte Carlo sampling of thermodynamic properties. In a given basin-hopping run, the step sizes are systematically adjusted to achieve a target acceptance ratio corresponding to a fixed value of the fictitious temperature.

The key to an efficient implementation of the basin-hopping method is an efficient local minimiser as each basin-hopping step involves requires a local minimisation. There exists a number of different approaches to local minimisation. The implementation in `GlOSP` employs the limited-memory Broyden-Fletcher-Goldfarb-Shanno (L-BFGS) method.[133–137] The L-BFGS method is a quasi-Newtonian method, which is underpinned by the quadratic approximation to the PES:

$$V(\mathbf{x}+\mathbf{h}) = V(\mathbf{x}) + \mathbf{g}^T\mathbf{h} + \frac{1}{2}\mathbf{h}^T\mathbf{H}\mathbf{h}, \tag{2.28}$$

where $\mathbf{x}$ is an arbitrary point on the PES, $\mathbf{h}$ is a displacement and $\mathbf{g} = \nabla V(\mathbf{x})$ is the gradient. Applying $dV(\mathbf{x}+\mathbf{h})/d\mathbf{h} = \mathbf{0}$ in order to find the greatest rate of change in the potential energy

V with the displacement:

$$\mathbf{0} = \mathbf{g} + \mathbf{H}\mathbf{h}. \tag{2.29}$$

The above equation can then be re-arranged to give the displacement to obtain the so-called *Newton step*:

$$\mathbf{h} = -\mathbf{H}^{-1}\mathbf{g}. \tag{2.30}$$

In the L-BFGS method, a relatively cheap approximation to the inverse Hessian matrix is made in each iteration.

2.3 Monte Carlo Sampling

Basin-hopping global optimisation method is a useful tool for identifying the global minimum on the PES along with low-energy minima, which correspond to candidate structures observed in experiments. However, this method does not involve sampling at thermal equilibrium. Monte Carlo (MC) methods, and in particular the Metropolis Monte Carlo sampling, are widely used to study soft matter systems at thermal equilibrium.[138] The MC methods, in their most simple form, are based upon the generation of a large number of configurations $\mathbf{x}^N$ for the system under consideration and their subsequent statistical evaluation. The Metropolis Monte Carlo algorithm is used to optimise this statistical evaluation.[138]

The ensemble average of a thermodynamic property A for a system of N particles at thermal equilibrium can be evaluated as the ratio of two integrals:

$$\langle A \rangle = \frac{\int d(\mathbf{x}^N) \exp[-\beta V(\mathbf{x}^N)] A(\mathbf{x}^N)}{\int d(\mathbf{x}^N) \exp[-\beta\, V(\mathbf{x}^N)]}, \tag{2.31}$$

where $\beta = 1/(k_B T)$, $A(\mathbf{x}^N)$ is the value of the property A for configuration $\mathbf{x}^N$ and $V(\mathbf{x}^N)$ is the potential energy of the configuration $\mathbf{x}^N$. In all but the very simplest of cases, the analytical evaluation of the integrals is not possible. It is also impractical to use common numerical methods to evaluate the integrals for a system size that we are typically interested in. The Monte Carlo methods can instead be used to effectively evaluate such a ratio.

A simplest form of the Monte Carlo methods proceeds as follows:

- A large number (τ_{max}) of uniformly random configurations are generated.
- For each configuration, the potential energy $V(\tau)$ and the value of property $A(\tau)$ are calculated.
- Each configuration is then given a weighting according to the factor $\exp[-\beta V(\tau)]$.
- The average value for the property A is then computed using the following expression

$$\langle A \rangle \approx \frac{1}{\tau_{\max}} \sum_{\tau=1}^{\tau=\tau_{\max}} \frac{\exp[-\beta V(\tau)] A(\tau)}{\exp[-\beta V(\tau)]} \tag{2.32}$$

The approximation is fairly accurate for large values of $\tau_{\max}$. Despite its simplicity, this straightforward implementation of a Monte Carlo method involving random sampling is inefficient and therefore not fit for practical use. This inefficiency arises from the sampling of vast swathes of configuration space that have a negligible contribution to the integral. Alternately, the Metropolis Monte Carlo method provides an efficient method for sampling configuration space and henceforth evaluating A.

In the Metropolis method, instead of generating random configurations to which a weighting of $\exp(-\beta V)$ is applied, configurations are chosen with a probability $\exp(-\beta V)$, all of which are weighted evenly.[139] This restricts the algorithm to choosing and sampling only those configurations with a non-negligible contribution to the integral.

From an initial configuration, the Metropolis Monte Carlo method, as implemented in the software `PaSSion` – a package for soft matter simulation – developed and maintained in-house,[140] for particles treated as rigid bodies proceeds in the following way to move a single particle:

- From the current configuration $\mathbf{x}_a$ with potential energy V_a, a particle i is selected at random and then random translational and orientational moves for the particle are simultaneously proposed as follows:
  - The proposed updates for the Cartesian coordinates of the centre-of-mass of the

particle i proceeds as follows:

$$x_i = x_i + \alpha\xi_1$$
$$y_i = y_i + \alpha\xi_2$$
$$z_i = z_i + \alpha\xi_3,$$

where α is the maximum translational stepsize and ξ is a random number taken from a uniform distribution between 1 and -1.

– The quaternion $\mathbf{Q}_i$, which represents the orientation of particle i, is updated by generating a suitable quaternion increment $\mathbf{Q}_r = [q_{r0}, q_{r1}, q_{r2}, q_{r3}]$ at random. A new orientation $\mathbf{Q}_i'$ is thus generated in the following three steps:[141]

1. Three random numbers q_{r1}, q_{r2} and q_{r3} are generated, according to a Gaussian distribution, with zero mean and the width which is controlled by the maximum rotational stepsize λ, adhering to the constraint:

$$S = q_{r1}^2 + q_{r2}^2 + q_{r3}^2 < 1 \tag{2.33}$$

2. The quaternion $\mathbf{Q}_r = [q_{r0}, q_{r1}, q_{r2}, q_{r3}]$ is then formed with

$$q_{r0} = \sqrt{1 - S} \tag{2.34}$$

3. The new quarternion can then be obtained by multiplying the current quaternion $\mathbf{Q}_i$ with the quaternion increment generated following the quaternion algebra.

$$\mathbf{Q}_i' = \mathbf{Q}_r \mathbf{Q}_i \tag{2.35}$$

- A new configuration $\mathbf{x}_b$, corresponding to the application of such a translational and rotational move is thus generated, and the potential energy V_b evaluated. trial moves.

- The difference in potential energy ΔV is then calculated between configurations $\mathbf{x}_a$ and

$\mathbf{x}_b$.

$$\Delta V = V_b - V_a \tag{2.36}$$

- The move from $\mathbf{x}_a \rightarrow \mathbf{x}_b$ is accepted with the following probability

$$\text{Prob}(a \rightarrow b) = \begin{cases} 1 & \text{if } \Delta V < 0 \\ \exp(-\beta \Delta V) & \text{if } \Delta V > 0 \end{cases}, \tag{2.37}$$

  In the case where $\Delta V > 0$, the step is accepted if ξ, a random number taken from a uniform distribution between 0 and 1, is less than $\exp(-\beta \Delta V)$ and rejected otherwise.

This process is repeated for a preset number of MC cycles. For a system with N particles, each MC cycle consists of N attempts for single-particle translational and orientational moves each as described above. The maximum step sizes for both translational and orientational moves were adapted to achieve a target acceptance ratio of 0.45 in a given Monte Carlo simulation. In this thesis work Metropolis Monte Carlo simulations were undertaken in the canonical ensemble with fixed N, V and T. When MC simulations were used to study colloidal clusters, a spherical constraining volume was employed to avoid evaporation.

The memoryless nature of the movement from configuration $a \rightarrow b$ gives rise to the formation of a Markov chain, characterised by $\text{Prob}(a \rightarrow b)$ only being dependent on the current state a and not any of those which preceded it. An important feature of the random Markov chain during the Monte Carlo simulation is that it obeys the detailed balance. This ensures that equilibrium once reached is not disturbed by random moves.

2.4 Virtual-Move Monte Carlo Algorithm

This section describes the implementation of the virtual-move Monte Carlo (VMMC) algorithm, introduced originally by Whitelam and Geissler[142] and subsequently developed further by a number of authors.[143–145] The *symmetrised* version of the algorithm was implemented in the software `PaSSion` following the prescription of Růžička and Allen,[144] who provided an alternative perspective to this rather involved algorithm. The VMMC algorithm is a notable

contribution to the existing library of cluster algorithms,[146–151] which prescribe collective moves for particles in a Monte Carlo simulation as opposed to the standard practice of single-particle moves.[138] The single-particle moves are likely to result in "kinetic traps", especially in strongly interacting systems in the presence of short-ranged and/or anisotropic interactions. In the context of studying hierarchical self-assembly, in particular if it involves staged assembly, it is easy to recognise the importance of concerted movements of particles.

The concerted movements of particles are crucial for both intra-cluster relaxation and whole-cluster diffusion, which thus get suppressed in standard MC methods with single-particle moves. The previously existing cluster algorithms initially enjoyed a degree of success in surmounting this limitation of the standard MC methods. Early cluster-move algorithms typically employed cluster moves, where a moving cluster was selected through the recursive linking of neighbouring particles based upon their pair-wise potential energies in the current configuration, ignoring any possible changes to be induced by the proposed move. However, it soon became clear that, by proposing cluster moves in such a manner, these cluster algorithms tended to under represent internal relaxation and motion within a cluster. Therefore, neighbouring particles repeatedly moved collectively as part of a cluster, but rarely moved relative to one another.[144] This meant that any cluster-move algorithm operating in this way continued to encounter severe non-physical kinetic traps and prevented accurate sampling from an equilibrium distribution.

The VMMC method markedly improves upon the existing cluster algorithms by utilising the calculation of pair-wise potential energy gradients to avoid kinetic traps. Made possible by the execution of a 'virtual' move, the pair-wise potential energy gradients corresponding to the direction of a given move are determined during the recursive linking process. By assessing the pair-wise potential energy both before and after the 'virtual' move, neighbouring particles that, despite being strongly interacting, seek to benefit energetically from not being selected to the cluster can be identified and thus internal cluster relaxation is facilitated. Such cluster moves not only help to remove kinetic traps, but also allow particles to move according to an approximation of real dynamics without the explicit calculation of forces and torques. With careful consideration of the parameters governing the VMMC algorithm, this method can thus provide an insight into physical dynamics or deliver an enhanced sampling of the equilibrium distribution.

In the context of the objectives of the study undertaken in the present thesis, the implementation of a cluster-move MC algorithm was of paramount importance. Given its promise as a state-of-the-art cluster-move algorithm, the VMMC algorithm was chosen. In what follows, an outline of the VMMC algorithm, as implemented in `PaSSion` following the prescription of Růžička and Allen,[144] is presented along with the benchmarks performed.

2.4.1 Recursive Cluster Selection

The starting point, as in all MC procedures, is the selection of a random particle from the system, denoted by S, of N interacting particles and the generation of a random move map M. This randomly selected particle is then considered as the root of the cluster C to be proposed for a move. In general, cluster algorithms then go on to produce a randomly ordered cluster, forming what is referred to as a 'random tree' in graph theory, during the recursive selection process. This process, however, is not always the best given the aim of the simulation[144] and the possible introduction of a maximum cluster size N_C. Instead one may wish to produce a cluster that is more isotropic in nature, allowing the cluster to imitate a physical fluctuation more accurately. Selecting clusters in this manner may potentially result in a more efficient simulation and a closer relation to Brownian/Stokesian dynamics upon the generation of diffusion coefficients. The so-called isotropically ordered[144] and the spirally ordered[152] selection processes offer two routes to producing isotropic clusters through recursive cluster selection. **Figure 2.2** shows illustrative examples. The spirally ordered selection process was chosen in the present implementation.

The spirally ordered selection process begins by identifying all pairs of interacting particles (i, j), where i is denotes the randomly selected root particle. An interacting particle pair is defined as two particles (i, j) whose inter-particle distance, either before or after the application of a virtual move, is less than a cut-off distance R_c. The cut-off distance R_c depends on the interaction potential, and the nature of the virtual move is given by the randomly generated move map M. If (i, j) is deemed to be an interacting particle pair, it is added to a queue of interacting particles to be further tested before inclusion in the moving cluster C. Following the initial identification of all interacting particle pairs (i, j), a pair of particles is then randomly selected from the queue listed. The selected particle pair is then subjected to a two-step linking

procedure, described below. The first step induces a random test, which, if failed, results in the interacting particle pair (i, j) in question being labeled as an *outright failed* link. Upon passing the first test, the pair faces a second random test. The interacting particle pair (i, j) is labeled as a *frustrated* link if it fails the second test. Otherwise, particle j joins the root particle i as a member of the moving cluster C. The two-step link process is then repeated, selecting the next interacting particle pair (i, j) randomly from the aforementioned queue, until no more interacting particle pairs remain.

Given the addition of new particles to the cluster C, this entire process is then repeated iteratively for all such newly added particles. Every new iteration begins by again identifying all interacting particle pairs (i, j), where i now becomes one of the particles subsequently added to C and j is any other particle not already a member of C. The cluster C is then finally accepted for a move provided that during the recursive selection process, the moving cluster generation only produces particle links that either led to a particle being accepted to the cluster C or generates an *outright failed* link. In other words, if any *frustrated* links are formed during the selection process, the moving cluster is rejected.

Two-step Link Formation

In the following, the two-step linking procedure by which the link between an interacting pair (i, j) is determined to be *outright failed*, *frustrated*, or such that j is to become a part of the moving cluster C, is described in some detail. Performing the two-step linking procedure is crucial as it ensures internal cluster relaxation through the inclusion of a virtual move, while also guaranteeing that the recursive process leading to the generation of the moving cluster C in the VMMC algorithm adheres to the microscopic reversibility condition.

The overall probability of overcoming the two-step link process is given by the joint probability:

$$p_{ij}^{(\mu)} = \text{Prob}\left\{X_1 < p_{i'j}^{(\mu)};\ \ X_2 < \min\left(1, p_{ij'}^{(\mu)}/p_{i'j}^{(\mu)}\right)\right\}, \tag{2.38}$$

where (X_1, X_2) are independent random numbers taken from a uniform distribution $U(0, 1)$. The joint probability therefore can be simply broken down into two separate random tests. The

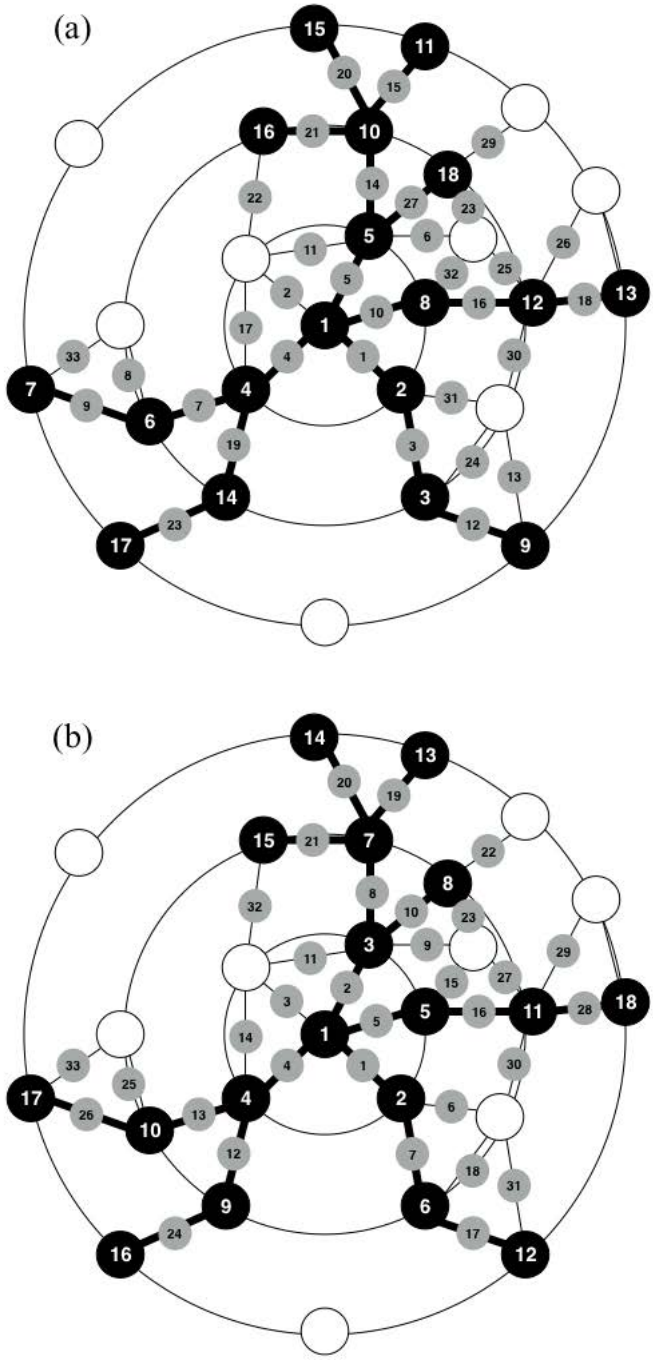

Figure 2.2: Two-dimensional representation of the randomly ordered selection process (a) and the spirally ordered selection process (b). Adapted from Růžička and Allen,[144] the diagram shows the order in which particles are accepted to the cluster alongside the order in which links between interacting pairs are proposed. Black discs are the particles which are members of the moving cluster C; white discs are particles outside the moving cluster; thick black lines highlight links formed; thin black lines show links tested but rejected; grey discs show the order in which links are proposed.

first test is whether

$$X_1 < p_{i'j}^{(\mu)} \tag{2.39}$$

and the second test is whether

$$X_2 < \min\left(1, p_{ij'}^{(\mu)}/p_{i'j}^{(\mu)}\right). \tag{2.40}$$

It is clear that the first test is independent of the second test. If the first test is failed, the fraction $p_{ij'}^{(\mu)}/p_{i'j}^{(\mu)}$ need not be evaluated, the interacting pair (i,j) is simply labeled as *outright failed*.

The first random test, as shown in the joint probability, requires the evaluation of the probability $p_{i'j}^{(\mu)}$:

$$p_{i'j}^{(\mu)} = \max\left\{0, 1 - \exp\left(-\beta\Delta\epsilon_{i'j}^{(\mu)}\right)\right\}. \tag{2.41}$$

The energy identity $\Delta\epsilon_{i'j}^{(\mu)}$ denotes the following energy difference

$$\Delta\epsilon_{i'j}^{(\mu)} = \epsilon_{i'j}^{(\mu)} - \epsilon_{ij}^{(\mu)}, \tag{2.42}$$

where $\epsilon_{ij}^{(\mu)}$ is given by the pair-wise interaction energy between particles (i,j) in the current configuration μ and $\epsilon_{i'j}^{(\mu)}$ is the pair-wise interaction energy between particles (i,j) after applying the 'virtual move', provided by the move map M, to particle i.

Once the first test is passed, the second random test then determines whether the interacting pair (i,j) is to form a *frustrated* link or particle j is to become part of the moving cluster C. The second test demands the evaluation of the fraction $p_{ij'}^{(\mu)}/p_{i'j}^{(\mu)}$. In order to calculate this quantity, the probability $p_{i'j}^{(\mu)}$ can be re-used having been previously calculated during the first random test. The probability $p_{ij'}^{(\mu)}$, however, must be evaluated:

$$p_{ij'}^{(\mu)} = \max\left\{0, 1 - \exp\left(-\beta\Delta\epsilon_{ij'}^{(\mu)}\right)\right\}. \tag{2.43}$$

where the energy identity $\Delta\epsilon_{ij'}^{(\mu)}$ is given by

$$\Delta\epsilon_{ij'}^{(\mu)} = \epsilon_{ij'}^{(\mu)} - \epsilon_{ij}^{(\mu)}. \tag{2.44}$$

Here $\epsilon_{ij}^{(\mu)}$ is again the pair-wise interaction energy between particles (i, j) in the current configuration μ. $\epsilon_{ij'}^{(\mu)}$ is the pair-wise interaction energy of particles (i, j) following the 'virtual move' of particle j.

2.4.2 Translational Moves

A particularly simple and efficient form of translational move is applied when the prospect of accepting cluster moves is expected to be high.[144] Following the selection of the random root particle, the translational move map M must be defined. M is given in the form of a displacement vector. The displacement in each dimension is given by a random number uniformly distributed over the interval $(-\delta, \delta)$, where δ is the maximum translation step size. Given the specification of M, particles are then selected to the cluster following the recursive selection process described previously.

A translational VMMC move is accepted provided during the recursive selection process no *frustrated* links are identified. For each translational move, N attempts to form and perturb a cluster are considered, each attempt beginning with a new random root particle and translational move map M.

2.4.3 Collective Rotational Moves

The rotational moves are not as straightforward as the translational moves, and it is possible that several hidden issues are encountered during collective rotation. However, by imposing additional conditions during the recursive selection process and ensuring all computations are undertaken with double precision floating point operations, such issues can be largely avoided.[144]

Again the rotational move must begin by first selecting a random root particle, where the position of the root particle is denoted as $\mathbf{r}_0$. A center of rotation is then defined as $\mathbf{r}_c = \mathbf{r}_0 + a\mathbf{u}$, where $\mathbf{u}$ is a random unit vector and a is a random number uniformly distributed over $[0, a_{\max}]$; here $a_{\max}$ is typically taken to be the particle diameter σ. A rotation matrix $\mathbf{R}$ is then obtained

corresponding to a rotation by an angle θ randomly drawn from the interval $(0, \theta_{\max})$ about a new random axis $\mathbf{u}^\star$, where $\theta_{\max}$ is the maximum rotational step size. Combining the centre of rotation $\mathbf{r}_c$ and the rotation matrix $\mathbf{R}$, one generates the rotational move map M. The application of the rotational move map M to the particle i, whose position is given by $\mathbf{r}_i$, can thus be expressed as $M\mathbf{r}_i = \mathbf{R}(\mathbf{r}_i - \mathbf{r}_c) + \mathbf{r}_c$. An equivalent rotation can be described by the quaternion $\mathbf{Q}_r = (\cos(\theta/2), \mathbf{u}\sin(\theta/2)$. The quaternion describing the orientation of particle i following the application of M can be obtained by the quaternion multiplication $\mathbf{Q}_r\mathbf{Q}_i$.

Having defined the rotational move map M, recursive cluster selection begins. This selection proceeds in the manner described previously, with the inclusion of additional tests on the interacting particle pairs (i, j). Before the two-step link formation is undertaken, an additional test for simulations of finite systems and an additional two tests for simulations of periodic systems are carried out. If the interacting pair (i, j) fails, it is labeled as *force failed*. The first test, common to both finite and periodic systems, assesses the maximum displacement size. For the particle j not already a member of the cluster, $M\mathbf{r}_j - \mathbf{r}_j$ is calculated. If the displacement ascertained is larger than σ, the pair (i, j) fails the test. The second test, necessary for periodic systems only, assesses the effect of the periodic boundaries on the potential cluster move. If the vector $\mathbf{r}_j - \mathbf{r}_c$ is greater that $L/4$, L being the box length, the second test is failed. Once (i, j) is labeled as a *force failed* pair, the recursive selection process does not continue onto the two-step link formation, but instead cycles, moving on to assess the remaining interacting particle pairs.

Following the recursive selection process for collective rotational moves, it is now possible that three types of interacting pairs, excluding those included in the cluster C, exist: *force failed*, *outright failed* and *frustrated* pairs. Again, if during the recursive selection process any *frustrated* links have been identified the rotational cluster move is rejected. In the absence of any *frustrated* links, the probability $W_{acc}^{(\mu\to\nu|R)}$ is generated from the *force failed* pairs B_f.

$$W_{acc}^{(\mu\to\nu|R)} = \min\left\{1, \prod_{(i,j)\in B_f} \exp(-\beta\epsilon_{i'j}^{(\mu)})\right\}. \tag{2.45}$$

The rotational cluster move is then only accepted if

$$X_3 < W_{acc}^{(\mu \to \nu | R)}, \tag{2.46}$$

where X_3 is a random number taken from a uniform distribution $U(0,1)$.

2.4.4 Benchmarking

Given the complexity of the VMMC algorithm, it was crucial to run some benchmarks with the implementation in `PaSSion`. **Figure 2.3** shows a set of radial distribution functions calculated from VMMC simulation runs as well as standard Monte Carlo simulation run for a system of $N = 2000$ Lennard-Jones particles in a cubic box under periodic boundary conditions. The VMMC simulations were performed using different move maps. The results are in agreement with each other, and also with what was reported in Ref. 144. In this thesis work, the VMMC algorithm was used to study the self-assembly of anisotropic colloidal particles both in finite and periodic systems. The simulations were undertaken in the NVT ensemble, with each VMMC cycle consisting of N translational or collective rotational cluster moves; the decision on undertaking a translational or collective rotational cluster move was taken at random with equal probabilities. A quaternion representation was used for the representation of orientational degrees of freedom.[153]

2.5 Umbrella Sampling

Umbrella sampling (US) is a rare event simulation technique,[154] which relies upon employing additional biasing potentials, known as *umbrella potentials*, to sample the free energy landscape. This technique allows the free energy profile $F(\xi)$ to be obtained along a chosen order parameter, or reaction co-ordinate ξ. To this end, multiple simulations are carried out in the presence of different biasing potentials V_j to probe the probability distribution along this reaction co-ordinate. The biasing potential $V_j(\xi)$ serves to confine the variations of ξ within a small interval around a prescribed value ξ_j, thereby enabling enhanced sampling in this region, called a *window*. Thus the umbrella sampling simulation for the j-th window is performed using the potential energy $U + V_j(\xi)$, where U is the total energy of the system in the absence

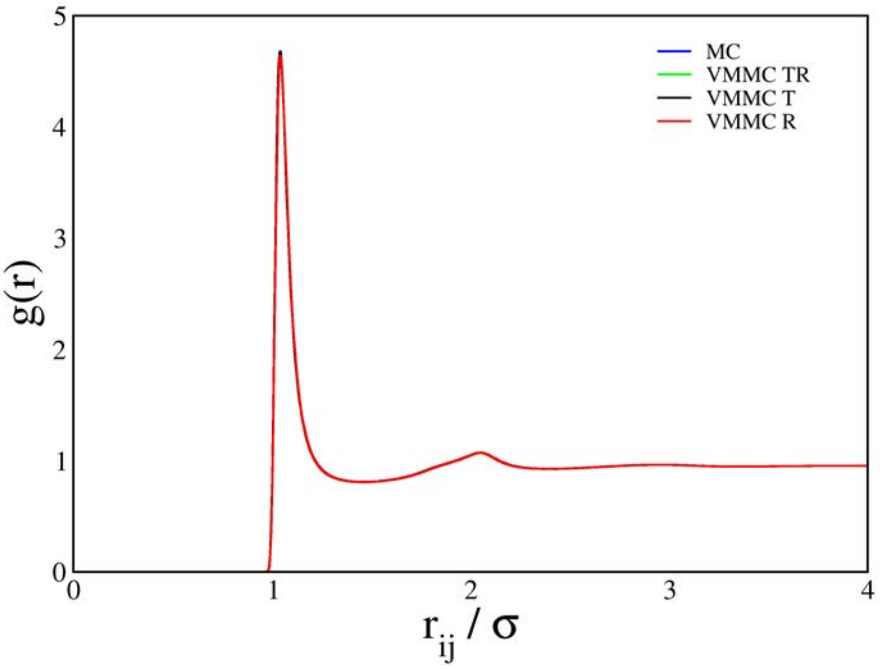

Figure 2.3: The radial distribution functions calculated from virtual-move Monte Carlo (VMMC) simulation runs as well as from a standard Monte Carlo (MC) simulation run for a periodic system of $N = 2000$ Lennard-Jones particles at the reduced temperature $T^\star = 0.6$ and the packing fraction $\phi = 0.225$. The data sets are from a standard MC simulation (blue - MC), VMMC simulation with only translational moves (black - VMMC T), VMMC simulation with only rotational moves (red - VMMC R), and VMMC simulation with both translational and rotational moves at equal probabilities (green - VMMC TR). The results are in agreement to such an extent that all lines are superimposed, leaving the VMMC R (red) plot predominantly visible.

of a bias. A reasonable choice for the biasing potentials are harmonic functions of the form $V_j(\xi) = \frac{1}{2}K(\xi - \xi_j)^2$, centred on successive values of ξ_j, where K is the spring constant. Although this choice is not a unique one, harmonic biasing potentials were used within this thesis.

After several windows (partially overlapping) spanning the reaction co-ordinate are sampled using the biasing potentials, the unbiased probability distribution can be obtained using, for example, the weighted histogram analysis method (WHAM).[155,156] This method essentially offers a scheme for "stitching" the biased probability distributions $\rho_j^{(b)}(\xi)$ from the umbrella sampling simulations together to yield a single unbiased probability distribution $P(\xi)$, which

then allows the free energy at temperature T to be estimated via the relationship

$$F(\xi_j) = -k_{\mathrm{B}}T \ln P(\xi_j), \tag{2.47}$$

where k_{B} is the Boltzmann constant. The *free energy difference*, $\Delta F_{\xi_i \to \xi_f}$, between an initial state, ξ_i, and a final state, ξ_f, is then given by

$$\Delta F_{\xi_i \to \xi_f} = F(\xi_f) - F(\xi_i) = -k_{\mathrm{B}}T \ln \left[\frac{P(\xi_f)}{P(\xi_i)} \right] \tag{2.48}$$

For a one-dimensional reaction co-ordinate ξ, the WHAM prescribes[156]

$$P(\xi) = \frac{\sum_{j=1}^{N_w} n_j \rho_j^{(b)}(\xi)}{\sum_{j=1}^{N_w} n_j e^{-\beta(V_j(\xi) - F_j)}} \tag{2.49}$$

$$e^{-\beta F_j} = \int e^{-\beta V_j(\xi)} P(\xi)\, d\xi, \tag{2.50}$$

where $\beta = 1/(k_{\mathrm{B}}T)$ and n_j is the number of snapshots used to construct $\rho_j^{(b)}$ for window j, for which F_j is a constant defined by Equation 2.50 and represents the free energy associated with the introduction of the umbrella potential. The WHAM equations, Equation 2.49 and Equation 2.50, are required to be solved self-consistently since the distribution function $P(\xi)$ itself depends on the set of the free energy constants F_j. In practice, an iterative procedure is followed.

2.6 Brownian Dynamics

The simulation of the dynamics of a colloidal suspension demands handling of widely disparate length and time scales. Brownian Dynamics (BD) is a computational technique extensively used to simulate the dynamics of colloidal particles in an implicit-solvent treatment, in which the fast time scale is eliminated at the expense of a random force in the equations of motion for slow-moving colloidal particles. We implemented a Brownian dynamics algorithm for spherical particles with a preferred body-fixed axis, ignoring hydrodynamic correlations and translation-rotation coupling.

This computational technique is underpinned by the Langevin equation:

$$m_i \frac{d\mathbf{v}_i}{dt} = -\zeta^{\mathrm{tr}}\mathbf{v}_i + \mathbf{F}_i(t) + \boldsymbol{\xi}_i^{\mathrm{tr}}(t) \tag{2.51}$$

where m is the mass of the colloidal particle i, $\mathbf{v}$ is its velocity at time t, ζ^{tr} is the friction coefficient, $\mathbf{F}(t)$ is a conservative force on the particle due to an effective potential and $\xi^{\mathrm{tr}}(t)$ is a fluctuating force responsible for Brownian motion. The superscript tr implies that the corresponding symbol refers to translational motion. Equation 2.51 is a stochastic differential equation because of the presence of the random force $\boldsymbol{\xi}_i^{\mathrm{tr}}(t)$. The first term on the right hand side of Equation 2.51 corresponds to a dissipative force induced by the viscous solvent. The friction coefficient for a spherical particle can be given by the Stokes law.

For independent rotational motion, the corresponding Langevin equation can be written as

$$I_i \frac{d\boldsymbol{\omega}_i}{dt} = -\zeta^{\mathrm{rt}}\boldsymbol{\omega}_i + \mathbf{T}_i(t) + \boldsymbol{\xi}_i^{\mathrm{rt}}(t), \tag{2.52}$$

where I_i is the moment of inertia of particle i, ω_i is its angular velocity, $\mathbf{T}_i$ is the torque acting on particle i, and ζ_i^{rt} is the rotational friction coefficient. In the absence of translation-rotation coupling, the frictional coefficients ζ^{tr} and ζ^{rt} are completely independent and are related to the translational and rotational diffusion coefficients, D^{tr} and D^{rt}, respectively by the generalised Einstein equations:

$$D^{\mathrm{tr}} = \frac{k_{\mathrm{B}}T}{\zeta^{\mathrm{tr}}} \qquad D^{\mathrm{rt}} = \frac{k_{\mathrm{B}}T}{\zeta^{\mathrm{rt}}} \tag{2.53}$$

The BD method neglects the inertial term in the Langevin equation and thus simulates trajectories on a time scale at which the momenta of the colloidal particles have relaxed. A BD trajectory can be simulated by the following prescription for the propagation of the translational and orientational co-ordinates over a time step Δt:

$$\mathbf{r}_i(t + \Delta t) = \mathbf{r}_i(t) + \frac{D_0^{\mathrm{tr}}}{k_{\mathrm{B}}T}\Delta t \mathbf{F}_i(t) + \boldsymbol{\xi}_i^{\mathrm{tr}} \tag{2.54}$$

$$\mathbf{e}_i(t + \Delta t) = \mathbf{e}_i(t) + \frac{D_0^{\mathrm{rt}}}{k_{\mathrm{B}}T}\Delta t \mathbf{T}_i(t) \times \mathbf{e}_i(t) + \boldsymbol{\xi}_i^{\mathrm{rt}} \times \mathbf{e}_i(t) \tag{2.55}$$

where $\mathbf{F}_i(t)$ and $\mathbf{T}_i(t)$ are, respectively, the force and the torque acting on particle i at time t and are given by

$$\mathbf{F}_i = -\boldsymbol{\nabla}_{\mathbf{r}_i} \sum_{j \neq i} U_{ij}(\mathbf{r}_{ij}, \mathbf{e}_i, \mathbf{e}_j) \tag{2.56}$$

$$\mathbf{T}_i = -\mathbf{e}_i \times \boldsymbol{\nabla}_{\mathbf{e}_i} \sum_{j \neq i} U_{ij}(\mathbf{r}_{ij}, \mathbf{e}_i, \mathbf{e}_j) \tag{2.57}$$

where D_0^{tr} and D_0^{rt} are, respectively, the translational and rotational diffusion coefficients at infinite dilution. The diffusion coefficients D_0^{tr} and D_0^{rt} are given by the Stokes law

$$D_0^{\mathrm{tr}} = \frac{k_{\mathrm{B}}T}{3\pi\eta\sigma} \qquad \text{and} \qquad D_0^{\mathrm{rt}} = \frac{k_{\mathrm{B}}T}{\pi\eta\sigma^3}, \tag{2.58}$$

where *sigma* is the diameter of the colloidal particle and η the viscosity coefficient of the solvent.

Here $\boldsymbol{\xi}_i^{\mathrm{tr}}$ and $\boldsymbol{\xi}_i^{\mathrm{rt}}$ are independent random displacements generated from Gaussian distributions with the following means and covariances:

$$\begin{gathered} \langle \boldsymbol{\xi}_i^{\mathrm{tr}} \rangle = 0, \quad \langle \boldsymbol{\xi}_i^{\mathrm{rt}} \rangle = 0 \\ \langle \boldsymbol{\xi}_i^{\mathrm{tr}} \cdot \boldsymbol{\xi}_j^{\mathrm{tr}} \rangle = 2\Delta t D_0^{\mathrm{tr}} \delta_{ij}, \quad \langle \boldsymbol{\xi}_i^{\mathrm{rt}} \cdot \boldsymbol{\xi}_j^{\mathrm{rt}} \rangle = 2\Delta t D_0^{\mathrm{rt}} \delta_{ij}. \end{gathered} \tag{2.59}$$

This set of stochastic displacements ensures the establishment of thermal equilibrium in the system by striking a balance between the random and frictional forces as prescribed by the fluctuation-dissipation theorem. After each step, the orientation vector $\mathbf{e}_i(t)$ is renormalised to retain the unit magnitude.

Within this thesis Brownian dynamics simulations are used to study the self-assembly of anisotropic colloidal particles in clusters and in the bulk. The simulations are undertaken in the canonical NVT ensemble. The anisotropic particles studied via Brownian dynamics simulations all display axial symmetry. Therefore, a unit vector description was used to represent the orientational degrees of freedom.

Chapter 3

Hierarchical Self-assembly of Colloidal Magnetic Particles into Reconfigurable Spheroidal Structures

3.1 Introduction

While buckministerfullerene is a classic example of a spheroidal molecule,[157] viral capsids with icosahedral symmetry showcase fascinating illustrations of molecular self-assembly into spheroidal structures in the realm of nature.[69] Hollow spheroidal structures, apart from their aesthetic appeal due to their high degree of symmetry,[158] have practical applications for their potential use as theranostic materials,[159] heterogeneous catalysts,[160] and metamaterials,[161] and thus serve as attractive targets for self-assembly at different length scales.[162–164] The ability to reconfigure such hollow spheroidal structures is critical to the design of responsive cages that can encapsulate guests and release them on demand.[165] However, realisation of such architectures with nanoscale or microscale building blocks has been elusive,[166] despite the promise of colloidal self-assembly,[167] spurred especially by a recent surge in the synthesis of an exotic variety of colloidal building blocks.[3,168] The key to the success of programmed self-assembly as a means of structure fabrication is the ability to encode the target structure into the building blocks.[167] The scope for tuning the interactions between the building blocks is critical to performing this task. Although colloidal building blocks are appealing from this perspective,[3,168] examples of colloidal self-assembly into target structures via *a priori* designed building blocks

are still rather limited.[55,59,94] Here we demonstrate *in silico* hierarchical self-assembly of rationally designed charge-stabilised colloidal magnetic particles into reconfigurable spheroidal structures.

We first describe the rationale that underpins our choice of building blocks in pursuit of targeted spheroidal assembly. Nanoscale and colloidal self-assembly can be governed by a multitude of forces.[6,169] While van der Waals interactions tend to favour close-packed structures,[170,171] the patchy colloids, which because of their heterogeneous surface chemistry offer highly directional interactions,[172] are known to stabilise low-coordinated structures.[59,94] Although computer simulation studies have now become indispensable for developing design principles, the complexity of the surface pattern predicted by *in silico* studies of patchy colloids is often beyond the reach of state-of-the-art experimental fabrication techniques.[173] A potential alternative to patchy colloids for stabilising low-coordinated structures is dipolar particles.[174,175] The common structural motifs observed for clusters of dipolar particles with a central dipole are linear chains, rings, and entangled knots for moderate strength of the dipole.[171,175] Dipolar colloidal particles thus appear to be promising building blocks for target structures that are non-close packed at the microscale. In particular, we considered charge-stabilised colloidal magnetic particles because of the scope for tuning the electrostatic and magnetic interactions independently in experimental conditions without recourse to involved chemistry.[175,176]

Self-assembly of nano- and micro-particles governed by magnetic interactions results in a rich variety of novel structures and phases.[177,178] Magnetic interactions can be due to permanent magnetic dipoles;[176,179] alternatively, uniaxial magnetic fields are commonly used to induce magnetic interactions in the absence of permanent dipoles,[55,180] though biaxial and triaxial magnetic fields have also been employed.[181,182] Until recently, the focus has been on dipolar interactions with an isotropic excluded volume,[177] for which the dipolar hard-sphere (DHS) model carrying a point-dipole at the centre has been extensively studied,[183] while soft interactions have also been considered.[184,185] The DHS model successfully captures the tendency for dipolar particles to form chains and rings.[183] While self-assembly into two-dimensional sheets has been observed for core–shell magnetic nanoparticles in the presence of an applied magnetic field,[186] superparamagnetic colloidal particles confined at air–water interface due to gravity have served as excellent models for two-dimensional systems.[187] A recent surge in the synthesis

of colloidal magnetic particles, where an additional anisotropy attribute exists due to either shape[55] or shift in the position of the dipole away from the centre of a spherical excluded volume,[176,188] or heterogeneous surface chemistry,[179,189] has brought about a paradigm shift in magnetic colloids with the prospect of realising complex architectures via their self-assembly.[190]

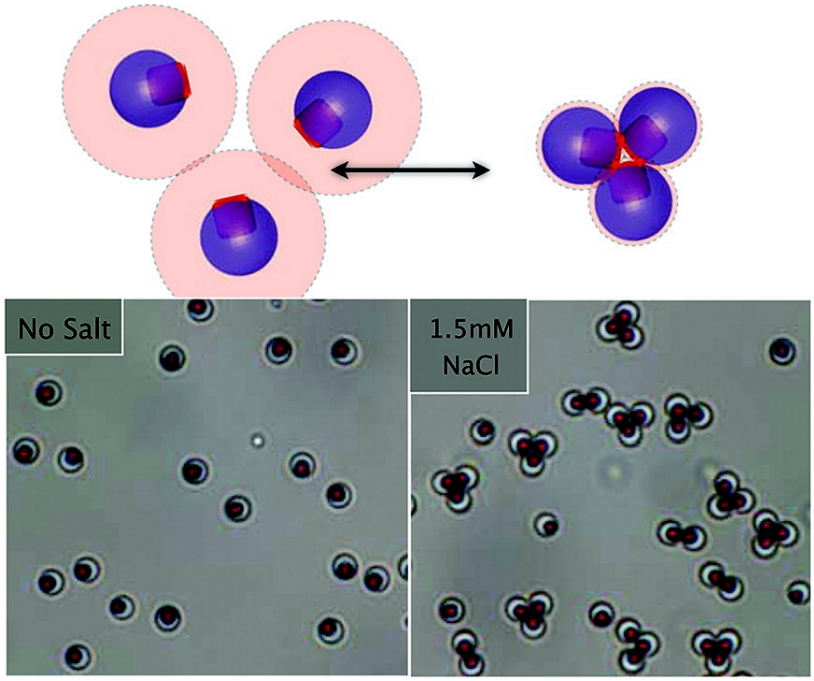

Figure 3.1: The self-assembly of colloidal magnetic colloidal particles recently synthesised by Sacanna *et al.*[176] Here, an iron oxide inclusion buried below the surface of an organosilica polymer sphere gives rise to magnetic interactions. The graphic schematically illustrates how, upon adding salt to the colloidal suspension, the range of the electrostatic repulsion between the particles is reduced and the self-assembly of trigonal planar motifs occurs. Copyright (2012) American Chemical Society.

In pursuit of the targeted spheroidal assembly we explored a route to surface curvature via edge sharing of polygons, as exemplified by Platonic and Archimedean solids.[191] The Platonic solids are convex polyhedra with equivalent faces comprised of congruent, regular convex polygons, where as the Archimedean solids are convex polyhedra formed of two or more distinct types of regular, convex polygons, meeting in identical vertices, i.e. having identical arrangements of the polygons about each vertex with sides all of the same length. A triangular face is the simplest of its kind, featuring in many of these uniform convex polyhedra. In order to facilitate the formation of triangular motifs, we focused on spherical charge-stabilised colloidal magnetic particles, where a dipole is embedded at a location shifted away from the centre. Such building blocks resemble closely the colloidal magnetic particles, realised recently using an iron oxide inclusion buried below the surface of an organosilica polymer sphere, that formed pla-

nar trimers upon tuning the electrostatic repulsion, as evident in **Figure 3.1**.[176] Our building block carries an off-centred dipole pointing radially outward.[192,193] Here, our results demonstrate hierarchical self-assembly of these colloidal building blocks into ground state structures that are topologically equivalent to the snub cube and the snub dodecahedron, the only two chiral Archimedean solids, for size-selected clusters. These spheroidal structures are shown to be reconfigurable by an external magnetic field, thus opening up the prospect of applications as responsive cages.

3.2 Methods

3.2.1 The Model

We employed a one-component treatment with an effective potential, widely used in colloid science,[194] to model the charge-stabilised colloidal magnetic particles and used basin-hopping global optimisation[24] to characterise the ground state structures. The spherical particles, with the centre of mass assumed to be at the centre, interact with each other via a screened electrostatic repulsion, given by the Yukawa potential.[194] In addition, an anisotropic site, located away from the centre in a rigid framework, holds a permanent point-dipole directed radially outward. A schematic illustration of the model charge-stabilised colloidal magnetic particles is shown **Figure 4.2**.

The potential energy V for a finite-sized system containing N charge-stabilised colloidal magnetic particles in the presence of a magnetic field is given by

$$\begin{aligned} V = & \sum_{i=1}^{N-1} \sum_{j=i+1}^{N} \epsilon_{\mathrm{Y}} \frac{\exp[-\lambda^{-1}(R_{ij} - \sigma)]}{R_{ij}/\sigma} \\ & + \sum_{i=1}^{N-1} \sum_{j=i+1}^{N} \frac{\mu_0}{4\pi} \frac{\mu_D^2}{r_{ij}^3} [(\hat{\boldsymbol{\mu}}_i \cdot \hat{\boldsymbol{\mu}}_j) - 3(\hat{\boldsymbol{\mu}}_i \cdot \hat{\boldsymbol{r}}_{ij})(\hat{\boldsymbol{\mu}}_j \cdot \hat{\boldsymbol{r}}_{ij})] \\ & - \mu_D \sum_{i=1}^{N} \hat{\boldsymbol{\mu}}_i \cdot \boldsymbol{B} \end{aligned} \tag{3.1}$$

Here, $\boldsymbol{R}_i$ and $\boldsymbol{r}_i$ are the position vectors for the centre of particle i and its embedded point-dipole, respectively, $\hat{\boldsymbol{\mu}}_i$ is the unit vector defining the direction of the dipole moment of the latter, whose magnitude is μ_D, and $\boldsymbol{r}_{ij}$ is the separation vector: $\boldsymbol{r}_{ij} = \boldsymbol{r}_i - \boldsymbol{r}_j$ with magnitude

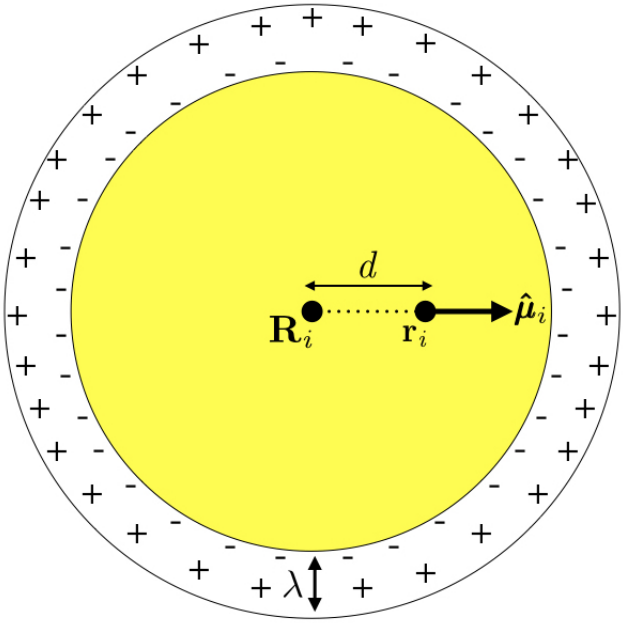

Figure 3.2: A schematic representation of the rationally designed model charge-stabilised colloidal magnetic particles. Here, $\boldsymbol{R}_i$ and $\boldsymbol{r}_i$ are the position vectors for the geometric centre of particle i and its embedded point-dipole, respectively, $\hat{\boldsymbol{\mu}}_i$ is the unit vector defining the direction of the dipole moment located at $\boldsymbol{r}_i$. λ is the Debye screening length, the characteristic length at which the electrostatic repulsion between two charge-stabilised particles decays.

r_{ij}, so that the unit vector $\hat{\boldsymbol{r}}_{ij} = \boldsymbol{r}_{ij}/r_{ij}$. In the Yukawa description of screened electrostatic repulsion, λ^{-1} is the inverse Debye screening length and ϵ_{Y} is the so-called contact potential. The units of energy and length are chosen as the Yukawa parameters ϵ_{Y} and σ, respectively. The direction of the external field $\boldsymbol{B} = (0, 0, B)$, when applied, was held fixed along the z-axis of the space-fixed frame. The magnetic dipole μ_D is given in reduced units of $(4\pi\epsilon_{\mathrm{Y}}\sigma^3/\mu_0)^{1/2}$ and the magnetic field strength B is in $[\epsilon_{\mathrm{Y}}\mu_0/(4\pi\sigma^3)]^{1/2}$, where μ_0 is the permeability of free space. The model parameters are then the inverse Debye screening length λ^{-1}, the strength of the dipole μ_D, the separation d between the location of the point-dipole and the centre of the particle, and the magnetic field strength B. The shift distance is expressed in terms of a dimensionless ratio $\alpha = 2d/\sigma$, where σ is the length scale in terms of which the Yukawa potential is defined, offering an estimate of the size of the particle in the absence of a hard core.

3.2.2 Simulation Details

Basin-hopping Global Optimisation

In order to elucidate the structures of colloidal clusters, the putative global minima on the potential energy surface were characterised by basin-hopping (BH) global optimisation,[24] as

described in **Chapter 2**. For the rigid-body description of the building blocks, the translational coordinates were represented by the Cartesian coordinates of the centre of the particle and the rotational coordinates by an angle-axis representation.[123] Although the latter representation introduces a redundant orientational degree of freedom for each axially symmetric particle in this case, it has certain numerical advantages in the context of geometry optimisation.[123] For a cluster of size N at least five independent basin-hopping global optimisation runs were performed starting from random initial structures and the lowest minimum found was proposed as the putative global minimum. Typically the convergence rate was between $80 - 100\%$ especially for smaller clusters.

Monte Carlo Simulations

We performed Monte Carlo (MC) simulations for a system of N particles in a canonical ensemble, employing a constraining radius and hence an accompanying constraining volume to avoid evaporation. The system was cooled starting from a random configuration. At each temperature, simulations were run for 10^7, 10^8 or 10^9 MC steps, half of which were for equilibration. As the temperature was lowered, the total number of MC steps was gradually increased. Each MC step consisted of N attempts for single-particle translational and rotational moves each. For MC simulation, a quaternion representation was used for rotational coordinates.[153] The temperature in the simulation is in the units of $\epsilon_{\mathrm{Y}}/k_{\mathrm{B}}$, k_{B} being the Boltzmann constant, and is referred to as the effective (or reduced) temperature. The step sizes were adaptive to achieve a target acceptance ratio of 0.45. At the lowest temperature, the translational step size was 2×10^{-2} in the reduced units, and the orientational step size was 1×10^{-2}.

3.2.3 Relative Shape Anisotropy Order Parameter

The relative shape anisotropy κ^2 is utilised to analyse and monitor the deviation from spherical symmetry for a distribution of charge-stabilised colloidal magnetic particles in MC simulations of colloidal clusters. The relative shape anisotropy is given by,

$$\kappa^2 = \frac{b^2 + (3/4)c^2}{R_g^4}. \tag{3.2}$$

Here, R_g is the radius of gyration, b is the asphericity and c the acylindricity, where

$$R_g^2 = \lambda_x^2 + \lambda_y^2 + \lambda_z^2, \tag{3.3}$$

$$b = \frac{3}{2}\lambda_z^2 - \frac{1}{2}R_g^2, \tag{3.4}$$

$$c = \lambda_y^2 - \lambda_x^2 \tag{3.5}$$

with λ_x^2, λ_y^2, λ_z^2 being the principal moments of the gyration tensor $\boldsymbol{S}$. The squared radius of gyration R_g^2 is a measure of the average size of a particular configuration. The shape anisotropy is defined as the traceless deviatoric part ($\hat{\mathbf{S}}$) of the gyration tensor $\mathbf{S}$:($\hat{\mathbf{S}}$) = $\mathbf{S} - (1/3)\mathrm{tr}(\mathbf{S})\mathbf{E}$, where $\mathbf{E}$ is the unit tensor. The relative shape anisotropy κ^2, as defined in Eq. (3.2), is dimensionless and provides a measure of shape. It has been previously utilised to characterise the shape of linear polymers during computer simulations.[195]

The relative shape anisotropy is bound between 0 and 1. When all particles are distributed in a spherically symmetric manner $\kappa^2 = 0$, if organised on a regular planar array such that the particles sit on the vertices of a regular polygon or form a homogeneously filled polygon $\kappa^2 = 0.25$ and if the particles of the system of interest are linearly distributed $\kappa^2 = 1$.

Brownian Dynamics Simulations

We performed Brownian Dynamics (BD) simulations in the over-damped limit without hydrodynamic interactions for finite-sized cluster of $N = 24$ particles. In simulations, the position and orientation of each particle were propagated following a widely used BD algorithm.[196] The translational and rotational diffusion coefficients at infinite dilution are given by appropriate Stokes' laws with sticky boundary conditions. For BD simulations, the time is expressed in the units of σ^2/D_0^t, where D_0^t is the translational diffusion coefficient at infinite dilution. Starting from low-energy structures obtained in MC simulations for the $N = 24$ cluster, several BD simulations were run at $T^\star = 0.1$ for 10^8 steps using the time step of $\Delta t = 10^{-5}$ in the reduced units. In real units, the total length of these simulation runs was estimated to be 10^3 s.

3.3 Results

3.3.1 Hierarchical Self-assembly of Hollow Spheroidal Structures

Optimal model parameters for charge-stabilised colloidal magnetic particles, maxmising the propensity to form triangular motifs, were identified. Here, the shift distance α was found to be the critical parameter. Utilising basin-hopping global optimisation, the lowest energy structures as a function of the shift distance α were identified for finite-sized clusters of $N = 2-6$ charge-stabilised colloidal magnetic particles. The remaining model parameters were fixed at: $\lambda^{-1} = 25$, $\mu_D = 2.0$ and $B = 0$. **Figure 3.3** exhibits the corresponding low energy structures. For $N = 2$ variation of α induced a significant change in the relative orientation of the two dipole moments; ranging from 180° for $\alpha = 0.6$ (**Figure 3.3a**) to 0° for $\alpha = 0.4$ (**Figure 3.3c**). As the cluster size is increased to $N = 3$ the triangular motif is the putative global minimum for all three α values. However, upon increasing the cluster size further to $N = 6$, the continued formation of triangular motifs is only observed for $\alpha = 0.6$. In addition, for $N = 6$ with $\alpha = 0.6$, the two trimers which constitute the lowest energy structure also edge share. Here, edge sharing is stabilised by a favourable anti-parallel arrangement of dipole moments between the adjacent triangular motifs, as seen in **Figure 3.3g**.

To confirm the identification of optimal parameters for the fabrication of triangular motifs, the relative stabilities of the global minima as a function of the cluster size were assessed. **Figure 3.4** shows the second finite difference of the energy for the global minimum of the cluster of size N, $\Delta_2 E(N)$, for $N = 2$–25 corresponding to a set of model parameters: $\lambda^{-1} = 25$, $\mu_D = 2.0$, $\alpha = 0.6$, and $B = 0$. Here $\Delta_2 E(N) = V_{min}(N-1) + V_{min}(N+1) - 2V_{min}(N)$, where $V_{min}(N)$ is the potential energy of the global minimum containing N particles. The pronounced peaks in the $\Delta_2 E$ versus N plot indicate especially stable structures for the corresponding cluster sizes. **Figure 3.4** shows that the trimer, i.e. $N = 3$ cluster is indeed especially stable for this set of parameters. The corresponding structure, stabilised by the dipolar interactions with an arrangement of the dipoles in a closed loop (i.e. flux-closure state),[197] is shown in **Figure 3.3d**. Although the dipoles and the centres of the particles are coplanar in this triangular structure of three-fold rotational symmetry, the dipoles are not directed along the line joining the centres. This set of parameters was chosen so that the propensity to form triangular

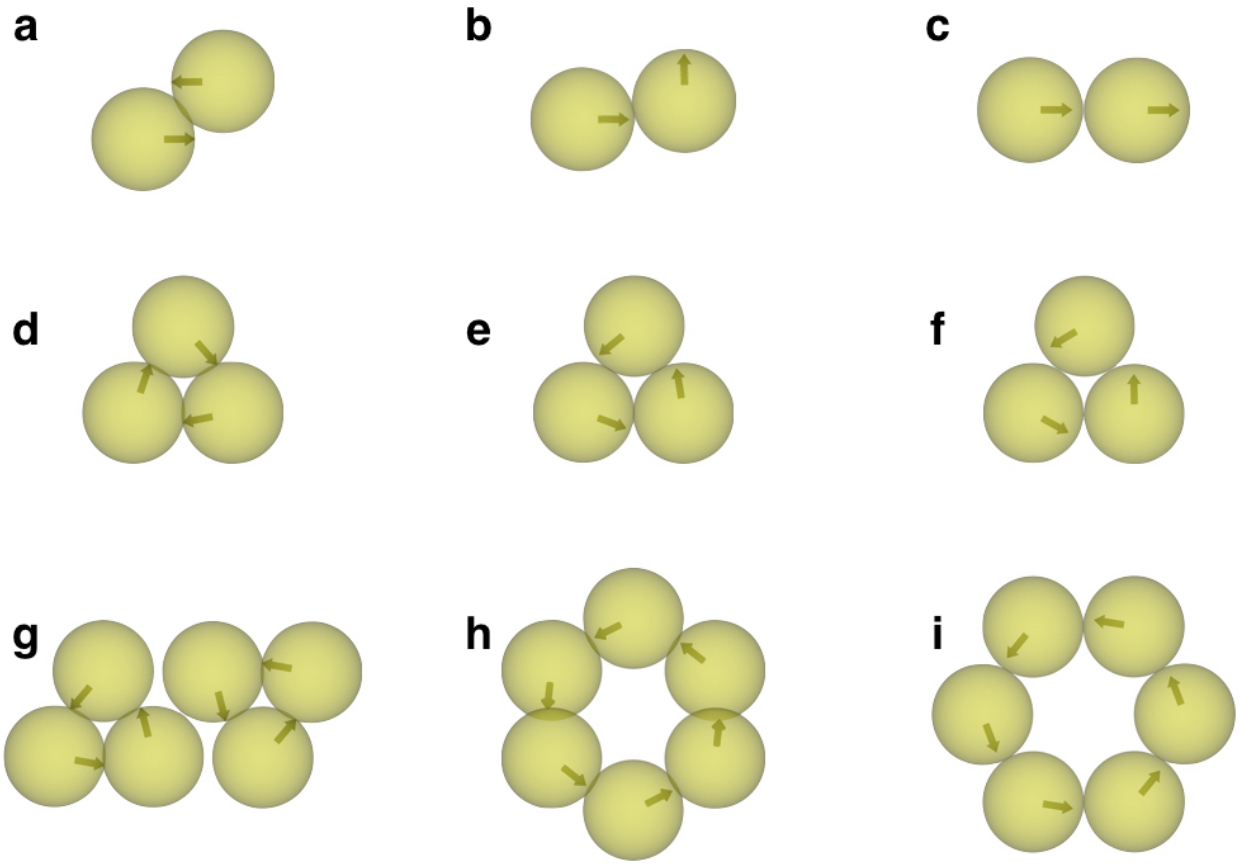

Figure 3.3: The optimisation of parameter space. In particular we focus on the variation of the parameter α. $\alpha = 0.6$ for the global minimum structures shown in **a**, **d** and **g**, $\alpha = 0.5$ for the global minima shown in **b**, **e** and **h**, while $\alpha = 0.4$ for structures **c**, **f** and **i**. Variation of the parameter α leads to a range of dipole-dipole orientations being stabilised as global minima for $N = 2$. While all α variations stabilise triangular units for cluster size $N = 3$, only for $\alpha = 0.6$ is the continued formation of triangular units, which in addition edge share, observed as the global minimum structure for cluster size $N = 6$.

subunits continued as apparent in the first place for the $N = 6$ cluster (**Figure 3.3g**). It is evident in **Figure 3.4** that the $N = 24$ cluster is substantially stable while the $N = 6$, 12, 15, and 18 clusters are somewhat stable as well. **Figure 3.5a**–**e** show the structures of the global minima for $N = 9$, 12, 15, 18 and 21 clusters, respectively, where a clear sign of hierarchical organisation of the triangular subunits, as seen in **Figure 3.3d**, is evident. Note that the hierarchical organisation resulted in bowl-shaped structures with emergent four-fold and five-fold rotational symmetry for $N = 12$ and $N = 15$, respectively; however, for $N = 18$ a planar structure was observed with six-fold rotational symmetry.

The surface curvature observed for the ground state structures of the $N = 12$, $N = 15$ and $N = 21$ clusters was promising for the spheroidal assembly of larger clusters. In a remarkable demonstration of hierarchical self-assembly, the ground state structure for the $N = 24$ cluster

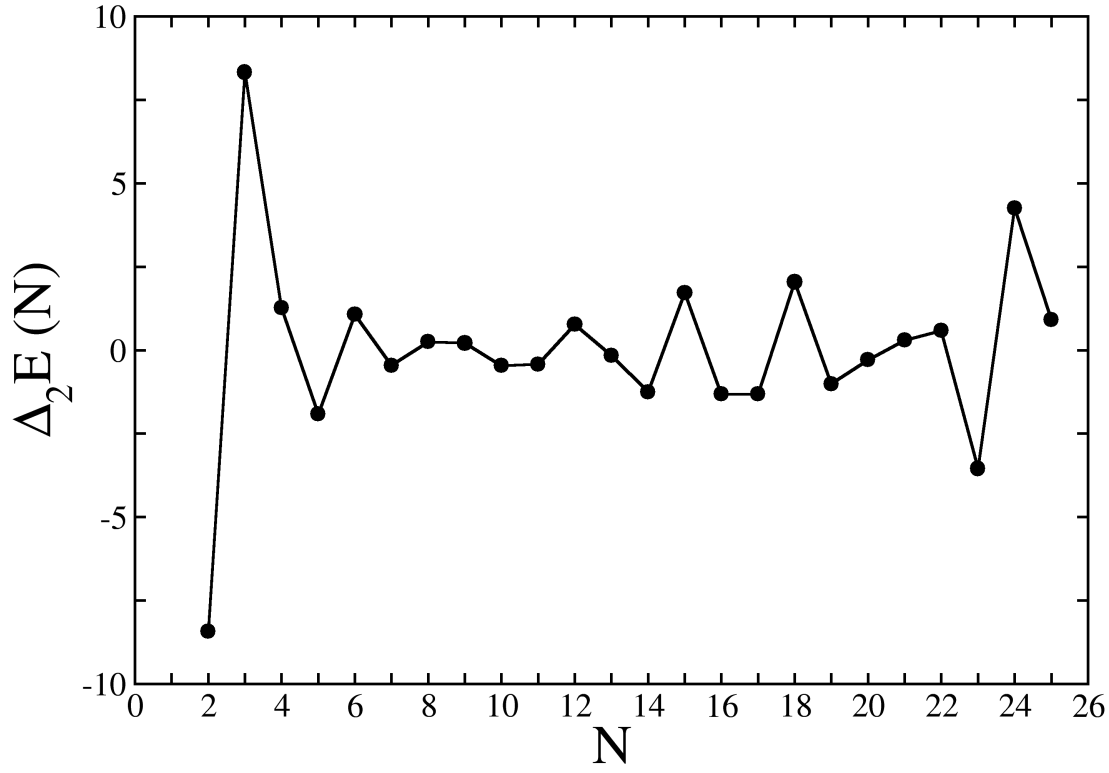

Figure 3.4: The second finite difference of potential energy for the putative global minimum of cluster size N, for $N = 2 - 25$.

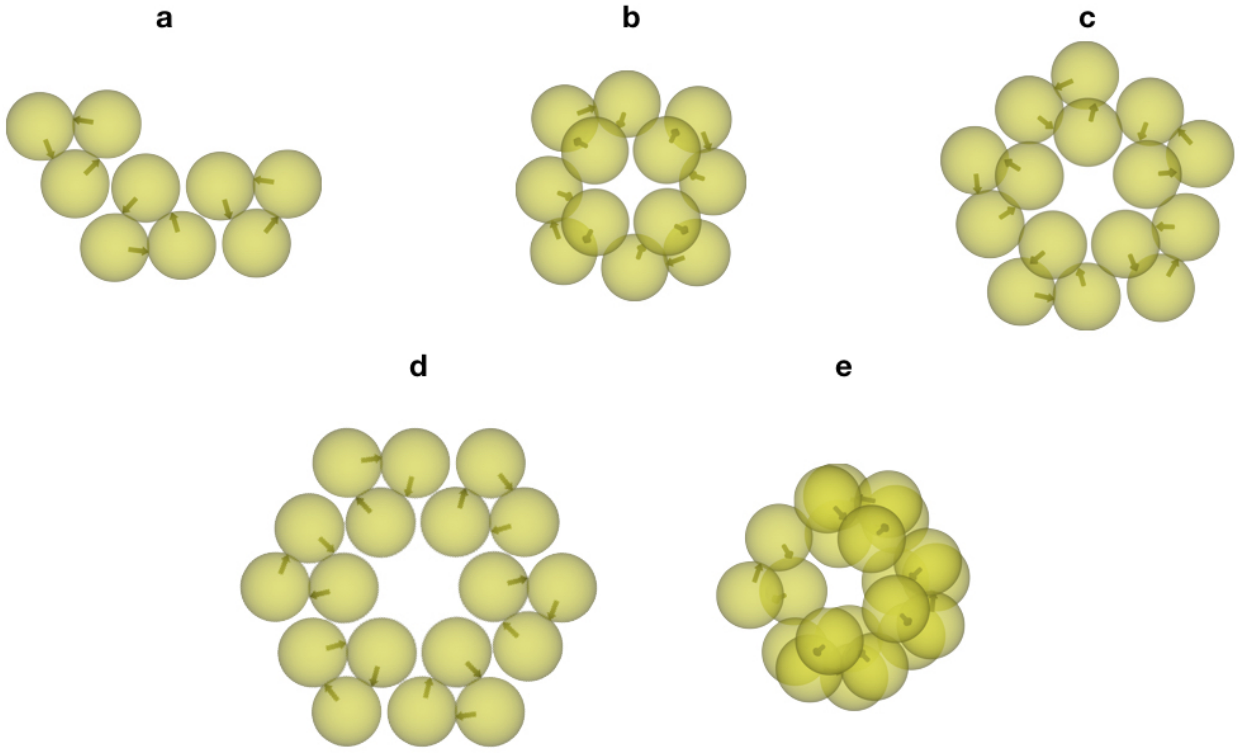

Figure 3.5: Structures of the global minima for clusters of size **a**. $N = 9$, **b**. $N = 12$, **c**. $N = 15$, **d**. $N = 18$ and **e**. $N = 21$.

was indeed found to be a closed shell with octahedral (O) symmetry, as shown in **Figure 3.6**. The structure is a non-uniform convex polyhedron composed of 32 triangular faces and 6 square faces and is topologically equivalent to a snub cube, a chiral Archimedean solid.[191] The polyhedron formed is topologically equivalent to the snub cube given that a continuous deformation will transform the structure into the snub cube. 8 of the triangular faces (yellow) originate from the colloidal particles forming triangular subunits of three-fold rotational symmetry, while the remaining faces emerge from the hierarchical self-assembly of these triangular subunits. It is noteworthy that the emergent triangular faces (blue) are distinct from the symmetrical triangular faces and have slightly different edge lengths. According to Kepler's description, a snub polyhedron is derived by expanding a regular polyhedron, moving the face apart and applying twists around their centres, adding new polygons centred on the original vertices and finally fitting pairs of triangles between the original edges.

Following the characterisation of the closed shell structure for the ground state of the $N = 24$ cluster, it was rational to expect a structure that is topologically equivalent to a snub dodecahedron for the $N = 60$ cluster if the observed trend continued. However, the search for such a structure, anticipated to be formed via hierarchical self-assembly governed by highly directional interactions, proved to be elusive. In order to improve the efficiency of the search for larger clusters, the trimeric subunits with three-fold rotational symmetry, as shown in **Figure 3.3d**, formed at the first stage of self-assembly for the $N = 24$ cluster were used as the building blocks instead. The effectiveness of this approach was assessed by examining the global minimum of the cluster of $N_t = 8$ such building blocks, which we call secondary building blocks as opposed to primary building blocks. The corresponding structure was also found to be of octahedral symmetry. When relaxed from this geometry, the $N = 24$ cluster with the primary building blocks was found to support the structure, shown in **Figure 3.6**. This observation validated our approach with secondary building blocks in the reduced configuration space.

Our hunt for a likely spheroidal structure for a cluster of $N = 60$ colloidal magnetic particles therefore continued with $N_t = 20$ secondary building blocks for global optimisation runs before relaxing the global minimum with 60 primary building blocks. For the same set of parameters, **Figure 3.7** presents the ground state thus identified for the $N = 60$ cluster – a closed shell polyhedral structure that is topologically equivalent to a snub dodecahedron. The structure

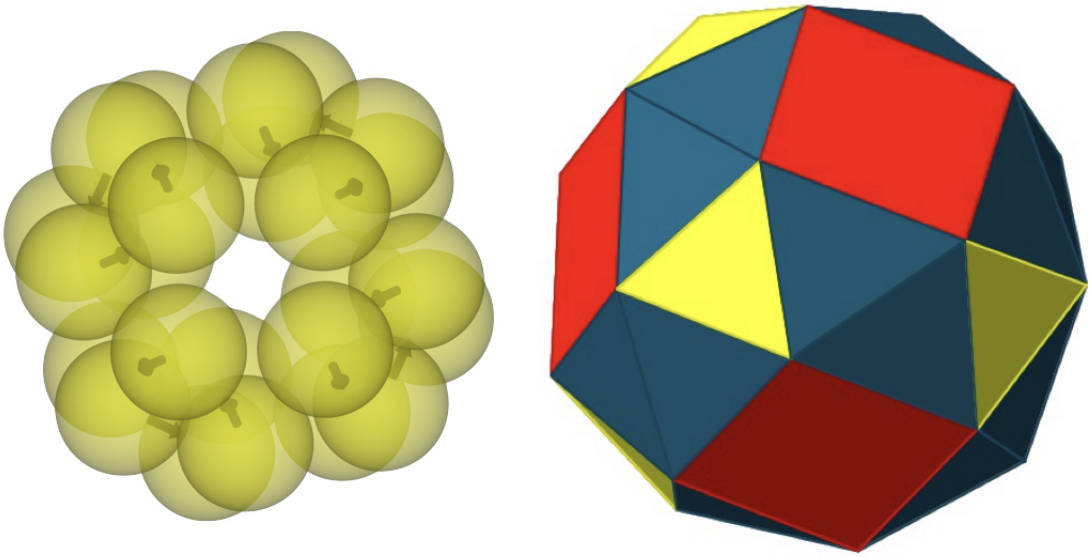

Figure 3.6: The structure of octahedral (O) symmetry, topologically equivalent to a snub cube, identified as the global minimum for the $N = 24$ cluster of charge-stabilised colloidal magnetic particles. Two representations of the same structure are shown: (left) spherical particles with embedded dipoles; (right) the non-uniform convex polyhedron with the faces colour-coded to distinguish between distinct faces. 8 of the triangular faces, shown in yellow, are sustained by the colloidal particles forming trimeric units of three-fold symmetry, while the rest of the faces are emergent from the hierarchical self-assembly of these trimeric units. The emergent triangular faces are in blue and the square faces are in red.

has icosahedral symmetry (I) and is composed of 80 triangular faces and 12 pentagonal faces. In this case, 20 of the triangular faces (shown in yellow), distinct from the 60 other triangular faces, are sustained by the colloidal particles forming triangular subunits of three-fold rotational symmetry, while the rest of the faces are emergent from the hierarchical self-assembly of these triangular subunits. As for the global minimum for the $N = 24$ cluster, the polyhedron is vertex-transitive but not uniform because of unequal edge lengths. Alongside the snub cube, the snub dodecahedron is a chiral Archimedean solid, existing in enantiomorphic forms. In fact, the snub dodecahedron can also be derived from the 120−vertex truncated icosidodecahedron by the process of alternation. Removal of alternate vertices leaves 60 of the vertices of the truncated icosidodecahedron to form a polyhedron topologically equivalent to one enantiomorphic form of snub dodecahedron. The other enantiomorphic form is formed by the set of other 60 vertices. The resulting polyhedron is vertex-transitive but not uniform, as shown in **Figure 3.7**, and requires some deformation to transform into a snub dodecahedron. Similarly, two enantiomorphic forms of snub cube can be derived from the 48-vertex truncated cuboctahedron.

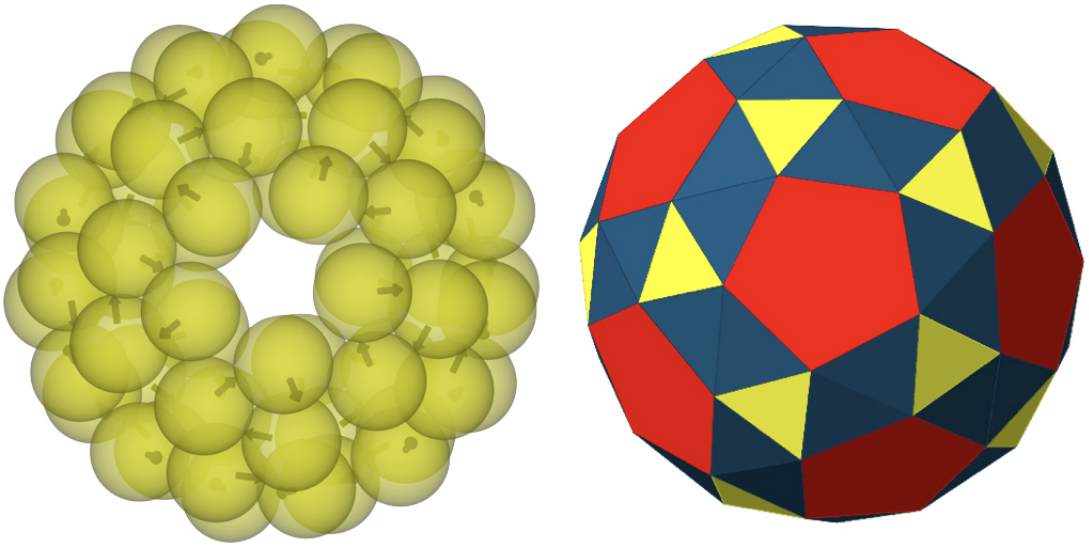

Figure 3.7: The structure of icosahedral (I) symmetry, topologically equivalent to a snub dodecahedron, identified as the global minimum for the $N = 60$ cluster of charge-stabilised colloidal magnetic particles. Two representations of the same structure are shown: (left) spherical particles with embedded dipoles; (right) the non-uniform convex polyhedron with the faces colour-coded to distinguish between distinct faces. 20 of the triangular faces, shown in yellow, are sustained by the colloidal particles forming triangular subunits of three-fold rotational symmetry, while the rest of the faces are emergent from the hierarchical self-assembly of these triangular subunits. The emergent triangular faces are in blue and the pentagonal faces are in red

We then examined the prospect of controlling the porosity of the spheroidal architectures by varying the salt concentration of the medium, which affects the inverse Debye screening length λ^{-1}. The spheroidal structures for the $N = 24$ and $N = 60$ clusters were observed to be stable as λ^{-1} was increased from $\lambda^{-1}\sigma = 20$ to $\lambda^{-1}\sigma = 50$. For $N = 24$, the edge length of the trimeric subunits was then found to increase by $\approx 6\%$, resulting in a decrease in the edge length of the emergent faces by $\approx 4\%$. The reduced softness of the repulsive core is the dominant factor here, though an increase in λ^{-1} also shortens the range of the electrostatic repulsion. Over this experimentally accessible regime, the radius of gyration for the spheroidal structure remained practically constant. The spheroidal structures were found to be stable for a reasonably wide range of μ_D values, but for a relatively narrow range of α values.

When subjected to an external magnetic field, the ground states of the $N = 24$ and $N = 60$ clusters retain their shell structures at low values for the field strength, but the symmetry is removed due to distortion. Above a threshold field, the shell structure collapses because of the tendency of the dipoles to align with the field. For strong fields, the interaction of the dipoles

with the field becomes dominant resulting in a linear chain aligned with the field. The hollow spheroidal structures, which enclose a well-defined space at the colloidal scale, can thus be reconfigured by the application of an external magnetic field above a threshold. This ability to reconfigure is critical to the design of responsive nano- or micro-cages capable of encapsulating guests and releasing them on demand.

The colloidal building blocks designed here are in close correspondence with the recently synthesised colloidal magnetic particles that used iron oxide inclusions located underneath the surface of the particles.[176] While achieving precise control over the direction of the dipole moment in an off-centred position is a challenge,[198] our model offers a design rule, which could be targeted realistically in pursuit of spheroidal self-assembly. As for the parameters, reasonable estimates in real units can be obtained by using $\epsilon_{\mathrm{Y}} = 4.1 \times 10^{-21}$ J (of the order of $k_{\mathrm{B}}T$ at room temperature) and $\sigma = 10^{-6}$ m. These values will correspond in real units to $\lambda = 40$ nm, $\mu_D \approx 4 \times 10^{-16}$ A m^2 and $B \approx 2 \times 10^{-4}$ T, calculated through considering the reduced units of $(4\pi\epsilon_{\mathrm{Y}}\sigma^3/\mu_0)^{1/2}$ and $[\epsilon_{\mathrm{Y}}\mu_0/(4\pi\sigma^3)]^{1/2}$ respectively. Given the magnetisation of hematite $M_{hem} \approx 2.2 \times 10^3$ A m^{-1}, such values are well within the experimental regime.[176,199] The value of the Yukawa contact potential ϵ_{Y} can be varied by an order of magnitude by controlling the colloidal charge number.[184]

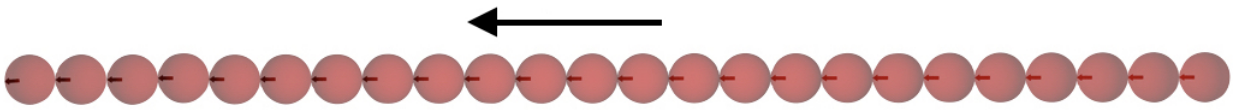

Figure 3.8: The structure identified as the global minimum for the $N = 24$ cluster of charge-stabilised colloidal magnetic particles in the presence of an applied magnetic field with strength, in reduced units, $B = 2.5$. Here, the arrow indicates the direction of the applied magnetic field.

3.3.2 Finite Temperature Study for Clusters of Charge-stabilised Colloidal Magnetic Particles

We now present our results of Monte Carlo (MC) simulations of the finite-sized systems. For $N = 24$ colloidal magnetic particles, which are the primary building blocks for the hollow

spheroidal structures reported here, we did not observe the formation of thermodynamically stable spheroidal structure even at effective temperature $T^\star = 0.1$ when the finite-sized system was gradually cooled starting from a random configuration. The single-particle MC moves that were attempted proved to be inadequate to make the thermodynamically stable structure accessible with the primary building blocks within the length of the MC runs. An estimate of dimensionless time, reduced by the self-diffusion coefficient at infinite dilution D_0 and particle diameter, per MC step can be obtained.[200] For micron-sized colloidal particles it is reasonable to consider $D_0 \approx 1 \times 10^{-12}$ m^2 s^{-1}.[201] The total length of the MC simulation run at the lowest temperature was thus estimated in real units to be of the order of hours ($\approx 3 \times 10^4$ s). In the context of hierarchical self-assembly, cluster moves, though unphysical,[200] could prove to be more efficient.[202] Alternatively, we carried out Brownian Dynamics (BD) simulations as they involve collective motion. When BD simulations were performed at $T^\star = 0.1$, the formation of more triangular subunits was indeed evident (**Figure 3.9**). However, the assembly of any spheroidal structure was not observed in the timescale of these BD simulations either. The formation of the thermodynamically stable spheroidal structure upon cooling is thus hindered by kinetic trapping, which frustrates the assembly process. The strongly directional dipolar interactions provide kinetic traps, presumably because of the propensity to form chains as opposed to triangular units in the flux-closure state.

Since our global optimisation results identified a well-defined structural motif as the secondary building block for the next level of structural hierarchy, we carried out MC simulations also with these secondary building blocks. The results are shown in **Figure 3.10**. In these MC simulation runs constrained in spherical containers of different sizes, the thermodynamically stable spheroidal structure was indeed found to be formed for $N_t = 8$ as the temperature was gradually lowered. Spherical containers of different sizes were used in order to show that the formation of the hollow spheroidal structure was not dependent on a restrictive container size. An increase in the container size leads to an increase in the volume that the particles can move in and thus an increase in the entropic penalty that the assembly into the snub cube structure would incur. This entropic penalty would need to be compensated by energetically favourable interactions for the assembly to take place. Therefore, a systematic decrease in the average temperature at which the formation of the hollow spheroidal structure is observed is to

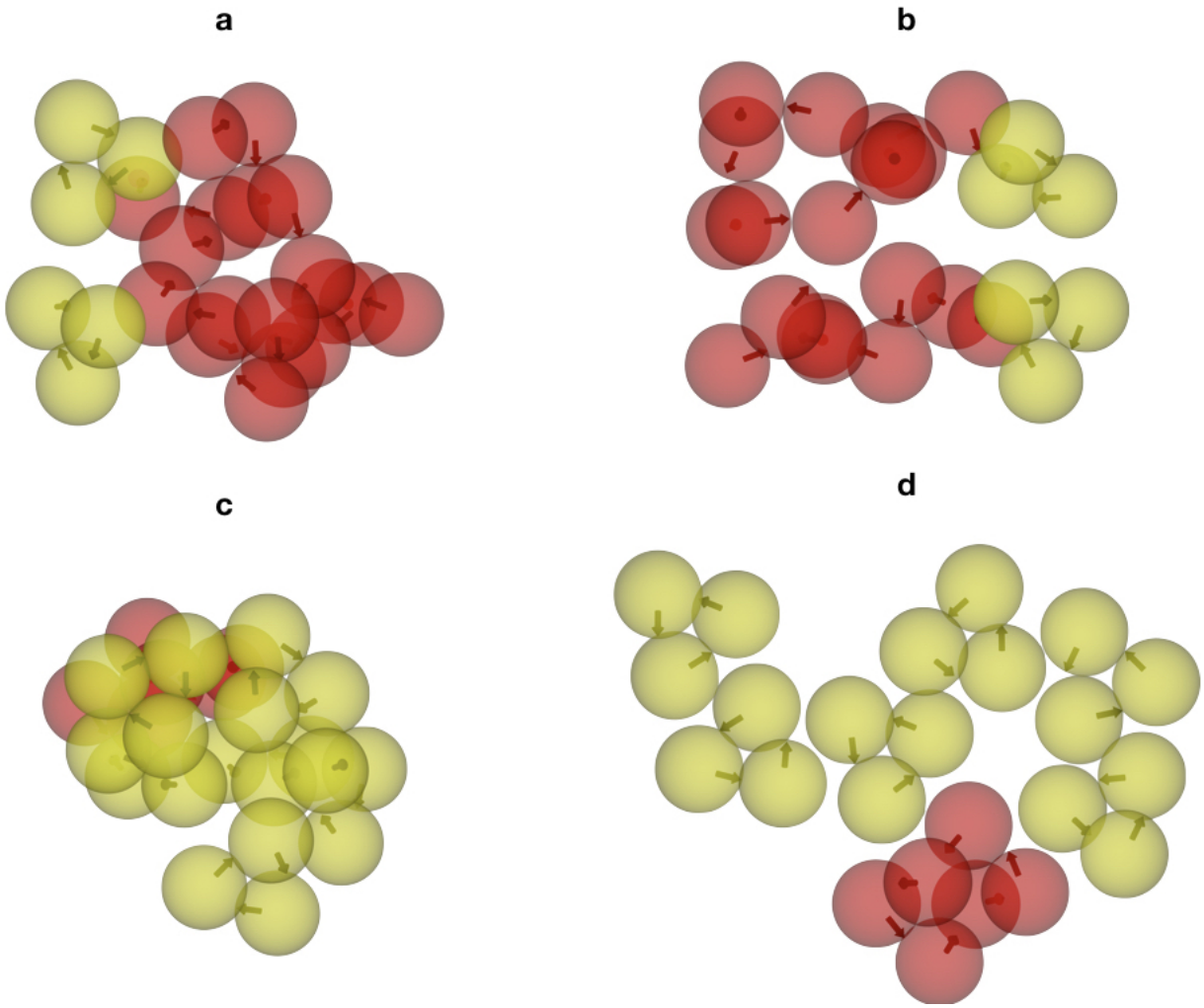

Figure 3.9: Representative low-temperature configurations for the 24-particle system obtained upon cooling from different Monte Carlo (MC) or Brownian Dynamics (BD) trajectories. **a.** MC at $T^\star = 0.1$; **b.** MC at $T^\star = 0.1$; **c.** BD at $T^\star = 0.1$; **d.** BD at $T^\star = 0.1$. The triangular subunits formed are shown in yellow.

be expected with increasing container size. However, **Figure 3.10** shows representative data from MC simulations for each container size as opposed to the average behaviour; therefore the expected trend is not clearly evident. A larger container volume would offer more flexibility in terms of the shape that the configurations can adopt, and thus one would expect that the error bars in the κ^2 versus $T^\star$ plot to increase as the size of the spherical container grows. A measure of the spherically symmetric distribution of the particles in the 24-particle cluster was estimated in terms of the relative shape anisotropy κ^2,[203] which is bounded between 0 and 1. $\kappa^2 = 0$ for a spherically symmetric distribution and $\kappa^2 = 1$ for a linear arrangement as in **Figure 3.8**. **Figure 3.10** shows the evolution of the relative shape anisotropy κ^2 as a function of effective temperature; a transition is marked by a fall in κ^2 to a value close to zero, indicating the formation of the spheroidal structure. The fall is relatively small for smaller

containers because of the restriction imposed. A similar observation was made for $N_t = 20$. The increase in the relative shape anisotropy κ^2, that occurs upon cooling the systems, can be plausibly explained by the formation of entropically favoured open bowl-like and planar structures, which are also energetically stabilised by anti-parallel arrangements of the dipoles in neighbouring trimers. Such structures tend to form first upon gradual cooling, before the closed snub cube structure is formed, resulting in the non-monotonic behavior of κ^2 observed.

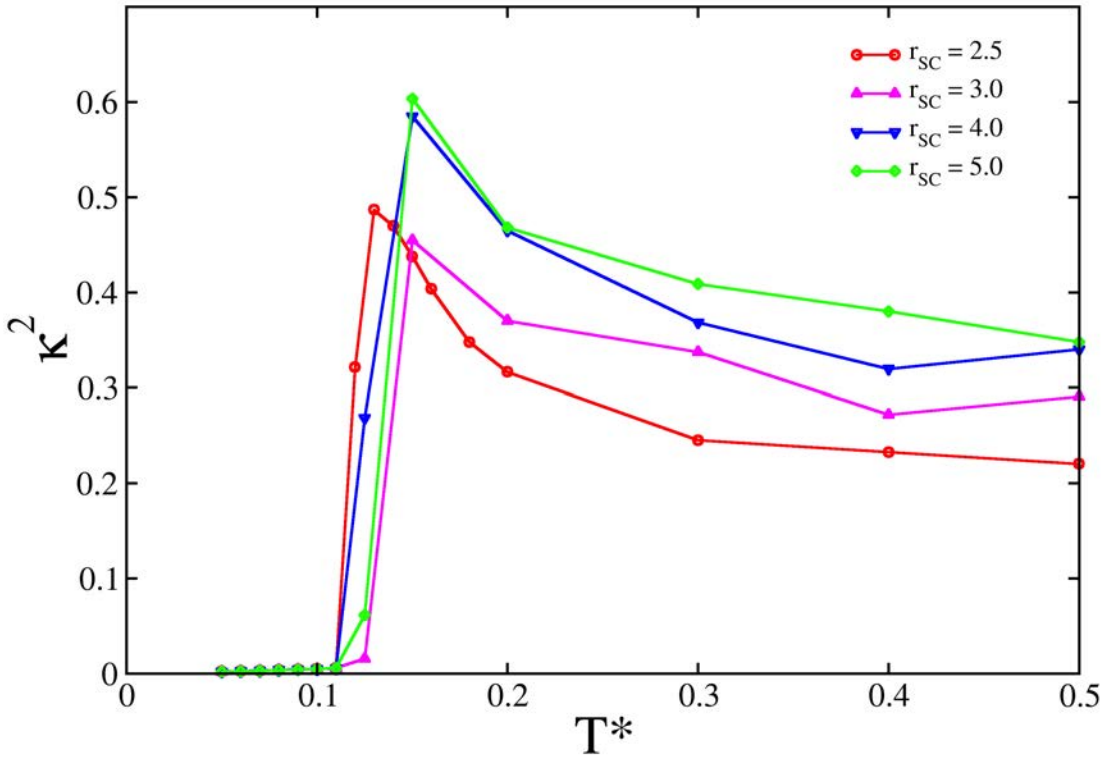

Figure 3.10: The relative shape anisotropy as a function of effective temperature for the finite-sized Monte Carlo simulation of $N_t = 8$ secondary building blocks. The radius of the spherical container r_{SC} is varied to highlight that self-assembly is independent of container size.

The present study highlights a critical aspect of programmed self-assembly that has received little attention until recently.[204–207] Here the task is to ensure that thermodynamically stable structures are kinetically accessible on the experimental time scale via removal of kinetic traps. Reversible association or contact formation allows for facile annealing of defects, and hence the removal of kinetic traps. Such reversibility is, however, often achieved at the expense of weak thermodynamic driving forces. It is relevant to note that this general idea has been corroborated, in particular, by a recent simulation study of a model of virus capsid assembly that employed rigid subunits corresponding to trimers of proteins.[204] The competing thermodynamic and kinetic criteria suggest that an optimal condition has to be established for efficient self-

assembly. In the presence of directional interactions, which strongly favour certain contacts, this task is even more challenging. One of the focal points of this thesis is to address this challenge in the context of hierarchical self-assembly.

3.4 Conclusions

In conclusion, we have demonstrated the rational design of colloidal magnetic particles which form thermodynamically stable hollow spheroidal structures via a remarkable hierarchical self-assembly. The ground state structures are topologically equivalent to the snub cube and the snub dodecahedron, the only two chiral Archimedean solids. The precision with which the sub-units are formed parallels nature's mastery of creating hierarchically organised complex architectures. The manipulation of the electrostatic repulsion between the charge-stabilised colloidal magnetic particles allows for the porosity of the spheroidal structures to be controlled. The structures are shown to be responsive to an external magnetic field. The ability to re-configure the hollow spheroidal structures is critical to the design of responsive supracolloidal cages for cargo delivery. The formation of thermodynamically stable spheroidal structures upon cooling is found to be hindered by kinetic trapping in the presence of the strongly directional dipolar interactions, presumably because of the propensity to form chains as opposed to triangular subunits. Here the term "kinetic trap" refers to a situation where relaxation of certain degrees of freedom occurs so slowly that access to the thermodynamically most favoured configuration is prevented on the timescale of observation. The presence of kinetic traps highlights the importance of the choice of optimal conditions for efficient self-assembly on the experimental timescale.

Chapter 4

Supracolloidal Reconfigurable Polyhedra via Hierarchical Self-assembly

4.1 Introduction

Self-assembly of colloidal particles offers a low-cost, scalable route to the bottom-up fabrication of three-dimensional structures because of the scope for tuning interparticle interactions.[167] Recent years have seen remarkable progress in the synthesis of a wide variety of complex colloidal particles,[3,168,208] which interact via a multitude of forces.[169] Thanks to this progress, hierarchical self-assembly for synthetic anisotropic colloidal building blocks, though still at an early stage of exploration, promises to open up routes to structural complexity at an unprecedented level.[66,98,209] While examples of structural hierarchies in nature are abundant,[210] encoding structural hierarchy for man-made functional materials has been elusive. This multiscale design problem faces a significant challenge to overcome any kinetic traps that may arise, especially in the presence of relatively strong interactions between anisotropic colloidal building blocks in certain directions.[66] Understanding the pathways for hierarchical self-assembly is thus crucial to mitigate this challenge.[211,212]

Hollow structures find a myriad of practical applications predominantly for their ability to encapsulate guests and thus have been targets for self-assembly at different length scales.[67,162–164,213] In **Chapter 3**, we explored a biomimetic design route to hollow spheroidal

structures at the microscale,[66] drawing inspiration from the intricate self-assembly of spheroidal shells with icosahedral symmetry observed for many viral capsids in the realm of nature.[69] These spheroidal shells exhibit a spectacular structural hierarchy, where the surface curvature emerges from the edge-sharing of polygons, as in the so-called Platonic and Archimedean solids.[191] Our approach to produce hollow spheroidal structures exploited designer colloidal magnetic particles, which, for size-selected clusters, formed thermodynamically stable polyhedra: a polyhedron of octahedral symmetry, topologically equivalent to the snub cube, for $N = 24$ particles and a polyhedron of icosahedral symmetry, topologically equivalent to the snub dodecahedron, for $N = 60$. In a remarkable display of structural hierarchy, the colloidal magnetic particles formed uniform triangular subunits at an intermediate level, while the ordered arrangement of these planar trimers at the next level resulted in the formation of each of these polyhedra with emergent faces.[66] It is relevant to note here that the snub cube and snub dodecahedron are the only two Archimedean solids which are chiral, despite having a high degree of rotational symmetry.[191] Together with the snub tetrahedron, they complete the set of convex snub polyhedra.[191] In **Table** 4.1 a comparison of the geometric features of this set of convex polyhedra is presented.

Polyhedron	Symmetry	V	F	E
Snub Tetrahedron	T	12	20	30
Snub cube	O	24	38	60
Snub dodecahedron	I	60	92	150

Table 4.1: A comparison of the geometric features of convex snub polyhedra. Here V is the number of vertices, F is the number of faces and E denotes the number of edges.

Our designer building blocks, which included a permanent point-dipole shifted away from the centre,[66] closely resemble the micron-sized colloidal magnetic particles, synthesised using a single-domain hematite cube inclusion underneath the surface of an organosilica polymer sphere.[176] When the range of the electrostatic repulsion between these colloidal particles was reduced by modulating the salt concentration of the medium, the particles were indeed found to form planar trimers. However, the direction of the dipole moment within the magnetic cube was not known with certainty in this experimental system.[214] In the building blocks that we considered the point-dipole was directed radially outward and thus the building blocks were cylindrically symmetric.[66] In fact, magnetic particles with off-centred dipoles have drawn

special interest in computer simulation studies,[66,192,214–216] relevant to the synthesis of a variety of exotic colloidal magnetic particles in recent years.[176,188,189,217]

As captured by our designer colloidal magnetic particles,[66] the trimers were the dominant structural motifs in the experimental study by Sacanna *et al.*[176] However, the formation of tetramers was also occasionally observed in this experimental system, as shown in **Figure 4.1**. In this context, a relevant question is whether we can design structural hierarchy with tetramers at the intermediate level. Another particularly pertinent question relates to the mechanism of self-assembly when it results in structural hierarchy at multiple levels. These questions provided the motivation for the present study, where we also intended to examine the possibility of encoding self-assembly of designer colloidal magnetic particles into the snub tetrahedron or its topological equivalent. In relation to the mechanism of hierarchical self-assembly, we intended to investigate, in particular, whether or not the emergence of structural hierarchy at multiple levels involves hierarchical pathways, i.e. proceeds in stages.[218]

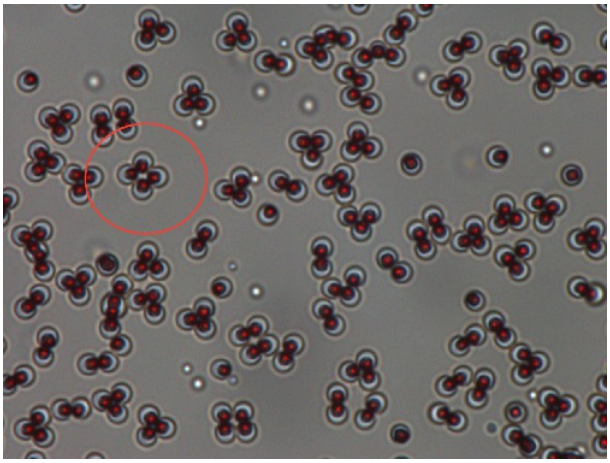

Figure 4.1: The self-assembly of charge-stabilised colloidal magnetic particles recently synthesised by Sacanna *et. al.* Here, the colloidal magnetic particles are shown to self-assemble into a square planar motif. Reproduced with the permission of Dr. S. Sacanna (*Private communication*).

In order to address these questions, we employed a sophisticated structure prediction tool, a rare-event simulation technique and a Monte Carlo simulation method. Here we demonstrate the self-assembly of designer charge-stabilised colloidal magnetic particles with off-centred dipoles into a series of reconfigurable supracolloidal polyhedra and elucidate distinct kinetic pathways for self-assembly into two of these polyhedra of very different morphologies. These polyhedra each display a remarkable two-level structural hierarchy involving either a tetramer or a trimer at the intermediate level.

4.2 Methods

4.2.1 The Model

We employed the widely-used one-component description for our colloidal system with an effective potential. The spherical magnetic particles that we considered in this study interact with each other via the Yukawa potential describing the screened electrostatic repulsion that offers the charge-stabilisation. The magnetic interactions are described within a point-dipole approximation; a permanent point-dipole is placed away from the centre of the spherical core in a rigid framework.

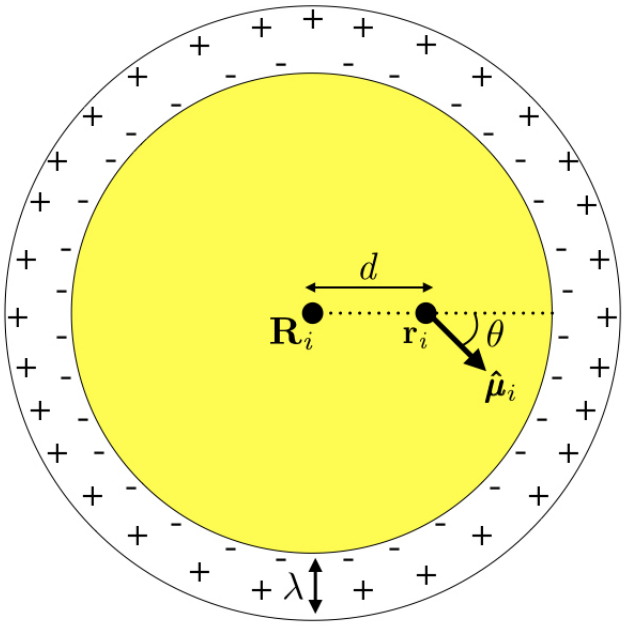

Figure 4.2: A schematic representation of the rationally designed model charge-stabilised colloidal magnetic particles. Here, $\boldsymbol{R}_i$ and $\boldsymbol{r}_i$ are the position vectors for the geometric centre of particle i and its embedded point-dipole, respectively, $\hat{\boldsymbol{\mu}}_i$ is the unit vector defining the direction of the dipole moment located at $\boldsymbol{r}_i$. θ defines the angle between the shift vector, $\boldsymbol{r}_i - \boldsymbol{R}_i$, and the unit vector describing the dipole orientation, $\hat{\boldsymbol{\mu}}_i$. λ is the Debye screening length, which provides an estimate of the thickness of the electrostatic double layer. The addition of the parameter θ allows the variation of dipole orientation within the rigid-body model.

The potential energy V for a cluster of N charge-stabilised colloidal magnetic particles in

the presence of a magnetic field is then given by,

$$
\begin{aligned}
V = & \sum_{i=1}^{N-1} \sum_{j=i+1}^{N} \epsilon_{\mathrm{Y}} \frac{\exp[-\lambda^{-1}(R_{ij}-\sigma)]}{R_{ij}/\sigma} \\
& + \sum_{i=1}^{N-1} \sum_{j=i+1}^{N} \frac{\mu_0}{4\pi} \frac{\mu_D^2}{r_{ij}^3} [(\hat{\boldsymbol{\mu}}_i \cdot \hat{\boldsymbol{\mu}}_j) - 3(\hat{\boldsymbol{\mu}}_i \cdot \hat{\boldsymbol{r}}_{ij})(\hat{\boldsymbol{\mu}}_j \cdot \hat{\boldsymbol{r}}_{ij})] \\
& - \mu_D \sum_{i=1}^{N} \hat{\boldsymbol{\mu}}_i \cdot \boldsymbol{B}
\end{aligned}
\tag{4.1}
$$

Here, $\boldsymbol{R}_i$ and $\boldsymbol{r}_i$ are the position vectors for the centre of particle i and its embedded point-dipole, respectively, $\hat{\boldsymbol{\mu}}_i$ is the unit vector defining the direction of the dipole moment of the latter, whose magnitude is μ_D, μ_0 is the permeability of free space, and $\boldsymbol{r}_{ij}$ is the separation vector: $\boldsymbol{r}_{ij} = \boldsymbol{r}_i - \boldsymbol{r}_j$ with magnitude r_{ij}, so that the unit vector $\hat{\boldsymbol{r}}_{ij} = \boldsymbol{r}_{ij}/r_{ij}$. In the Yukawa description of screened electrostatic repulsion, λ^{-1} is the inverse Debye screening length and ϵ_{Y} is the so-called contact potential. The units of energy and length are chosen as the Yukawa parameters ϵ_{Y} and σ, respectively. The direction of the external field $\boldsymbol{B} = (0, 0, B)$, when applied, was held fixed along the z-axis of the space-fixed frame. The magnetic dipole μ_D is given in reduced units of $(4\pi\epsilon_{\mathrm{Y}}\sigma^3/\mu_0)^{1/2}$ and the magnetic field strength B is in $[\epsilon_{\mathrm{Y}}\mu_0/(4\pi\sigma^3)]^{1/2}$. The model parameters are then the inverse Debye screening length λ^{-1}, the strength of the dipole μ_D, the separation d between the location of the point-dipole and the centre of the particle, the angle θ between the direction of the dipole moment $\hat{\mu}_i$ and the shift vector $\boldsymbol{r}_i - \boldsymbol{R}_i$ as shown in **Figure 4.2**, and the magnetic field strength B. The shift distance is expressed in terms of a dimensionless ratio $\alpha = 2d/\sigma$, where σ is the length scale in terms of which the Yukawa potential is defined, offering an estimate of the size of the particle in the absence of a hard core. In **Chapter 3**, we considered the $\theta = 0°$ case, where the point-dipole points radially outward.

The colloidal magnetic particles were treated as rigid bodies. The translational coordinates for the centre of the particles were represented by the Cartesian coordinates and the rotational coordinates by an angle-axis representation,[123] unless specified otherwise. The gradients and the Hessian were obtained analytically whenever necessary.

4.2.2 Simulation Details

Basin-hopping Global Optimisation

We used basin-hopping (BH) global optimisation method,[24,132] to characterise the putative global minimum on the potential energy landscape (PEL) for each cluster size. For each cluster size, five independent BH global optimisation runs were performed starting from random initial configurations and the lowest minimum found was proposed as the putative global minimum. In this study, the global minima are presented with high confidence level with 100% convergence up to $N = 21$. For $N = 24$, the tetramer with four-fold rotational symmetry, as shown in **Figure 4.3**, were used as a rigid building block to improve the efficiency of search. The global minimum thus obtained was relaxed for the individual colloidal magnetic particles with $\theta = 90°$ by removing the constraints.

Rare-event Simulation

In order to obtain kinetic pathways for structural transitions, we employed discrete path sampling (DPS),[219] as implemented in the software PATHSAMPLE, which drives the program OPTIM. The DPS approach to rare-event simulation relies upon recursive use of geometry optimisation to grow a database of minima and transition states. In this method, an initial path between two selected minima, generally consisting of a series of intervening transition states and minima, is determined by repeated use of double-ended transition state searches. The doubly nudged elastic band (DNEB) algorithm[220,221] is used to identify transition state candidates, which are then accurately refined using hybrid eigenvector-following techniques.[222] The eigenvalue shifting technique is used for treatment of the six degrees of freedom associated with overall translation and rotation in transition state searches. The technique uses analytic expressions for the corresponding Hessian eigenvectors with zero eigenvalues. The DNEB implementation uses a discrete representation of the band in terms of a set of images, obtained by an incremental approach to quaternion interpolation algorithm Slerp.[223]

The two minima reached by (approximate) steepest-descent paths leaving a transition state parallel and anti-parallel to the eigenvector with the unique negative eigenvalue define its connectivity. For local minimisations the limited-memory Broyden–Fletcher–Goldfarb–Shanno (LBFGS) algorithm of Liu and Nocedal is used.[224,225] Discrete paths are then generated sys-

tematically from the initial connected path to grow the database by adding all the distinct minima and transition states found during successive connection-making attempts for pairs of minima selected using a missing connection algorithm.[226] The addition of new stationary points to the database critically depends on reliable identification of permutation-inversion isomers. The discrete path that makes the largest contribution to the two-state rate constant within a steady-state approximation for the intervening minima is extracted from the DPS database using a network formulation[227] via Dijkstra's shortest-path algorithm[228] by choosing suitable edge weights.[219]

Monte Carlo Simulations

A series of Monte Carlo (MC) simulations were performed within two different constraining spherical volumes starting from five independent configurations. In a given run, the reduced temperature of the system of $N_s = 4$ rigid building blocks was gradually decreased. For each rigid body, the translational degrees of freedom were represented by the Cartesian coordinates of the geometric centre and a quaternion representation was used to describe the orientational degrees of freedom.[229] The step sizes in both translational and orientational space were adapted to secure an average acceptance ratio of 0.45 except at relatively high reduced temperatures. At each temperature, simulations were run at least for 10^9 MC cycles (2×10^9 cycles at low temperatures), each of which consisted of N_s single-particle moves in both translational and orientational space; half of these cycles were used for equilibration. Here $T^\star$ is the reduced temperature given by $T^\star = k_\mathrm{B}T/\epsilon_\mathrm{Y}$.

4.3 Results

4.3.1 The Rational Design of Hollow Tubular Structures

In our quest for hierarchical self-assembly via tetramers, square planar units appeared to be plausible secondary building blocks, which could support a flux-closure arrangement of dipoles, as opposed to tetrahedra. We therefore considered the $\theta = 90^\circ$ case and varied the parameter α in particular. By employing basin-hopping global optimisation, we characterised the global minima on the PELs for clusters of these colloidal particles as the thermodynamically

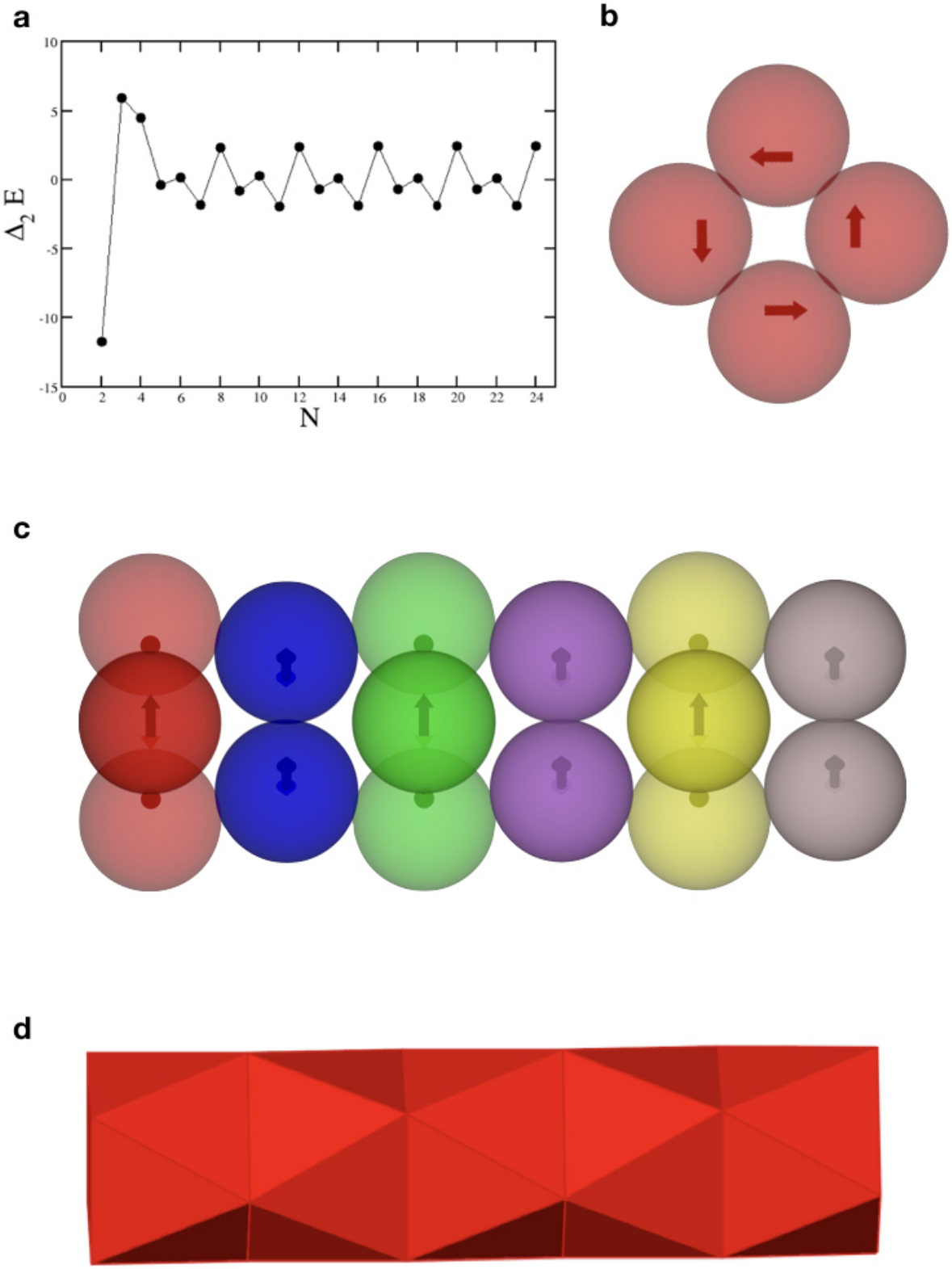

Figure 4.3: **a**. The second finite difference of the potential energy for the global minimum of cluster size N as the cluster size grows spanning the range N = 2–24. **b**. The structure of the global minimum for N = 4. **c**. The structure of the global minimum for N = 24. **d**. The polyhedral representation, showing the emergent triangular faces for N = 24, clearly demonstrates the anti-prismatic arrangement.

favoured structures especially at low reduced temperatures. **Figure 4.3a** shows the second finite difference of the potential energy for the global minimum as a function of the cluster size N, $\Delta_2 E(N)$ for $N = 2 - 24$. Here $\Delta_2 E(N) = V_{min}(N-1) + V_{min}(N+1) - V_{min}(N)$, where $V_{min}(N)$ is the potential energy of the global minimum for a cluster of N particles. The plot corresponds to the following set of parameters: $\theta = 90°$, $\alpha = 0.3$, $\mu_D = 2.0$ and $\lambda^{-1} = 25$. The plot features pronounced peaks for certain values of N, indicating especially stable structures for the corresponding cluster sizes. It is then evident that the structures for the cluster sizes, which are integer multiples of 4, are especially stable. This could be a sign of structural hierarchy, which was indeed confirmed by the inspection of the structures. **Figure 4.3b** exhibits the 4-particle global minimum for the aforementioned parameter set. The global minimum in this case is indeed a square planar unit, stabilised by the dipoles arranged in a flux closure state. The disposition to form tetrameric subunits continued with increasing N. These square planar subunits stack on top of each other to form a tubular structure in a striking display of structural hierarchy as evident in **Figure 4.3c** for $N = 24$. As N increases in integer multiples of 4, the number of square planar subunits grows resulting in an increase in the length of the tube and the global minima are of D_{4d} symmetry. The polyhedral representation in **Figure 4.3d** shows the triangular faces that are emergent from this hierarchical self-assembly and clearly demonstrates the anti-prismatic arrangement.

We characterised a dominant pathway for the self-assembly into the tubular structure for $N = 16$ by employing discrete path sampling approach to rare event simulation.[123,219,230] The dominant pathway is taken to be the discrete path that makes the largest contribution to the two-state rate constant (see section 4.2.2). The energy profile of the dominant pathway for the self-assembly starting from a high-energy, relatively disordered minimum that we obtained in this case is shown in **Figure 4.4a** (see Movie 1 in the electronic supplimentary information of Ref.[68]) for the complete pathway. This pathway involves the formation of the square planar units as the secondary building blocks and demonstrates that as the square planar subunits are formed, they attach to a growing tubular structural motif practically one by one (D, E and F in **Figure 4.4a**). These subunits are stabilised by the dipoles in a flux-closure state; the transformation from E to F involves a relatively high energy barrier due to the reorganisation of the dipoles within the final two subunits to attain the flux-closure state. Thus the main

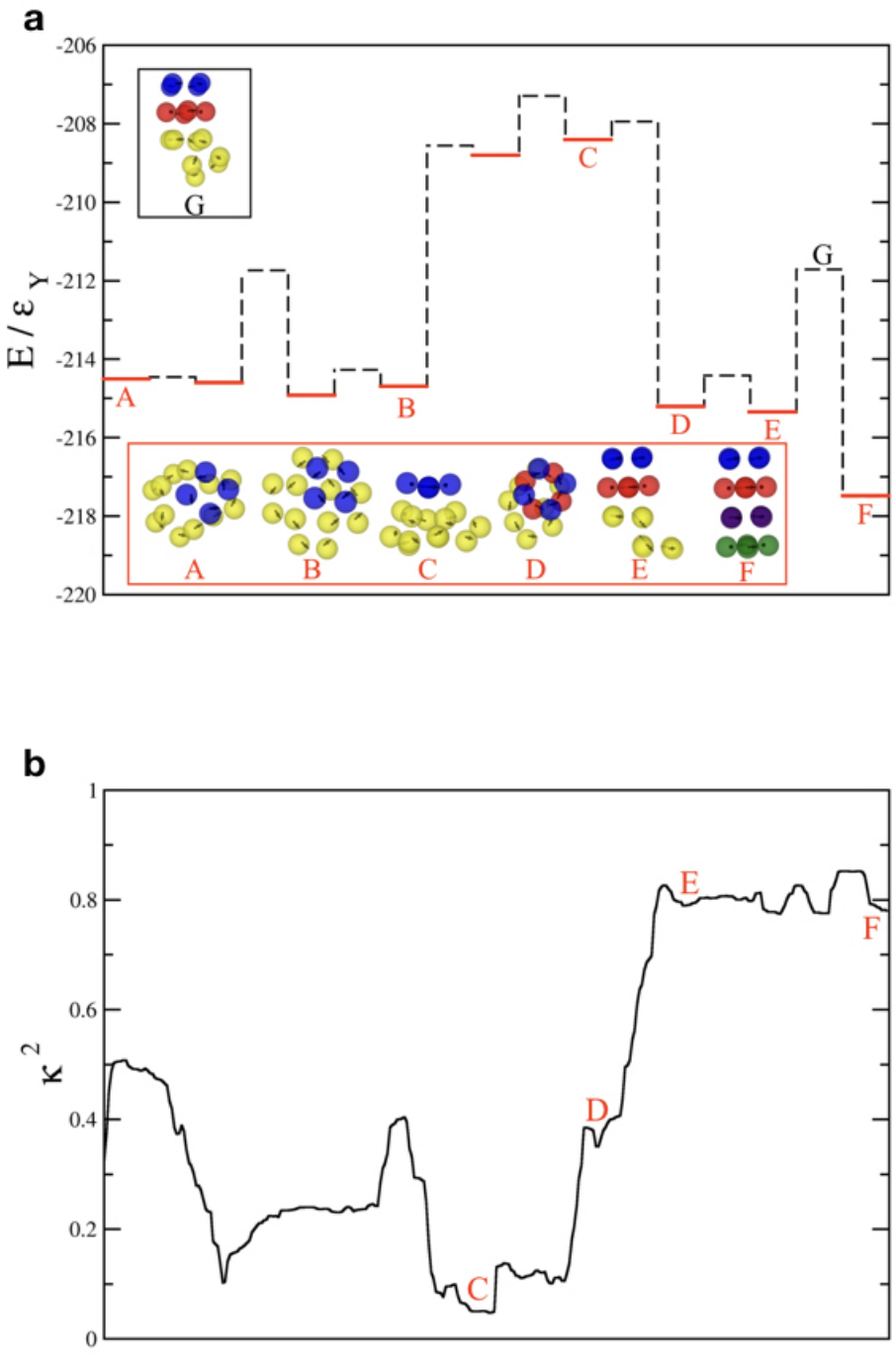

Figure 4.4: The dominant pathway for the self-assembly into a tubular structure formed by $N = 16$ designer charge-stabilised colloidal magnetic particles with $\theta = 90°$. The colloidal magnetic particles are shown not to scale. **a**. The potential energy profile for the pathway along with the structures corresponding to a few selected stationary points. The solid and dashed horizontal lines correspond to the minima and transition states, respectively. The secondary building blocks, the square planar subunits, when formed are colour-coded for visual aid. **b**. The evolution of the relative shape anisotropy parameter κ^2 along the pathway. For both **a** and **b**, the lateral displacement is arbitrary as the pathway is traversed.

feature for this pathway for hierarchical self-assembly is that the assembly at both the levels proceed simultaneously to eventually produce a two-level structural hierarchy. The relative shape anisotropy parameter κ^2 for a cluster, bounded between 0 and 1, provides an estimate of its shape anisotropy.[203] $\kappa^2 = 0$ for a spherically symmetric distribution and $\kappa^2 = 1$ for a perfectly linear arrangement. The evolution of κ^2 along the self-assembly pathway into the tubular structure, shown in **Figure 4.4b**, highlights the progressive increase in κ^2 with the quasi one-dimensional growth caused by the sequential attachment of the tetrameric subunits to the tubular motif as they are formed.

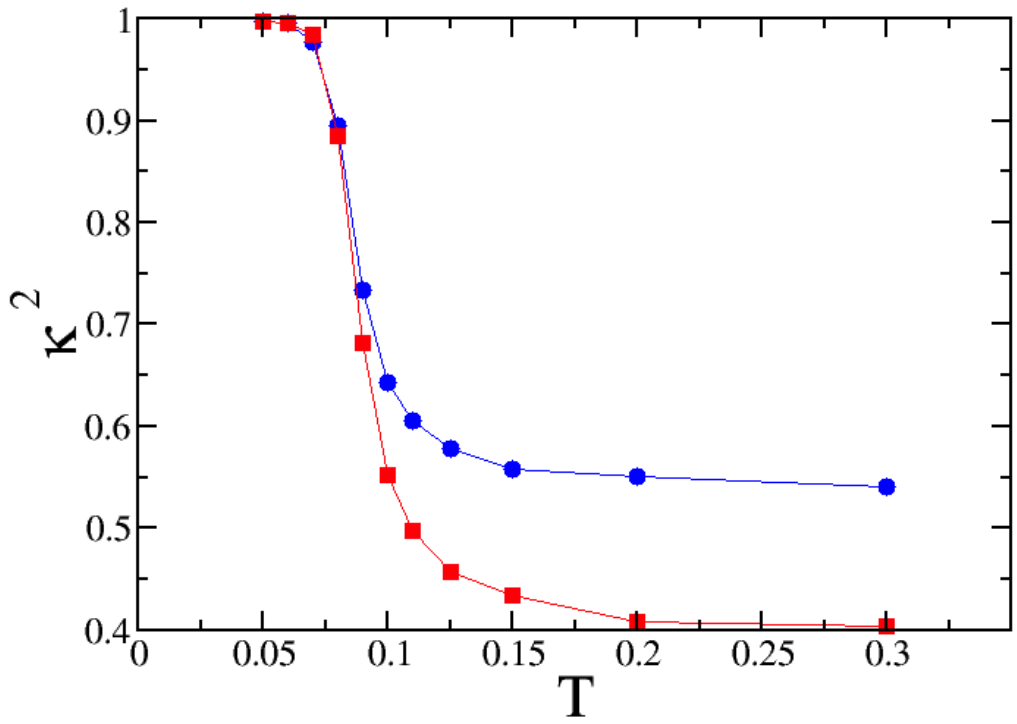

Figure 4.5: Relative shape anisotropy parameter as a function of reduced temperature for a cluster of 4 square planar units constrained within two spherical containers of radii: 3 (square) and 2 (circle) in reduced units. The average values over five independent runs are shown.

In order to assess whether the thermodynamically stable tubular structure is kinetically accessible and is thus likely to be self-assembled under appropriate experimental conditions, we carried out Monte Carlo simulations wherein the reduced temperature $T^\star$ was gradually reduced from a finite value. Since the pathway, shown **Figure 4.4a**, suggests that the hierarchical self-assembly into the tubular structure is most likely to proceed via the formation of the square planar units, Monte Carlo simulations were performed with the secondary building blocks, shown in **Figure 4.3b**, modeled as rigid units. Such an approach allowed single-particle moves

to be used effectively in a multi-scale problem. **Figure 4.5** shows the evolution of the parameter κ^2 as a function of the reduced temperature; the gradual growth of κ^2 to unity indicates the formation of increasingly quasi one-dimensional structure. Note that for a perfectly tubular structure, the centres of the rigid secondary building blocks are co-linear, for which $\kappa^2 = 1$.

4.3.2 *In Silico* Search for the Snub Tetrahedron

We next sought the design rule for the snub tetrahedron, the smallest member of the set of convex snub polyhedra. In our quest for the snub tetrahedron, we focused on the cluster of $N = 12$ cylindrically symmetric (i.e. $\theta = 0°$) colloidal magnetic particles, which show propensity to form trimers (see **Figure 4.6**) While the global minimum on the PEL is a bowl structure (**Figure 4.7a**), we identified a spheroidal structure that is topologically equivalent to the snub tetrahedron as a low-lying minimum (**Figure 4.7b**). Both of these structures exhibit a two-level structural hierarchy, where planar triangular subunits, stabilised by a flux-closure arrangement of the point-dipoles, serve as secondary building blocks (see **Figure 4.6**). It is the organisation of these secondary building blocks that results in an open or a closed structure. Analysis of the energetics for these structures reveals that a nearly anti-parallel arrangement of the dipoles in neighbouring secondary building blocks is energetically favoured (representative examples are shown in **Figure 4.6a**, **b** and also in **Figure 4.8**) and is a key factor in determining the low energy structures. Such interactions, though fewer in number for the bowl structure compared to the spheroidal structure, are of sufficient strength to make the bowl structure the global minimum on the PEL. The angle ϕ between the dipoles for such pairs is closer to the perfect anti-parallel arrangement in the bowl structure (see **Table** 4.2).

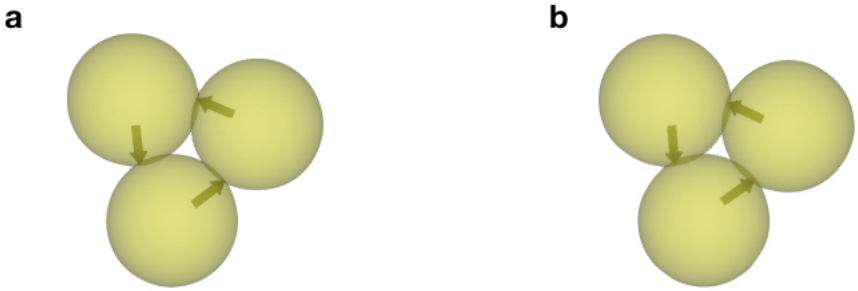

Figure 4.6: The triangular subunits formed as secondary building blocks in the hierarchical self-assembly route to hollow spheroidal structures. **a**. The triangular subunit for $\theta = 0°$; **b**. the triangular subunit for $\theta = 10°$.

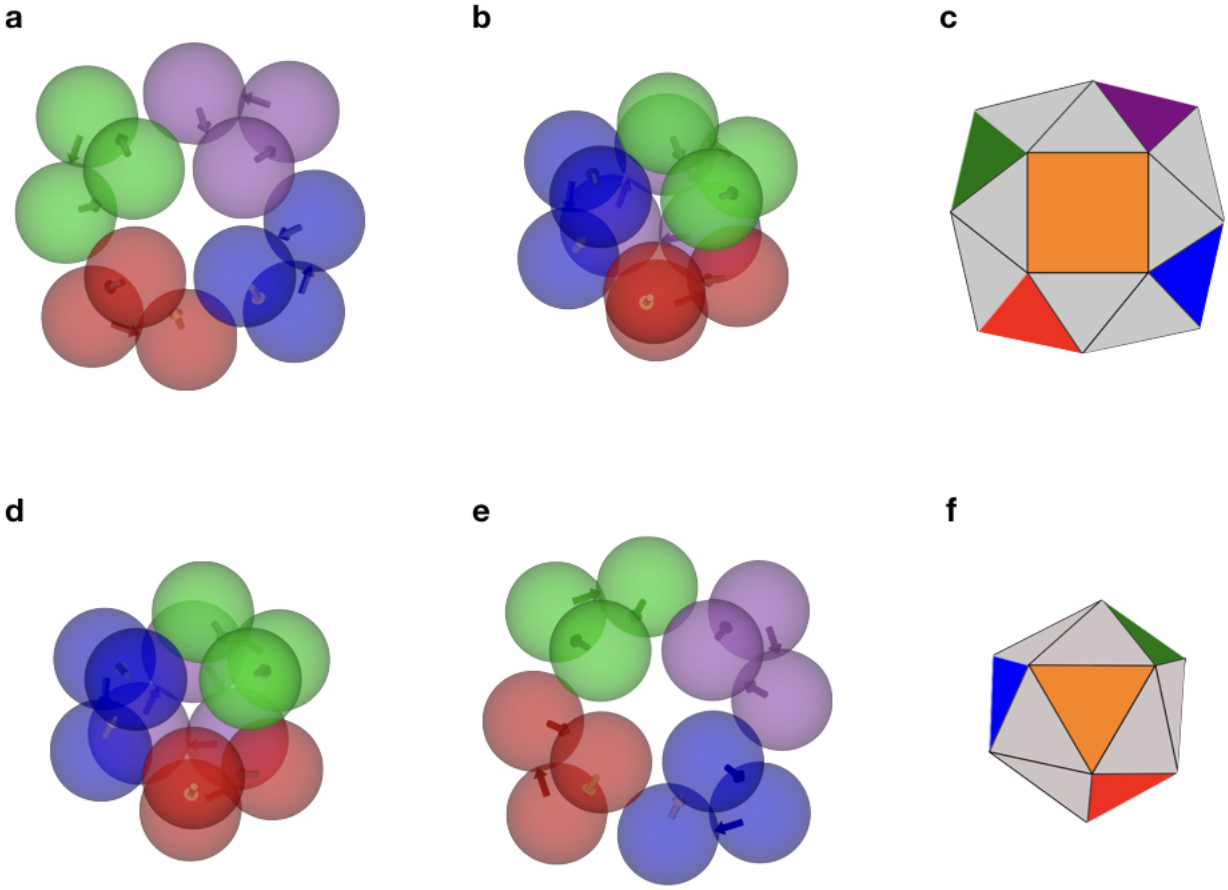

Figure 4.7: The competing structures, characterised as the low-lying minima on the energy landscape, for $N = 12$ charge-stabilised magnetic colloids with an embedded point-dipole shifted away from the centre. The angle θ defines the angle between the direction of the dipole and the radial shift. In this case $\alpha = 0.6$, $\mu_D = 2.0$ and $\lambda^{-1} = 25.0$; θ is varied. **a**. The bowl structure for $\theta = 0°$; **b**. the spheroidal structure for $\theta = 0°$; **c**.polyhedral representation of the bowl structure shown in **a**; **d**. the spheroidal structure for $\theta = 10°$, **e**. the bowl structure for $\theta = 10°$; **f**. polyhedral representation of the spheroidal structure shown in **d**. The secondary building blocks are highlighted by colour-coding and representative examples of anti-parallel arrangements of the dipoles in neighbouring secondary building blocks are shown in yellow. The spheroidal structure is topologically equivalent to the snub tetrahedron.

Minimum	ϕ	R_{ij}/σ	r_{ij}/σ	$E_{ap}/\epsilon_{\mathrm{Y}}$
The bowl structure	172.8	1.02	0.8	−7.66
The spheroidal structure	164.8	1.05	0.86	−6.04

Table 4.2: A comparison of the anti-parallel arrangements of the dipoles in two neighbouring secondary building blocks of two low-lying minima for $N = 12$ charge-stabilised colloidal magnetic particles, where $\theta = 0°$. ϕ is the angle between the dipole vectors, R_{ij} is the distance between the centres of the spherical colloidal particles, r_{ij} is the distance between the point-dipoles and E_{ap} is the potential energy contribution arising from the two dipoles.

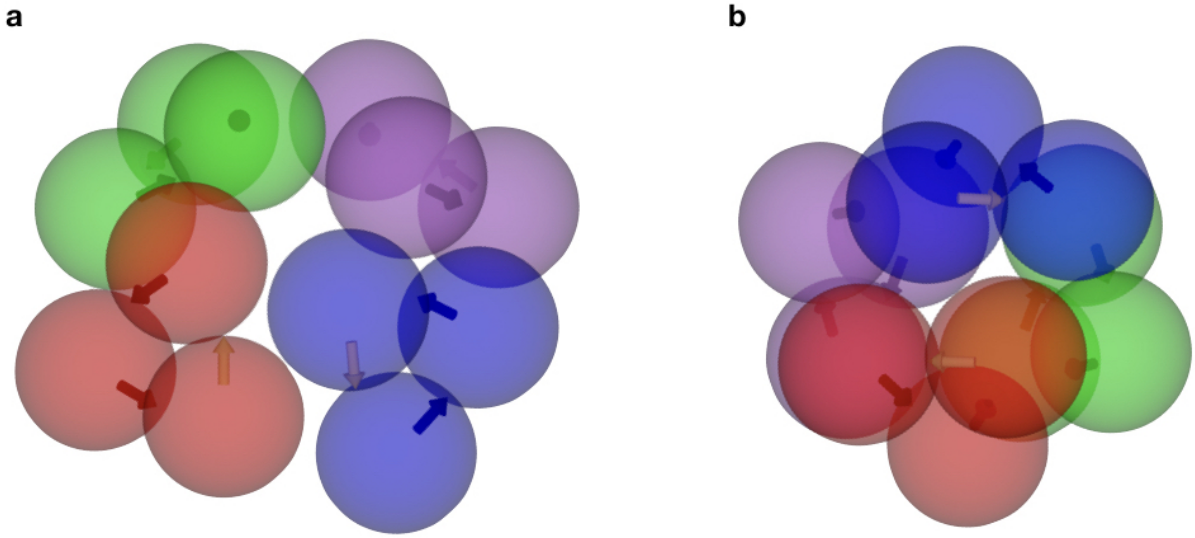

Figure 4.8: The competing structures, characterised as the low-lying minima on the energy landscape, for $N = 12$ charge-stabilised magnetic colloids. Representative examples of the anti-parallel arrangement of the dipoles in neighbouring secondary building blocks are clearly shown here and the dipoles concerned are highlighted in yellow. **a.** The ground state structure for $\theta = 0°$; **b.** the ground state structure for $\theta = 10°$. Here θ defines the angle between the direction of the dipole and the radial shift.

The above analysis led us to vary the parameter θ for our designer building blocks and investigate the structures and energetics. This choice also appeals in the context of the uncertainty in the direction of the dipole moment within the magnetic cube used in the synthesis of colloidal magnetic particles.[176] For $\theta = 10°$, the propensity for hierarchical self-assembly was retained with the triangular subunits in the flux-closure arrangement formed at the first level of organisation. In fact, the triangular subunit is more stable when $\theta = 10°$ as compared to $\theta = 0°$ due to a decrease in the separation between the dipoles within the subunit. For $N = 12$, we indeed find the global minimum to be a spheroidal structure (**Figure 4.7d**) that

Minimum	ϕ	R_{ij}/σ	r_{ij}/σ	$E_{ap}/\epsilon_{\mathrm{Y}}$
The bowl structure	174.7	1.05	0.92	−5.11
The spheroidal structure	166.3	1.07	0.94	−4.74

Table 4.3: A comparison of the anti-parallel arrangements of the dipoles in two neighbouring secondary building blocks of two low-lying minima for $N = 12$ charge-stabilised colloidal magnetic particles, where $\theta = 10^{\circ}$. ϕ is the angle between the dipole vectors, R_{ij} is the distance between the centres of the spherical colloidal particles, r_{ij} is the distance between the point-dipoles and E_{ap} is the potential energy contribution arising from the two dipoles.

is topologically equivalent to the snub tetrahedron as evident in **Figure 4.7f**. Note that it is chiral with tetrahedral symmetry. In this case, the interactions between the dipoles in the anti-parallel arrangements in neighbouring secondary building blocks are sufficient in strength in the spheroidal structure, though they are still weaker than those in the bowl structure (**Figure 4.7e**), to stabilise the spheroidal structure, and in fact, cause it to be the global minimum on the PEL. The details of the energetics along with the geometric features are given in **Table** 4.3 for the $\theta = 10^{\circ}$ case.

It was then relevant to investigate whether the designer colloidal magnetic particles with $\theta = 10^{\circ}$ formed the other two convex snub polyhedra for appropriate size selected clusters. To this end, we considered $N = 24$ and $N = 60$. In the case of $N = 24$, the ground state structure for the cluster is indeed a convex polyhedron of octahedral (O) symmetry, displaying two-level structural hierarchy, as shown in **Figure 4.9**. This polyhedron is composed of 32 triangular faces and 6 square faces and is topologically equivalent to the snub cube, a chiral Archimedean solid. Eight of the triangular faces (shown in distinct colours) originate from the colloidal particles forming triangular subunits of three-fold rotational symmetry. The other triangular faces (shown in light gray) and the square faces (shown in orange) emerge from the hierarchical self-assembly of these triangular subunits. The emergent triangular faces have slightly different edge lengths, making the polyhedron topologically equivalent to the snub cube. In the case of $N = 60$, however, we have not observed such a spheroidal structure to be the ground state. A polyhedron topologically equivalent to the snub dodecahedron and thus of icosahedral symmetry would have an emergent face of five-fold symmetry. For our designer colloidal magnetic particles with $\theta = 10^{\circ}$, we have found that for $N = 15$ a bowl structure with such an emergent face is not the global minimum. Instead, the global minimum in this case

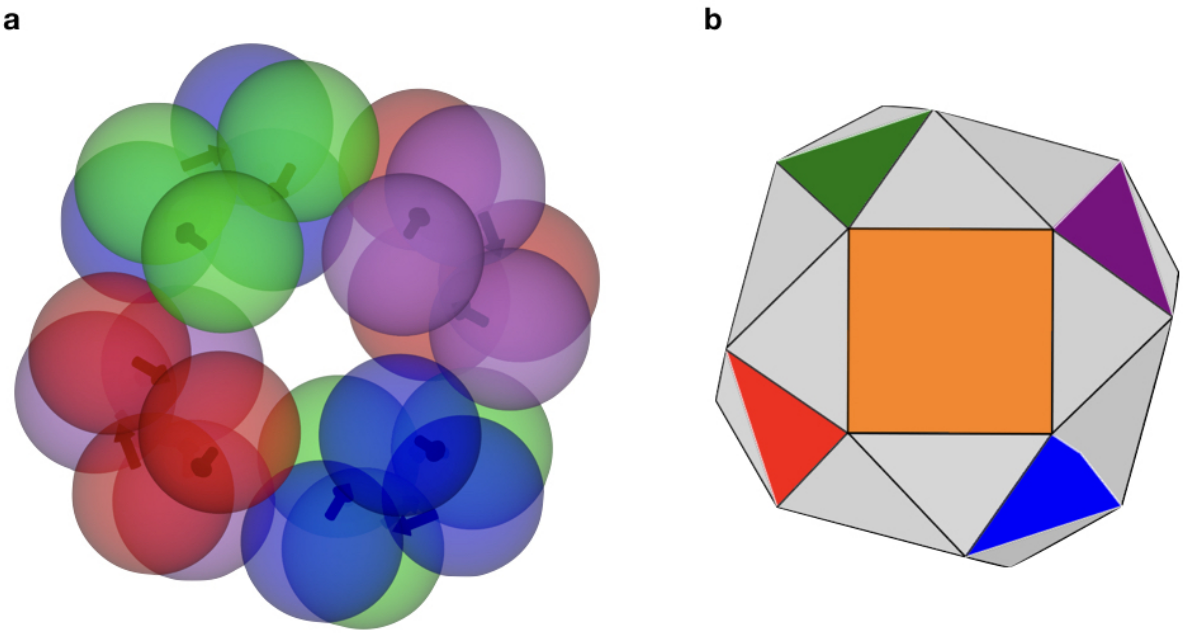

Figure 4.9: The structure of octahedral (O) symmetry, topologically equivalent to the snub cube, characterised as the global minimum for a cluster of $N = 24$ charge-stabilised colloidal magnetic particles with $\theta = 10°$. Two representations of the same structure are shown: **a.** spheroidal particles with embedded dipoles, drawn not to scale; **b.** the convex polyhedron with the faces colour-coded to distinguish between them. Eight of the triangular faces of three-fold symmetry, colour-coded distinctly, are formed by the colloidal magnetic particles at the first level of organisation; the emergent faces from the second-level of organisation are shown in orange (square faces) and in light gray (triangular faces).

corresponds to a configuration, containing a polyhedron that is topologically equivalent to the snub tetrahedron plus an additional trimeric subunit (**Figure 4.10**). This is in line with our observation for $N = 60$.

Finally, we characterised the dominant pathway to the hollow spheroidal structure of tetrahedral symmetry, topologically equivalent to the snub tetrahedron, as shown in **Figure 4.7d**. It was of interest to compare pathways to two distinct polyhedra that both exhibit two-level structural hierarchies with different types of subunits formed at the intermediate level.[66] **Figure 4.11** shows the energy profile of the dominant pathway that we have obtained for the self-assembly to the spheroidal structure, which is the smallest in this series, starting from a relatively high-energy, disordered minimum. (electronic supplimentary information of Ref.[68]) This self-assembly pathway suggests that the pathway is hierarchical, where the two-level organisation proceeds stage-wise. In the first stage, trimers stabilised by the arrangement of dipoles in a flux-closure state are formed. These trimers act as the secondary building blocks

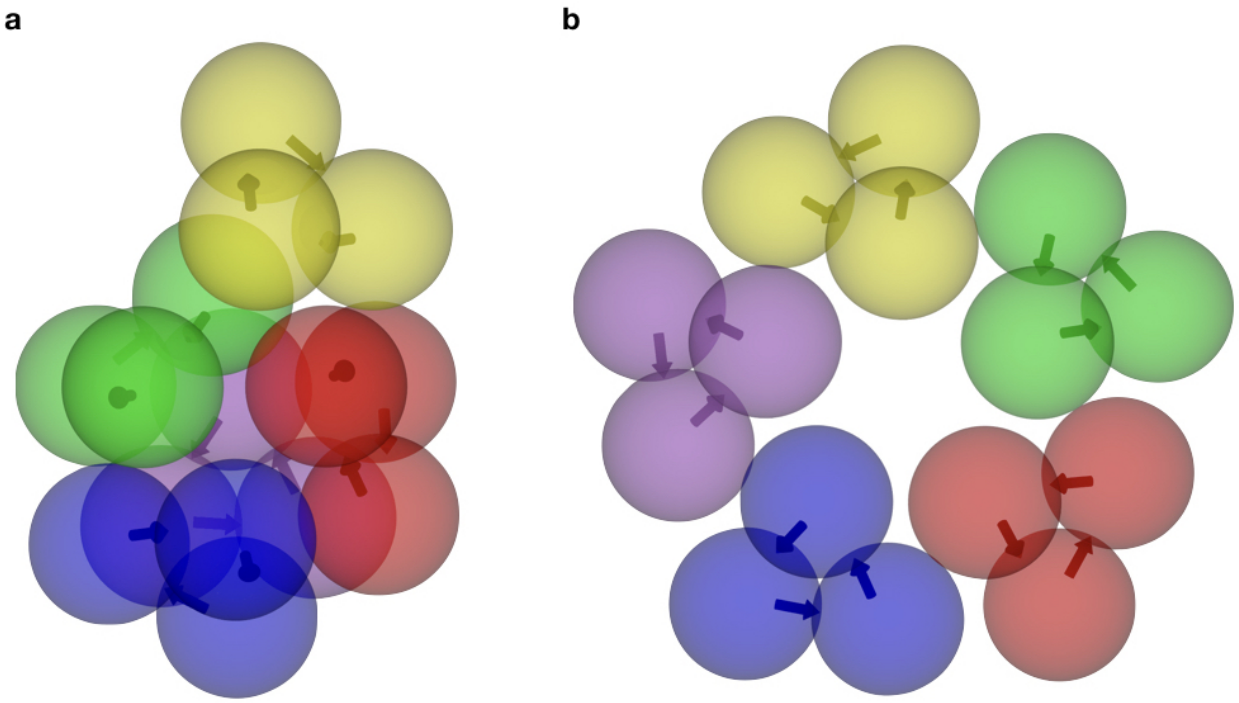

Figure 4.10: The two structures characterised as the low lying minima on the energy landscape for $N = 15$ charge-stabilised colloidal magnetic particles, where $\theta = 10°$. **a.** The ground state structure, which consisted of the snub tetrahedron plus an additional triangular subunit; **b.** the bowl structure, a low lying minimum, with an emergent five-fold rotational symmetry.

for the subsequent stage and the next level of assembly is driven by the stability arising from the anti-parallel arrangements of the dipoles between the secondary building blocks. Through the second stage of assembly the trimers retain their integrity, invoking a high degree of cooperativity. The energy barriers involved in the second stage of assembly are therefore relatively low. However, the element of cooperativity is likely to result in relatively high entropy costs in the free-energy barriers.

When subjected to an external magnetic field, the tubular structures collapse above a threshold field. For example, the ground state structure for the $N = 16$ cluster with $\theta = 90°$ was found to be a zig-zag chain, where the dipoles are parallel to the field direction, as shown in **Figure 4.12**. For a nonzero value of θ, such a zig-zag configuration is favoured over a linear configuration by the dipolar interactions due to a smaller separation between the adjacent point-dipoles in the former case. The structures can thus be reconfigured by the application of an external magnetic field above a threshold. The ability to reconfigure an enclosed structure is especially attractive when it is hollow and spheroidal for the design of responsive containers that can encapsulate guests and release them on demand.

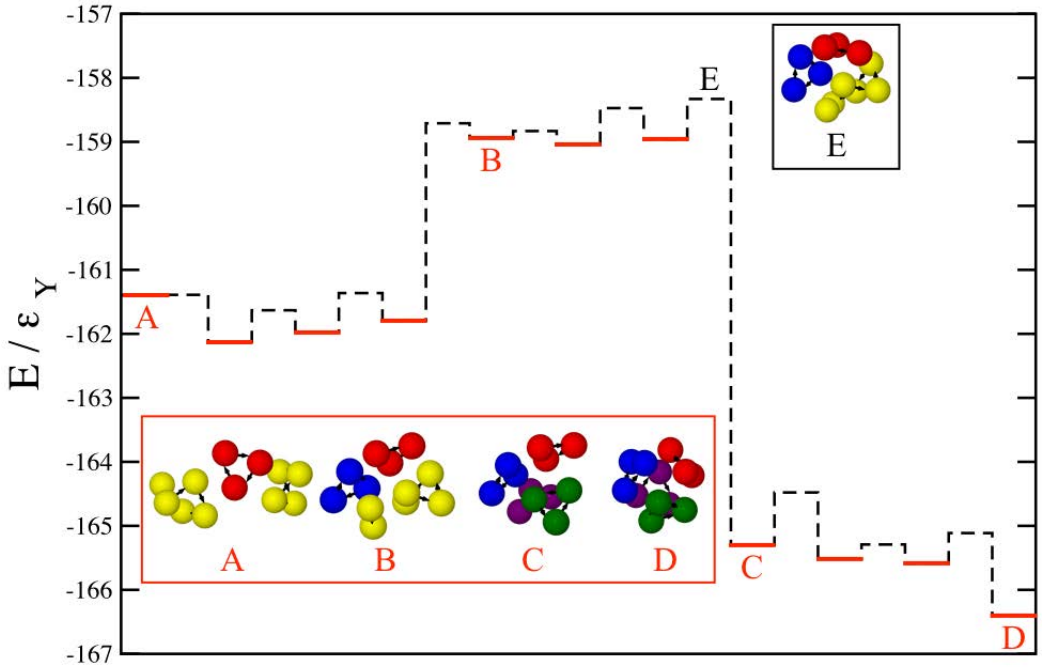

Figure 4.11: The potential energy profile along a dominant pathway for the self-assembly into a spheroidal structure, topologically equivalent to the snub tetrahedron, formed by $N = 12$ designer charge-stabilised colloidal magnetic particles with $\theta = 10°$. The solid and dashed horizontal lines correspond to the minima and transition states, respectively. The inset images show structures corresponding to selected stationary points labeled along the pathway. The secondary building blocks, the triangular subunits, when formed are colour-coded for visual aid.

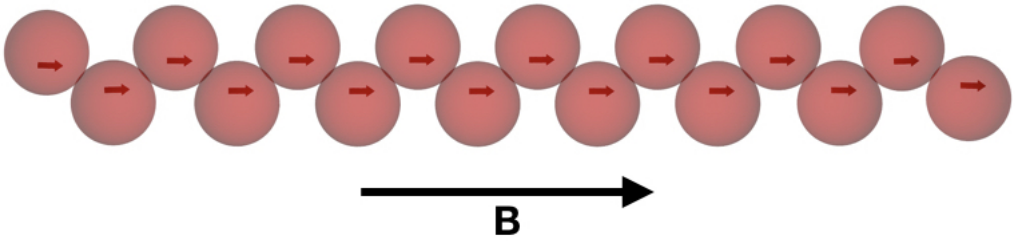

Figure 4.12: The ground state structure for $N = 16$ charge-stabilised colloidal magnetic particles, each with an embedded shifted dipole at an angle $\theta = 90°$ to the radial shift, in the presence of an applied magnetic field $B = 10.0$.

The colloidal magnetic particles we have considered in the present study are in close correspondence with the colloidal magnetic particles, synthesised using iron oxide inclusions located underneath the surface of organosilica polymer spheres.[176] Reasonable estimates for the parameters can be obtained in real units by using $\epsilon_{\mathrm{Y}} = 4.1 \times 10^{-21}$ J (of the order of $k_{\mathrm{B}}T$ at room temperature) and $\sigma = 10^{-6}$ m. Corresponding to these values, we have in real units $\mu_D \approx 4 \times 10^{-16}$ A m^2, $B \approx 2 \times 10^{-4}$ T, and $\lambda = 40$ nm, all well within the experimentally

accessible regime.[176] The control of the colloidal charge number allows for the value of the Yukawa contact potential ϵ_{Y} to be modulated by an order of magnitude.[184]

4.4 Conclusions

The present computer simulation study has identified a series of polyhedra as the ground state structures for size-selected clusters of designer charge-stabilised colloidal magnetic particles, each with an embedded point-dipole at an off-centred location. In particular, we have identified square anti-prismatic tubular structures and spheroidal polyhedra as the ground state structures for the design space that we investigated. A remarkable feature of these supracolloidal polyhedra of distinct morphologies is that they all exhibit two-level structural hierarchies, via either tetramers or trimers in the intermediate level. The subunits formed at the intermediate level have the dipoles in flux-closure arrangements in either case. The shift of the dipole relative to the centre, described by the parameter α, and the angle θ between the dipole vector and the radial shift vector are the two critical parameters that determine whether these subunits have four-fold or three-fold rotational symmetry and hence the overall morphology. We have thus been able to design structural hierarchies via tetramers in a controlled way.

In our quest for the snub tetrahedron, we have found the angle θ to be a critical parameter to determine the stability of a topological variant of the snub tetrahedron relative to the bowl structure on the PEL. In particular, for $\theta = 10^{\circ}$, we observed the ground state structures, which are topologically equivalent to the snub tetrahedron ($N = 12$) and the snub cube ($N = 24$), two of the three convex snub polyhedra that exist. The third member of this set is the snub dodecahedron, which is of icosahedral symmetry; for $N = 60$, we observed the ground state structure that is topologically equivalent to the snub dodecahedron in the case of $\theta = 0^{\circ}$, but not for $\theta = 10^{\circ}$. On the other hand, for $\theta = 0^{\circ}$, a snub polyhedral structure (topologically equivalent) is also the ground state structure for $N = 24$, but not for $N = 12$. It is important to note here that the internal angle for the emergent regular faces in this series of topologically equivalent snub polyhedra varies from 60° to 108° from the snub tetrahedron to the snub dodecahedron. It is plausible that this angular range is too wide for these emergent faces be supported by our designer colloidal magnetic particles for a single value of θ for these polyhedra to be the ground state structures for appropriate size-selected clusters. Another striking feature

is that the spheroidal polyhedra, which are formed via the formation of triangular subunits at the intermediate level, are chiral, despite having a high degree of rotational symmetry.

It is intriguing that the dominant kinetic pathways, which we characterised for the self-assembly into two distinct supracolloidal polyhedra, present very different mechanisms for emergent two-level structural hierarchies, presumably due to the distinct morphologies of these polyhedra. These pathways provide especially distinct routes depending upon whether organisation at different levels proceeds simultaneously or sequentially. In the former case, higher-order building blocks are formed one by one and attach to a growing structural motif corresponding to the next level of organisation; in the latter, higher-order building blocks are all formed before the next level of organisation proceeds.[218] The spheroidal structures can be underpinned by only certain numbers of triangular subunits commensurate with closed shells. In contrast, the square planar subunits, which serve as the secondary building blocks, can directly stack up to form the tubular structures. It is likely that these structural features of the assemblages resulted in the distinct mechanisms that we observed. The formation of the spheroidal structure proceeds via a hierarchical pathway where the requisite number of triangular subunits are produced in the first stage before the organisation of these secondary building blocks takes place. The tubular structure is instead formed via a growth mechanism involving sequential attachment of the secondary building blocks as they are formed. It is noteworthy that cooperative particle dynamics are crucial for the hierarchical pathway, and the corresponding free-energy barrier is likely to have a considerable entropy contribution. The mechanistic understanding of the self-assembly pathways will be critical to our ability to effectively control the dynamical pathways.[231,232]

These supracolloidal polyhedra can serve as microscale containers, the practical applications of which primarily arise from their ability to encapsulate guests. Our results demonstrate a feasible design space for the experimental realisation of such 3-dimensional hollow structures, exploiting a hierarchical self-assembly scheme. Additionally, we provide possible guidelines for controlling the morphology in terms of the two parameters α and θ, in particular. The responsiveness of these containers to an applied magnetic field is a particularly attractive feature that allows these containers to be opened and closed on demand. The spheroidal polyhedra that we characterised offer confined space enclosed by well-defined facets in a chiral environ-

ment, extending the features of metal–organic frameworks to the microscale,[162,233] and are thus likely to offer a further range of potential applications in catalysis and separation.[234] For these applications, the ability to select the size of the cluster will be especially crucial.

Chapter 5

Programming Hierarchical Self-assembly of Colloids: Matching Stability and Accessibility

5.1 Introduction

Hierarchical self-assembly of nano- and micro-particles is emerging as an attractive route to structural organisation at a higher level, spanning multiple length scales.[209,235] Notably, the hierarchical self-assembly of mono-disperse colloidal octapod-shaped nanocrystals resulted in a three-dimensional superlattice via the formation of linear chains of interlocked octapods.[98] The assembly of binary and ternary patchy nanoparticles produced supracolloidal ordered structures in a hierarchical scheme.[236] The 'patchiness' of colloidal triblock spherical particles was exploited to encode staged self-assembly triggered by stepwise changes of the ionic strength of the medium.[237] A computational study demonstrated an alternative scheme for patchiness without engineered surfaces en route to a variety of complex superstructures via hierarchical self-assembly.[238] Recent work also demonstrated how the self-assembly of colloidal particles in confinement could lead to a complex hierarchical geometry that exhibited a rich variety of optical effects including structural colouration due to the interaction of light with the structural features at different length scales.[239] We followed a biomimetic design route to hollow spheroidal structures, **Chapter 3 and 4** exploiting a hierarchical self-assembly scheme for charge-stabilised colloidal magnetic particles with an off-centred magnetic dipole.[66,68] While a

growing body of work in recent years has demonstrated the great promise of hierarchical colloidal self-assembly, a conceptual framework to reliably program hierarchical self-assembly of colloidal building blocks is still lacking. Such a framework is crucially important to address the challenge of a multiscale design problem, arising from the requirement of bridging hierarchies of multiple length- and time-scales, associated with structure and dynamics respectively, along the self-assembly pathway.

Harnessing the enormous potential for colloidal self-assembly to offer a bottom-up route to structure fabrication critically hinges on our ability to manipulate the interactions between the colloidal particles such that a target structure is not only thermodynamically favourable, but also kinetically accessible on experimental time scales.[22,240] This task becomes even more formidable in the context of hierarchical self-assembly. In this case, a pertinent question is whether the pathway is staged – that is to say, whether the assembly itself follows a hierarchical pathway.[68,218] Such a pathway for colloidal self-assembly would involve concerted movements of colloidal particles over the course of the assembly pathway. In fact, the requirement of matching stability and accessibility draws a parallel between the target structure for programmed self-assembly and the native structure of a protein.[241]

In particular, hollow spheroidal structures at the nano- and micro-scale are attractive targets for a range of practical applications,[67,163,242] especially as nanocapsules resembling viral capsids and microvesicles for drug delivery.[62,243] Viral capsids of icosahedral symmetry are in fact marvelous examples of molecular self-assembly in nature, resulting in a remarkable structural hierarchy in terms of repeating subunits.[69] While the structures of viral capsids are now known in great detail, the pathways for capsid assembly remain poorly understood largely due to limitations on experimental characterisation.[244,245]

In this chapter, we employ a variety of computational methods to examine the kinetic accessibility of the hollow spheroidal structures self-assembled from charge-stabilised colloidal magnetic particles. The structures each show a fascinating two-level structural hierarchy. We demonstrate how an optimal design rule for hierarchical self-assembly in this case can be derived while satisfying both the thermodynamic and kinetic criteria. We find a striking correspondence between the thermodynamics and kinetics, which we account for in a staged assembly pathway. While our designer building blocks closely resemble recently synthesised colloidal magnetic

particles,[176] our results suggest design principles, which should have general implications for programming hierarchical self-assembly of nano- and micro-particles.

5.2 Methods

5.2.1 The Model

We model the charge-stabilised colloidal magnetic particles under consideration using a one-component description with an effective pairwise potential and the point-dipole approximation for the magnetic interactions. The point-dipole was off-centred, located at a distance d away from the centre of a spherical particles and inclined with an angle θ to the radial shift vector. The Yukawa potential was used to describe the screened electrostatic repulsion giving rise to the charge-stabilisation. In this description, the potential energy V for a finite-size system of N colloidal magnetic particles in the absence of any external magnetic field is then given by

$$V = \sum_{i=1}^{N-1} \sum_{j=i+1}^{N} \epsilon_{\mathrm{Y}} \frac{\exp[-\lambda^{-1}(R_{ij} - \sigma)]}{R_{ij}/\sigma} + \sum_{i=1}^{N-1} \sum_{j=i+1}^{N} \frac{\mu_0}{4\pi} \frac{\mu_D^2}{r_{ij}^3} [(\hat{\boldsymbol{\mu}}_i \cdot \hat{\boldsymbol{\mu}}_j) - 3(\hat{\boldsymbol{\mu}}_i \cdot \hat{\boldsymbol{r}}_{ij})(\hat{\boldsymbol{\mu}}_j \cdot \hat{\boldsymbol{r}}_{ij})] \tag{5.1}$$

Here, $\boldsymbol{R}_i$ and $\boldsymbol{r}_i$ are the position vectors for the centre of colloidal particle i and its embedded point dipole, respectively, $\hat{\boldsymbol{\mu}}_i$ is the unit vector defining the orientation of the aforementioned point dipole, whose magnitude is given by μ_D, μ_0 is the permeability of free space, and $\boldsymbol{r}_{ij}$ is the separation vector: $\boldsymbol{r}_{ij} = \boldsymbol{r}_i - \boldsymbol{r}_j$ with magnitude r_{ij} , so that the unit vector $\hat{\boldsymbol{r}}_{ij} = \boldsymbol{r}_{ij}/r_{ij}$. In the Yukawa description of screened electrostatic repulsion, λ^{-1} is the inverse Debye screening length and ϵ_{Y} is the so-called contact potential. The chosen units of energy and length are the Yukawa parameters ϵ_{Y} and σ, respectively. The model parameters are then the inverse Debye screening length λ^{-1}, the strength of the magnetic dipole μ_D, the separation d between the centre of the colloidal particle and the location of the embedded point dipole and the angle θ between the direction of the dipole moment $\hat{\boldsymbol{\mu}}_i$ and the shift vector $\boldsymbol{r}_i - \boldsymbol{R}_i$. The shift distance is expressed in terms of the dimensionless ratio $\alpha = 2d/\sigma$, where σ is the length scale in terms of which the Yukawa potential is defined, proposing an estimate of the particle size in the absence

of a hard core. The magnetic dipole μ_D is given in reduced units of $(4\pi\epsilon_Y\sigma^3/\mu_0)^{1/2}$. In the present study, $\alpha = 0.6$, $\mu_D = 2.0$ and $\lambda^{-1} = 25.0$; θ was varied. We treated the colloidal particles as rigid bodies, representing the translational coordinates of each rigid body by the Cartesian coordinates of the centre of the spherical particle and the rotational coordinates by a unit quaternion, unless specified otherwise. An additional contribution to the potential energy is drawn in the presence of an external static magnetic field $\boldsymbol{B}$ and is given by $-\mu_D \sum_{i=1}^{N} \hat{\boldsymbol{\mu}}_i \cdot \boldsymbol{B}$. The magnetic field strength B is given here in the units of $[\epsilon_Y\mu_0/(4\pi\sigma^3]^{1/2}$.

5.2.2 Simulation Details

Global Optimisation

We used the basin-hopping (BH) global optimisation method[24,132] to identify the global minimum of potential energy landscape and to calculate mean first encounter times. An angle-axis representation was used for the rigid-body rotational coordinates due to certain numerical advantages associated with such a representation in the context of geometry optimisation.[123] For each set of model parameters with a distinct value of θ, twenty independent BH global optimisation runs were performed, undertaking 5×10^6 basin-hopping steps from an identical set of random initial configurations. The BH step at which the global minimum was first identified for each run, the first-encounter time, was recorded to calculate a mean first-encounter time for each θ.

Monte Carlo Sampling

Monte Carlo (MC) simulations of a number of systems, each containing $N_t = 8$ rigid building blocks, were performed in the canonical ensemble, employing a constraining radius to avoid evaporation especially at high temperatures. In the present study, the radius of the container used was 2.5 in the reduced unit. For each set of model parameters with a distinct value of θ, 10 independent MC runs were undertaken. In a given run, starting from a random initial configuration, the system was gradually cooled. The number of MC steps carried out increased from 10^7 at high temperatures to 2×10^9 at low temperatures; the first half of the MC run at every temperature was used for the system to equilibrate. Each MC step involved N_t single-particle moves in both translational and rotational coordinates, where the step sizes

were adapted to achieve a target acceptance ratio of 0.45. For the MC simulations, the reduced temperature $T^\star$, given by $T^\star = k_\mathrm{B}T/\epsilon_\mathrm{Y}$, was used.

The formation of the spheroidal structure was monitored by calculating the relative shape anisotropy,[203] κ^2, for the distribution of the particles in the system which is given by

$$\kappa^2 = \frac{b^2 + (3/4)c^2}{R_g^4}, \tag{5.2}$$

where R_g is the radius of gyration, b the asphericity, and c the acylindricity: $R_g^2 = \lambda_x^2 + \lambda_y^2 + \lambda_z^2$, $b = (3/2)\lambda_z^2 - (1/2)R_g^2$ and $c = \lambda_y^2 - \lambda_x^2$; $\lambda_x^2 \geq \lambda_y^2 \geq \lambda_z^2$ are the principal moments of the gyration tensor $\mathbf{S}$.

In order to compute the free energy profiles, we employed umbrella sampling,[246] using the relative shape anisotropy κ^2 as the order parameter. To this end, a series of Monte Carlo simulations of 8 rigid trimers were carried out employing additional biasing potentials, which were harmonic functions, centred on successive values of the order parameter. The biasing potentials ensured efficient sampling over several partially overlapping windows, spanning the range of the order parameter of interest. The unbiased probability distribution was then obtained using the weighted histogram analysis method.[247,248] Finally, the free energy difference along the chosen order parameter was evaluated from this unbiased probability distribution, taking the hollow spheroidal structure, corresponding to $\kappa^2 \approx 0$, as the reference.

Virtual Move Monte Carlo

We employed the virtual move Monte Carlo (VMMC) algorithm,[142] following a recent prescription.[144] The VMMC algorithm prescribes cluster moves. It is necessary to consider cluster moves in the context of emergent structural hierarchy. Such an algorithm helps to overcome the non-physical kinetic traps that are encountered during MC simulations employing single-particle moves, leading to an enhanced sampling of the equilibrium distribution.

We carried out VMMC simulations in the canonical ensemble for finite-size clusters of $N = 24$ particles contained within a spherical volume of radius 2.5 in the reduced unit. For each set of model parameters with a distinct value for θ, 10 independent VMMC simulations were performed starting from random initial configurations. For a given run, the system was

gradually cooled. As the reduced temperature $T^\star$ was decreased, the number of VMMC cycles undertaken was increased from 10^8 at high temperatures to 10^9 at low temperatures. Each VMMC cycle involved N translational moves or N collective rotational moves; the first half of the run at every temperature studied was used for equilibration. The steps sizes proposed within the translational and collective rotational VMMC moves were adjusted to secure an average acceptance ratio of 0.45. For the VMMC simulations, the reduced temperature $T^\star$ was also given by $T^\star = k_\mathrm{B}T/\epsilon_\mathrm{Y}$.

5.3 Results

While magnetic colloidal particles are classic examples of microscale building blocks with anisotropic interactions,[190] recent years have experienced a surge in the synthesis of exotic colloidal magnetic particles.[176,188] Having drawn motivation from these research activities, a number of computational studies have focused on spherical magnetic colloids with an additional anisotropy attribute in terms of an off-centred point-dipole.[66,214,215] We considered charge-stabilised colloidal magnetic particles, which included a permanent point-dipole shifted away from the centre,[66] closely resembling those synthesised using a single-domain hematite cube inclusion underneath the surface of organopolymer spheres.[176] However, there was uncertainty in the direction of the dipole moment within the magnetic cube in this experimental system.[214] It was most likely that the direction of the dipole was not parallel to the radial shift vector to the position of the dipole.[214] We introduced an additional model parameter θ, denoting the angle at which the direction of the point-dipole is inclined to the radial shift vector.[68]

We employed the basin-hopping global optimisation method to identify the global minima on the potential energy landscapes for size-selected clusters.[24,132] In the case of a cluster of $N = 24$ particles, a polyhedron of octahedral symmetry topologically equivalent to the snub cube was found to be the most favoured structure on the potential energy landscape for a range of θ values from 0° to 10° (see **Figure 5.1a**), the rest of the model parameters remaining identical. The supracolloidal polyhedron exhibited a fascinating two-level structural hierarchy via the formation of planar trimers with the dipoles in a flux-closure arrangement at the intermediate level (see **Figure 5.1d**). **Figure 5.1c** shows a polyhedral representation with colour codes to

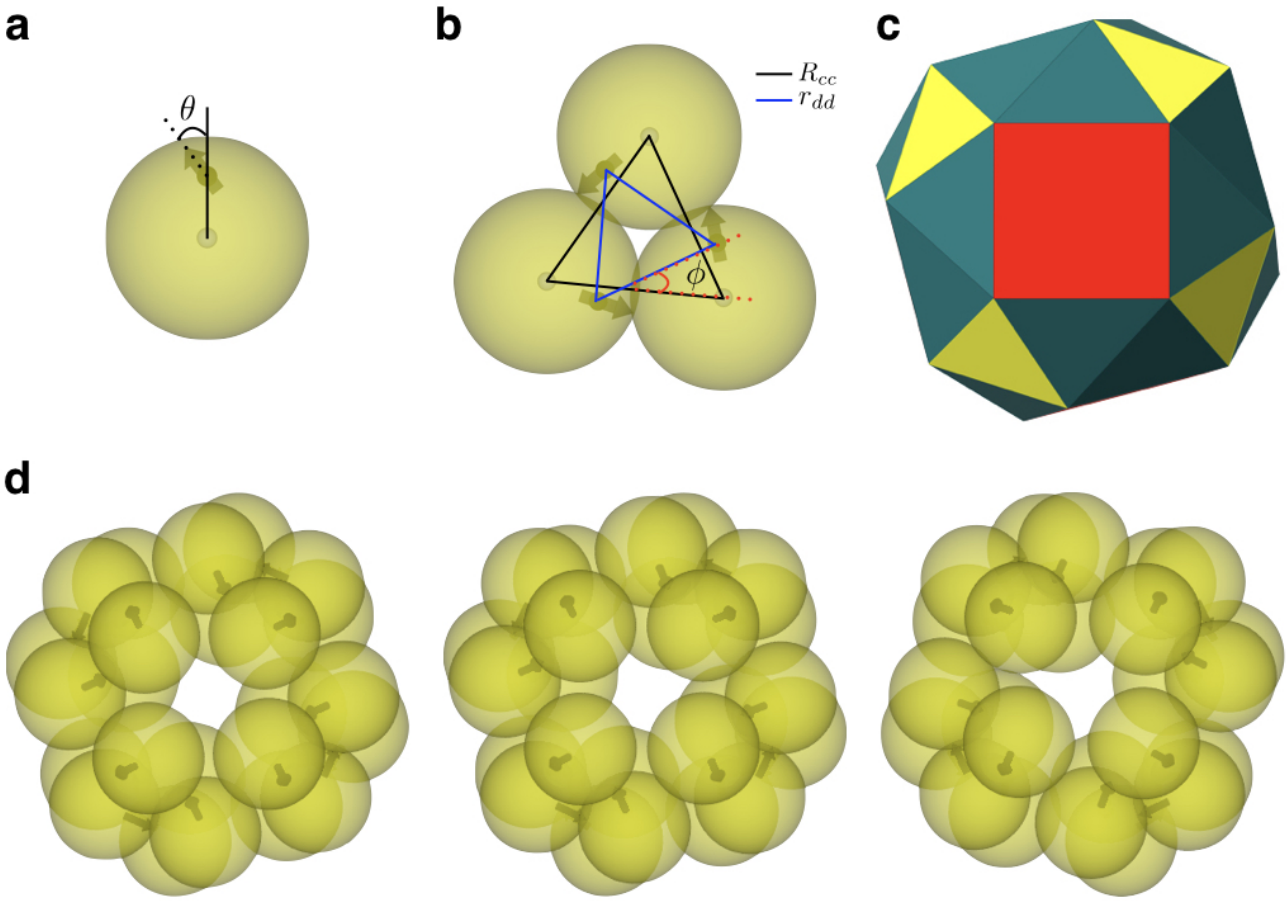

Figure 5.1: Two-level structural hierarchy emerging from the charge-stabilised colloidal magnetic particles under consideration. **a.** A schematic representation of a single colloidal magnetic particle, showing the angle θ at which the direction of the point-dipole is inclined to the radial shift vector. **b.** A representative global minimum for $N = 3$ charge-stabilised colloidal magnetic particles - the planar trimer formed at the intermediate level - showing the dipoles in a flux-closure arrangement. In addition, the parameters defining the structural features tabulated in Table 5.1 are shown: R_{cc} denotes the distance between the geometric centres of adjacent colloidal particles and r_{dd} the distance between the corresponding point-dipoles; ϕ is the angular displacement between the triangles formed by the geometric centres and those by the point-dipoles on the plane. **c.** A polyhedral representation of the snub cube structure of octahedral symmetry for $\theta = 5°$, where distinct types of faces are colour coded. The eight equilateral triangular faces, shown in yellow, are sustained by the colloidal magnetic particles; the remaining faces, namely six square faces (red) and twenty four triangular faces (blue), emerge from the assembly of these trimers. **d.** The global minimum for $N = 24$ charge stabilised colloidal magnetic particles corresponding to three sets of model parameters, where only the model parameter θ is varied. From the left to the right θ increases: 0°, 5° and 10°, respectively. All three structures are of octahedral symmetry and are topologically equivalent to the snub cube.

distinguish distinct types of faces. The eight equilateral triangular faces, shown in yellow in **Figure 5.1c**, are sustained by the colloidal magnetic particles; the remaining faces, namely six square faces (red) and twenty four triangular faces (blue) emerge from the assembly of

these trimers. Hereafter, we refer to this structure as the snub cube structure or the hollow spheroidal structure. For $\theta = 15°$, the snub cube structure was no longer the global minimum on the energy landscape. In the present study, we compared the kinetic accessibility of the snub cube structure for three different θ values over the range of θ values from $0°$ to $10°$, in which this structure is the global minimum on the energy landscape.

Although the basin-hopping global optimisation method relies upon a hypersurface deformation,[24,132] which removes the barriers on the potential energy landscape, the success rate of this method in finding the global minimum reflects the complexity of the landscape, which would have some impact on the kinetics. It is noteworthy that a series of basin-hopping steps do not correspond to a physical dynamical process. As θ assumed a non-zero value, an indication for reduced complexity and improved kinetics was apparent in a significant enhancement of the success rate for the basin-hopping global optimisation method to find the snub cube structure as the global minimum on the potential energy landscape within a certain pre-fixed number of basin-hopping steps. When identical sets of 20 random starting configurations were considered for half a million basin-hopping steps, the success of finding the global minimum was only 5% for $\theta = 0°$ as opposed to 100% for both $\theta = 5°$ and $\theta = 10°$. The mean first encounter times differed only by approximately 4% between $\theta = 5°$ and $\theta = 10°$ – not significant enough for comparing their kinetic accessibility conclusively.

In order to draw a comparison of the hollow spheroidal structures for different θ values in terms of their kinetic accessibility when the underlying energy landscape is sampled at a non-zero temperature, we carried out Monte Carlo simulations to sample equilibrium configurations, while the temperature $T^\star$ was gradually reduced. In the context of emerging structural hierarchy, single-particle Monte Carlo moves for the elementary building blocks were known to be inadequate.[66] The dominant pathway for the hierarchical self-assembly into a structure topologically equivalent to the snub tetrahedron for $N = 12$ and $\theta = 10°$ was found by means of a rare event simulation technique to proceed stagewise via the formation of trimers.[68] It was therefore reasonable to anticipate that a staged assembly pathway would most likely be followed for the emergence of structural hierarchy in this case. We thus performed Monte Carlo simulations with the trimers formed at the first level of the assembly, and carried out single-particle moves treating these secondary units as rigid bodies. The secondary units with

dipoles in planar flux-closure arrangements, as shown in **Figure 5.1b**, were distinct for each value of θ. The distinct structural features are tabulated in **Table** 5.1. 10 independent Monte Carlo simulations were carried out with $N_t = 8$ rigid secondary units for all three θ values, each within an identical spherical container. The data shown in **Figure 5.2** are corresponding to the spherical container of radius 2.5 in the reduced unit, while the radius of gyration is 1.405 for the snub cube structure corresponding to the value of $\theta = 10°$. The formation of a hollow spheroidal structure was monitored with the relative shape anisotropy parameter κ^2 as shown in **Figure 5.2**, and was also confirmed by visual inspection. For a hollow spheroidal structure such as the snub cube, $\kappa^2 \approx 0$. While we observed the formation of the snub cube structure for all three θ values as evident in **Figure 5.2**, the success rate varied considerably. The success rate was 10% for $\theta = 0°$, increasing to 40% for $\theta = 5°$ and further to 80% for $\theta = 10°$. The trend was thus clearly evident. As a representative case, for $\theta = 0°$ for which the success rate was the least, we considered bigger spherical containers to investigate whether the snub cube structure was formed for a container size varying over a reasonable range; we indeed observed the formation of the snub cube structure up to a radius of 5 in the reduced unit.

θ	$0°$	$5°$	$10°$
R_{cc}	0.963	0.955	0.949
r_{dd}	0.667	0.637	0.612
ϕ	$30.92°$	$30.42°$	$29.67°$

Table 5.1: The structural features that make the planar trimers formed at the intermediate level distinct for the three values of the model parameter θ studied. Here R_{cc} denotes the distance between the geometric centres of adjacent colloidal particles, r_{dd} is the distance between the corresponding point-dipoles, and ϕ is the angular displacement between the triangles formed by the geometric centres and those by the point-dipoles on the plane. These distances are in the reduced unit.

The free-energy profiles for the formation of the hollow spheroidal structures, as shown in **Figure 5.3**, were found to be consistent with the gradual increase in their kinetic accessibility as θ was varied from 0° to 10°. The free-energy profiles were obtained by the umbrella sampling technique, where the order parameter κ^2 was used as the reaction coordinate. For each θ value, the umbrella sampling simulations were undertaken at the respective temperatures at which the formation of the hollow spheroidal structures was first observed upon cooling. The biased Monte Carlo simulations were carried out with rigid secondary units, distinct for each θ value, with single-particle moves. The self-assembly of the colloidal particles into the snub cube structure,

which is of octahedral symmetry, is expected to incur an entropy cost. **Figure 5.3** shows that the snub cube structure was indeed the global minimum on the free energy profile for all three θ values, despite the entropy cost. It is also evident in **Figure 5.3** that the free energy barrier to the formation of the snub cube structure gradually decreased as the model parameter θ was increased from 0°, thus leading to increased kinetic accessibility. From our analysis, it is reasonable to say that the free energy barrier to formation of the snub cube structure has largely energy contributions rather than entropic. The assembly of the snub cube structure from the trimers draws thermodynamic driving forces arising from the "bonds" between adjacent trimers due to favourable anti-parallel dipole-dipole interactions. The analysis of the energetics in the global minimum structures reveals the following energies for these interactions: -6.372, -5.594, -4.832 in the units of energy for 0°, 5°, and 10°, respectively. As it is apparent in **Figure 5.3**, the formation of the snub cube structure requires rearrangements of the trimers involving breaking of these bonds, which is strongest for the 0° case and gradually becomes weaker. This consideration thus explains the trend in the free energy barrier observed in **Figure 5.3** as the angular parameter θ varies.

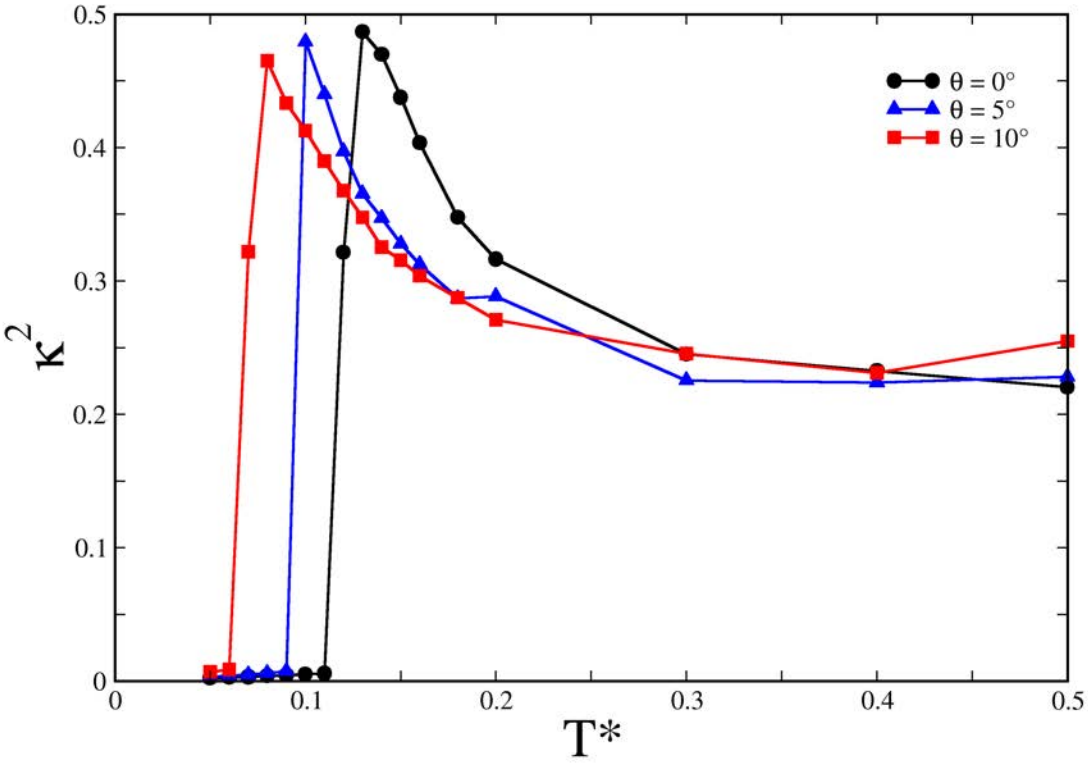

Figure 5.2: The relative shape anisotropy κ^2 as a function of the reduced temperature $T^\star$ in Monte Carlo simulations of $N_t = 8$ rigid trimers for three different θ values. Data from a typical run in which the hollow spheroidal structure was successfully formed are shown.

Since the aforementioned series of Monte Carlo simulations were performed with the rigid secondary units, these simulations could capture only the second stage of assembly. In order to garner a complete picture, we also performed Monte Carlo simulations of the primary building blocks for all three θ values, using the virtual-move Monte Carlo (VMMC) algorithm.[142] The VMMC algorithm implements cluster moves, and thus promises to be effective for sampling with the primary building blocks in this case. We carried out 10 independent VMMC simulations of $N = 24$ colloidal magnetic particles within a fixed spherical container for each of the three θ values. As the temperature $T^\star$ was gradually decreased for the VMMC simulations, the formation of the snub cube structure demonstrating a remarkable two-level structural hierarchy was observed for $\theta = 5°$ and $10°$, as revealed by the evolution of the order parameter κ^2 (**Figure 5.4**). The desired snub cube structure was formed with a 30% success rate for $\theta = 5°$ and with a 60% success rate for $\theta = 10°$. However, for $\theta = 0°$, the snub cube structure was not

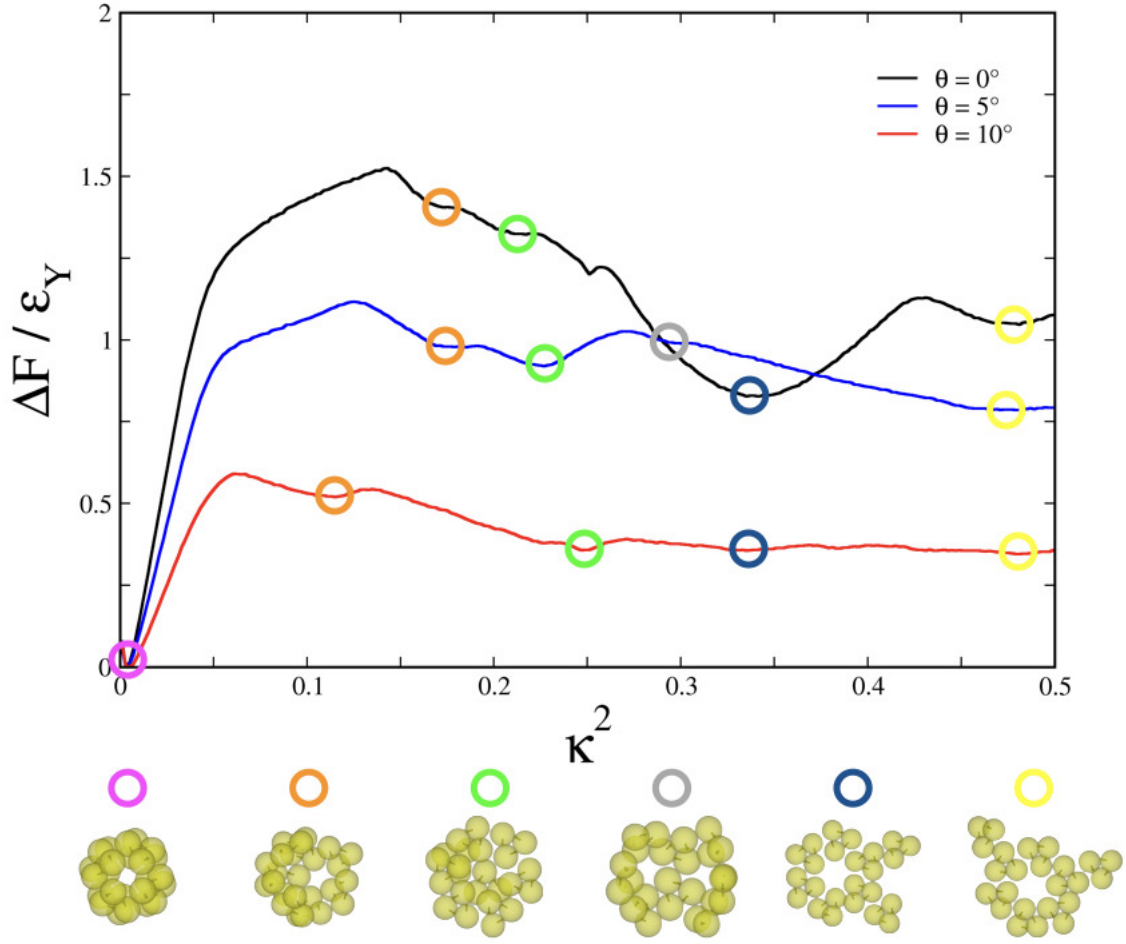

Figure 5.3: The free energy profiles as a function of the order parameter κ^2 for finite-size clusters of $N_t = 8$ rigid trimers for three different θ values. The free energy profiles were obtained by performing umbrella sampling simulations at different reduced temperatures: $T^\star = 0.11$ for $\theta = 0°$ (black), $T^\star = 0.08$ for $\theta = 5°$ (blue), and $T^\star = 0.07$ for $\theta = 10°$ (red). Colored rings highlight metastable minima on the free energy profiles; the corresponding structures are shown.

obtained in any of these simulation runs. In fact, we did not observe even the formation of the requisite number of trimers in a single instance for $\theta = 0°$, implying that the first stage of the assembly was not completed correctly in this case. The results of the VMMC simulations thus unequivocally provided evidence that the hollow spheroidal structure was most kinetically accessible for $\theta = 10°$. A spherical container of radius 2.5 in the reduced unit was used for the data in **Figure 5.4**. For the representative case of $\theta = 10°$, additional data, not shown here, confirmed the formation of the snub cube structure with spherical containers up to the radius of 4 in the reduced unit.

The hollow spheroidal structure, despite being thermodynamically favourable, proved elusive for $\theta = 0°$. While a staged pathway was most probable, it was striking that the first stage

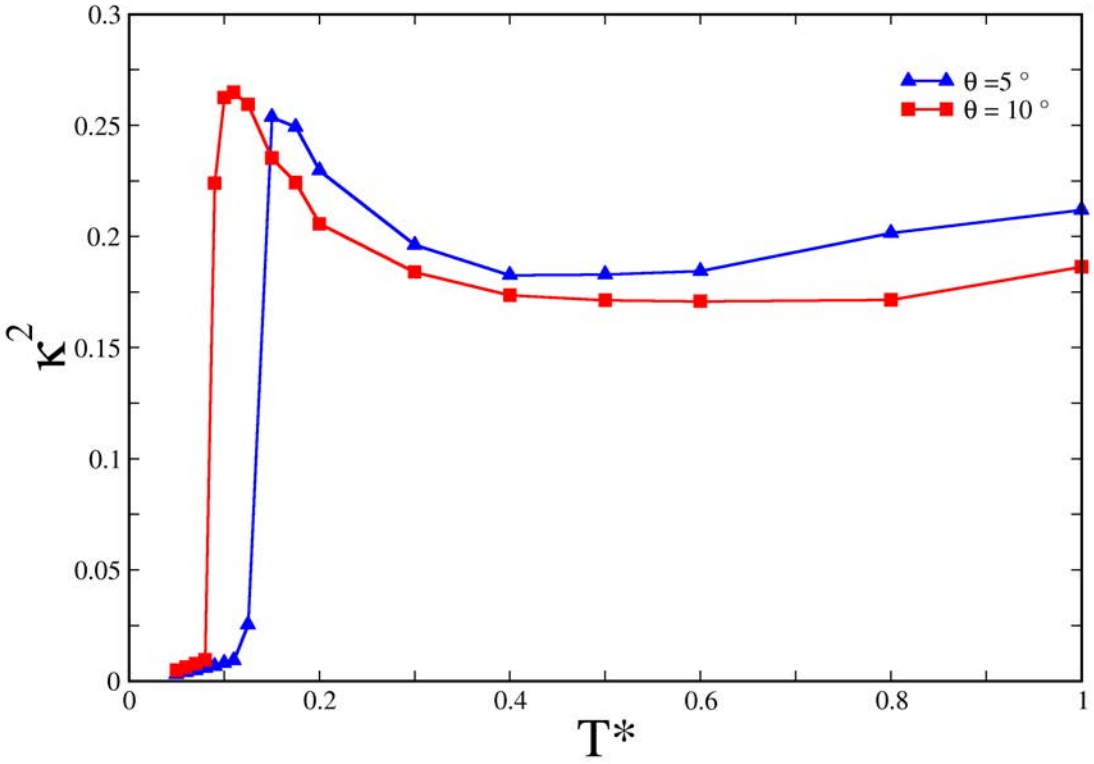

Figure 5.4: The relative shape anisotropy κ^2 as a function of the reduced temperature $T^\star$ in virtual-move Monte Carlo simulations of $N = 24$ colloidal magnetic particles for two different θ values. Data from a typical run in which the hollow spheroidal structure was successfully formed are shown.

of the self-assembly into the trimers could not be achieved in our VMMC simulations. This observation, in particular, led us to analyse the energetics of the snub cube structure, which shows a two-level structural hierarchy, and compare the energetic stabilities gained at each level of the assembly for all three θ values, as shown in **Table** 5.2. The analysis revealed a remarkable correspondence between the relative energetic stabilities gained at successive levels of the assembly, as shown schematically in **Figure 5.5**, and the kinetic accessibility of the hollow spheroidal structure as the model parameter θ was varied. It is clearly evident that the thermodynamic driving forces arising from the energetic stability gained through the formation of a trimer at the first level of the assembly increased as θ increased from $\theta = 0°$ to $\theta = 10°$. This resulted in the formation of increasingly more stable secondary building units. The second stage of assembly brought together eight such secondary building units to form the snub cube structure. The difference in the potential energy between the snub cube structure and eight

independent trimers, which appears in the column denoted by ΔE_{12} in Table 5.2, accounts for the thermodynamic driving force behind the second stage of the assembly. It thus follows that the thermodynamic driving force for the second stage of the assembly gradually decreased as θ was varied from $\theta = 0^\circ$ to $\theta = 10^\circ$. The energetic stability was drawn from nearly anti-parallel arrangements for pairs of dipoles in neighbouring secondary units emerging from the second stage of the assembly.

θ	E_1	E_2	ΔE_{12}
0°	-31.294	-275.225	-24.873
5°	-35.761	-304.189	-18.101
10°	-40.395	-336.721	-13.561

Table 5.2: The energetics of the two-level hierarchical self-assembly for three different values of the model parameter θ. In each case, E_1 stands for the potential energy of the global minimum for $N = 3$ colloidal magnetic particles, E_2 is the potential energy of the global minimum corresponding to the hollow spheroidal structure, and ΔE_{12} the difference in potential energy: $\Delta E_{12} = E_2 - 8E_1$, denoting the energetic stability gained from the second stage of assembly.

The striking correspondence between the thermodynamics and kinetics of the self-assembly into a two-level structural hierarchy, as revealed here, called for an explanation. For the success of programmed self-assembly into a target structure, the microscale colloidal particles need to negotiate the so-called kinetic traps, which arise from the presence of metastable "wrong" structures in the free-energy landscape.[231] Reversible association allows for facile annealing of defects, and hence removal of kinetic traps. Such reversibility is best achieved here at the expense of relatively weak thermodynamic driving forces for the second stage of assembly. In the present case, the hierarchical self-assembly followed a staged pathway, in which the trimers formed in the first stage of assembly served as the secondary building blocks in the course of the second stage of assembly while retaining their integrity. Such a pathway involved concerted movements of the colloidal particles over the course of the second stage of assembly, incurring an entropy contribution to the free energy barrier. The more energetically stable the secondary building blocks, the higher would be the energy penalty for any alternative pathway involving the loss of integrity of the secondary building blocks, and hence the more facile the staged assembly pathway from the perspective of free energy barrier.

It follows from the results presented here that a hierarchy of interactions is crucial for a staged assembly pathway to structural hierarchy. Such a hierarchy of interactions allows us

to consider a staged disassembly into the secondary building blocks and their reassembly, as shown in **Figure 5.6** for the case of $\theta = 10°$, by the application of a weak external magnetic field in the first place and then turning it off. The strength of the magnetic field was so chosen that it could open up the snub cube structure while retaining the integrity of the trimers. For the data shown in **Figure 5.6**, $B = 0.25$ at $T^\star = 0.07$. This demonstration suggests that a weak magnetic field could, in principle, be also exploited to induce staged disassembly of any "wrong" structure obtained from the second stage of assembly. The ease of disassembly that such an operational hierarchy of interactions implies may have implications for disassembly observed for viral capsids.[249]

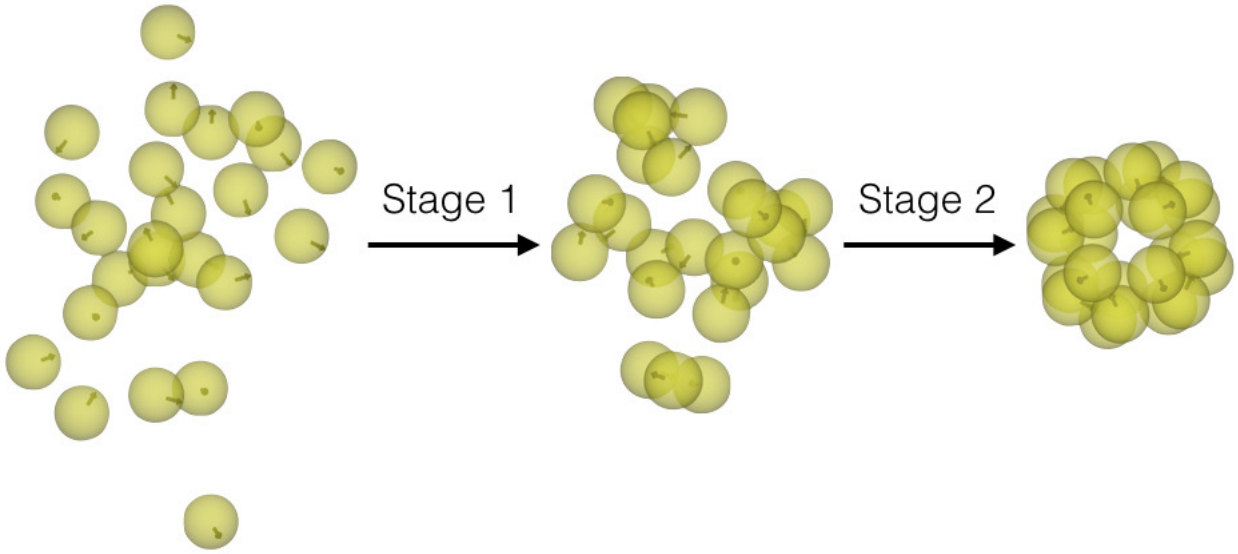

Figure 5.5: A schematic illustration of the staged assembly pathway leading to the hollow spheroidal structure, which displays a two-level structural hierarchy, as revealed in a typical virtual-move Monte Carlo simulation run. Starting from a random initial configuration (left), 8 colloidal trimers are formed in the first stage of assembly ($T^\star \approx 1.0$); the trimers formed in the first stage thus serve as the building blocks in the course of the second stage to form the hollow spheroidal structure ($T^\star \approx 0.07$).

5.4 Conclusion

In the present study we employed a variety of computational methods to examine the kinetic accessibility of a series of hollow spheroidal structures, each displaying a remarkable two-level structural hierarchy, self-assembled from charge-stabilised colloidal magnetic particles. For these designer building blocks, which were modeled after recently synthesised colloidal magnetic

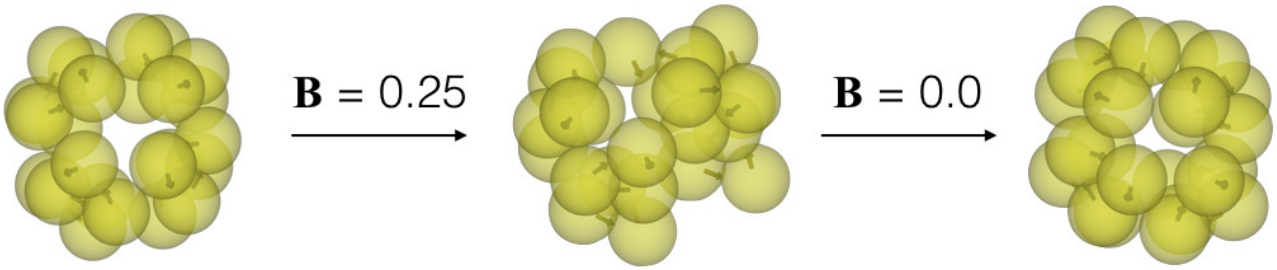

Figure 5.6: A controlled disassembly of the snub cube structure into the trimers by the application of a static magnetic field and reassembly of the trimers into the snub cube structure in the absence of the field.

particles,[176] a model parameter was varied across the series, resulting in a gradual change in the energetics. We found that for a staged assembly pathway, the structure, which derived the strongest energetic stability from the first stage of the assembly and the weakest from the second stage, was most kinetically accessible. We accounted for such a striking correspondence between the thermodynamics and kinetics for optimal design principles, which should have general implications for programming hierarchical self-assembly pathways for nano- and micro-particles, while matching stability and accessibility. The present scenario should be distinguished from those where thermodynamic or kinetic control prevail so that a structure is observed either because it is the most stable state or because the pathway leading to it has the lowest free energy barrier.[231]

We further note that it is quite likely that an experimental system would have some degree of dispersity in the dipole direction. Given the global stability of the hollow spheroidal structure for a range of θ values, one would expect that the formation of such structures would have some level of tolerance to this dispersity, though the symmetry of the structure would then be reduced. The study of a model system with the dispersity of the dipole direction was, however, beyond the scope of the present investigation.

Chapter 6

Programming Hierarchical Self-assembly of Patchy Particles into Colloidal Crystals via Colloidal Molecules

6.1 Introduction

The scope for tuning the interactions between colloidal particles offers enormous opportunity to programme their self-assembly.[3,22,250] In particular, hierarchical self-assembly of colloidal particles, which is currently at an early stage of exploration,[66,97,98,102,218,238,251] offers a bottom-up route to increased level of structural complexity. However, programming hierarchical self-assembly faces a major challenge in bridging hierarchies of multiple length- and time-scales associated with structure and dynamics respectively, along the self-assembly pathways.[235] While hierarchical self-assembly of colloidal particles via small colloidal clusters mimicking the symmetry of molecular structures, *i.e.* the so-called "colloidal molecules",[15,23,235,252] could be a plausible route to structural hierarchy, a generic design principle for programming colloidal self-assembly hierarchically is still lacking. Another major challenge that such a route faces is to assemble the colloidal molecules in a self-limiting way for them to serve as monodisperse secondary building blocks for the next level of assembly.[253]

In **Chapter 5** we examined the kinetic accessibility of a series of hollow spheroidal structures

with a two-level structural hierarchy self-assembled from charge-stabilised colloidal magnetic particles. The study reports that for a staged assembly pathway, the structure, which derives the strongest energetic stability from the first stage of assembly and the weakest from the second stage, is most kinetically accessible. In this context, we hypothesised that a hierarchy of interaction strengths could be a propitious route to structural hierarchy. In the present study, we realise a hierarchy of interaction strengths with triblock patchy colloidal particles in order to test this hypothesis. Our designer patchy particles are spherical in shape, having two distinct attractive patches A and B at the poles across a charged band in the middle. Such triblock spherical particles were recently synthesised at the micron scale and shown to undergo staged assembly triggered by stepwise change of the ionic strength of the medium (**Figure 6.1**).[97] However, the assembly at the first stage produced a distribution of cluster sizes, including tetramers and hexamers, posing serious limitations to the formation of colloidal crystals in the next stage.[97]

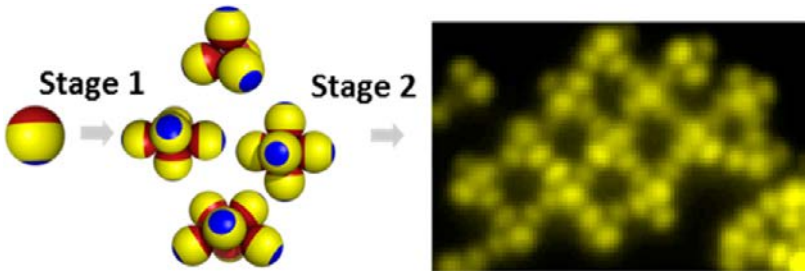

Figure 6.1: The staged assembly of triblock patchy particles demonstrated by Chen *et al.*[97] Here stepwise change in the ionic strength of the medium induces a staged self-assembly process. Copyright (2012) America Chemical Society.

The formation of uniform tetrahedral clusters in a self-limiting way has, in particular, the potential of opening up a novel route to the much sought-after cubic diamond lattice. Despite being an attractive target for programmed colloidal self-assembly, cubic diamond colloidal crystals, which have potential applications as a three-dimensional complete photonic band gap material,[254,255] have proved remarkably difficult to realise via self-assembly. A number of strategies have been explored so far.[11,85,103,105,173,256,257] One strategy exploited an interplay between a long-range repulsion and a short-range attraction, both isotropic in nature, at the nanoscale to stabilise a diamond-like open lattice for two oppositely charged nanoparticles.[256] An alternative strategy prescribes the use of anisotropic interactions realised through patchy colloidal particles decorated with four patches in tetrahedral symmetry.[11,85,173,258] This route faces the

challenge of resolving the competition from thermodynamically preferred tetrahedral liquid or gel.[11,173,258,259] In a related strategy, tetrahedral DNA origami constructs were employed with two types of gold nanoparticles coated with designer single-stranded DNA to form a cubic diamond lattice.[257] However, in this case the spacing between the nanoparticles in the lattice was considerably larger than the core diameter of the nanoparticles, which could restrict its appeal as a photonic crystal.[105] Another distinct route to open structures, such as the cubic diamond lattice, is to first form a denser lattice with two compositionally distinct species each forming a sub-lattice, one of which is the cubic diamond lattice as in the case for the $MgCu_2$ Laves phase.[103] The removal of the second sub-lattice selectively produces the cubic diamond lattice as an open structure. This route was followed in a recent work, which employed DNA mediated interactions to guide preassembled tetrahedral colloidal clusters and spheres to form the $MgCu2$ Laves phase.[105]

Here we validate our hypothesis in computer simulations to establish a generic rule to programme hierarchical self-assembly, exploiting a hierarchy of interaction strengths. In particular, we demonstrate the hierarchical self-assembly of triblock patchy particles into a cubic diamond lattice via tetrahedral clusters, thus opening up a new strategy for its experimental realisation. Additionally, for a wider patch width and a longer patch-patch interaction range, we show that these triblock patchy particles hierarchically self-assemble into a body-centered cubic and simple cubic crystals via octahedral clusters, thus lending generality to our design principle.

6.2 Methodology

6.2.1 The Model

We employed the traditional one-component description for the colloidal suspensions considered here with a pairwise effective potential.[260] In this description, triblock patchy colloidal particles are modeled as rigid bodies consisting of a spherical core decorated with two distinct patches, A and B, located on opposing poles across a charged middle band. The effective potential has an isotropic component in the form of the Yukawa potential describing screened electrostatic repulsion and an anisotropic component, which describes the directional interactions between patches. The interaction potential used here has some similarity with the widely used Kern and

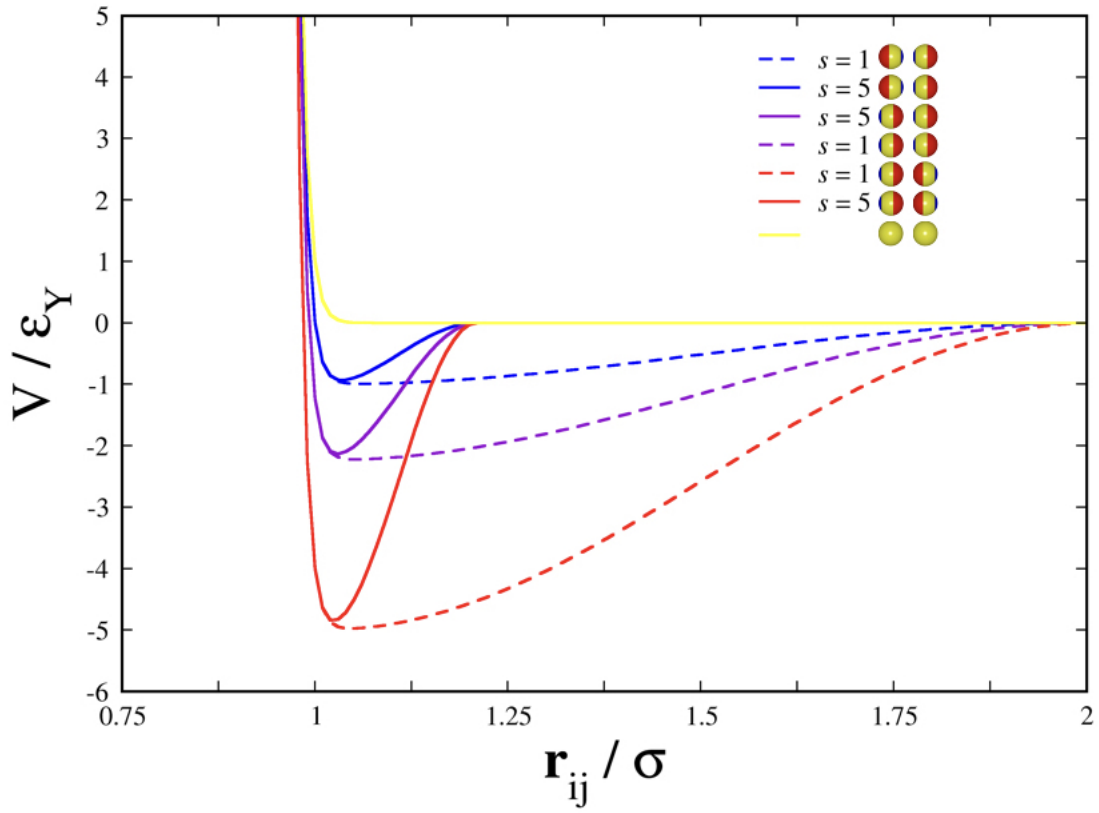

Figure 6.2: The effective pair potential for the patchy particles under consideration as a function of separation for three different orientations and two values of the model parameters. The following model parameters are kept constant: $\epsilon_{AA} = 5$, $\epsilon_{BB} = 1$, $\alpha = 80°$, $\beta = 40°$, $\kappa = 100$. The isotropic component, given by the Yukawa potential U_{Y},is shown separately in yellow.

Frenkel model,[53] especially in the way the patch-patch interaction is described. However, the isotropic part of the present potential is described by a Yukawa potential without a hard core, and the anisotropic patch-patch interaction is continuous instead of a square-well potential with angular modulation. The present potential thus avoids any discontinuity, and is suitable for Brownian Dynamics simulation. In our model, both patches A and B are able to interact with themselves and one another. Patches A and B differ in terms of their surface coverage, characterised by the angles α and β which describe their half-patch widths respectively, and the strength of their patch-patch interactions. ϵ_{ij} is the depth of the potential due to the patch i - patch j interaction when the two patches face each other. The effective potential for a pair of patchy particles V is given by

$$V(\boldsymbol{r}_{ij}, \boldsymbol{\Omega}_i, \boldsymbol{\Omega}_j) = U_{\mathrm{Y}}(r_{ij}) + \sum_{p \in i} \sum_{p' \in j} U_{pp'}(\boldsymbol{r}_{ij}, \boldsymbol{\Omega}_i, \boldsymbol{\Omega}_j) w_{pp'}(r_{ij}) \tag{6.1}$$

where $\boldsymbol{r}_{ij} = \boldsymbol{r}_j - \boldsymbol{r}_i$ is the separation vector between triblock patchy particles i and j, $\boldsymbol{r}_i$ is the position vector for the geometric center of the patchy particle i and r_{ij} the magnitude of the vector $\boldsymbol{r}_{ij}$. $\boldsymbol{\Omega}_i$ and $\boldsymbol{\Omega}_j$ describe the orientations of particles i and j, respectively. The isotropic component U_{Y} is the repulsive Yukawa potential

$$U_{\mathrm{Y}}(r_{ij}) = \epsilon_{\mathrm{Y}} \frac{\exp[-\kappa(r_{ij} - \sigma)]}{r_{ij}/\sigma}, \tag{6.2}$$

where κ is the inverse Debye screening length and ϵ_{Y} is the contact potential. The angular dependence of the patch-patch interaction is described by $U_{pp'}$:[59]

$$U_{pp'}\left(\boldsymbol{r}_{ij}, \boldsymbol{\Omega}_i, \boldsymbol{\Omega}_j\right) = \epsilon_{pp'} \frac{1}{4} \left[1 + \Phi\left(\boldsymbol{r}_{ij}, \boldsymbol{\Omega}_i, \boldsymbol{p}_i\right)\right] \left[1 + \Phi\left(\boldsymbol{r}_{ji}, \boldsymbol{\Omega}_j, \boldsymbol{p}_j\right)\right], \tag{6.3}$$

$$\Phi\left(\boldsymbol{r}_{ij}, \boldsymbol{\Omega}_i, \boldsymbol{p}_i\right) = \begin{cases} -1, & \cos\theta_{ijp_i} < \cos\delta, \\ -\cos\left(\dfrac{\pi\left[\cos\theta_{ijp_i} - \cos\delta\right]}{1 - \cos\delta}\right), & \cos\theta_{ijp_i} \geq \cos\delta. \end{cases} \tag{6.4}$$

The depth of the patch-patch interaction is given by $\epsilon_{pp'}$. Here $\boldsymbol{p}_i$ is a normalised vector from the center of the spherical particle i in the direction of the patch p on it, which depends on $\boldsymbol{\Omega}_i$, and $\cos\theta_{ijp_i}$ is the scalar product of the normalised vector $\hat{\boldsymbol{r}}_{ij}$ with $\boldsymbol{p}_i$. The width of the patches is controlled by the parameter $\cos\delta$.

The distance dependence of the patch-patch interaction is governed by the function $w_{pp'}$:

$$w_{pp'}\left(r_{ij}\right) = \begin{cases} -1, & \text{if } (r_{ij} - \lambda) < 0, \\ -\frac{1}{2}\left[1 + \cos\left(\pi\left(r_{ij} - \lambda\right)s\right)\right], & \text{if } 0 \leq (r_{ij} - \lambda) \leq s^{-1}, \\ 0, & \text{if } (r_{ij} - \lambda) > s^{-1}, \end{cases} \tag{6.5}$$

where λ is the largest separation at which the patch p - patch p' attraction is at its strongest and the parameter s controls the range over which this attraction decreases to zero. In the present study, λ was set to 1.01σ. We used reduced units: the length in the units σ, the energy in the units of ϵ_{Y}, and the temperature in the units of $\epsilon_{\mathrm{Y}}/k_{\mathrm{B}}$. In the absence of a hard core σ provides an estimate for the size of the charge-stabilised patchy particles. We set $\epsilon_{AB} = \sqrt{\epsilon_{AA}\epsilon_{BB}}$.

6.2.2 Simulation Details

Structure Prediction for Clusters

We employed the basin-hopping global optimisation method to identify global minima on the potential energy surface for size-selected clusters.[24,132] The global minima are the candidates for thermodynamically favoured structures observed under experimental conditions especially at low temperatures. An angle-axis representation was used for rigid-body rotational coordinates.[123] The limited-memory Broyden-Fletcher-Goldfarb-Shanno algorithm was used for local minimization with analytic first derivatives of the potential energy.[137] For each set of potential parameters, we carried out 5 independent runs, starting from 5 random initial configurations. The runs consisted of a minimum of 5×10^5 basin-hopping, varying by an order of magnitude.

Virtual Move Monte Carlo

A series of virtual-move Monte Carlo (VMMC) simulations were performed in the canonical ensemble with $N = 500$ triblock patchy particles. The simulations were carried out in a cubic box under periodic boundary conditions using the minimum image convention. We employed the symmetrised version of the virtual-move Monte Carlo algorithm.[142–144] The orientational degrees of freedom were represented by quaternions. Each VMMC cycle consisted of N translation or collective rotational cluster moves, chosen at random with equal probability. The maximum step size for both the translational and collective rotational cluster moves were fixed, taken as $\delta = 0.1$ in the reduced unit and $\theta_{max} = 0.1$, respectively. The potential energy was calculated using a spherical cut-off of radii 1.3σ and 2.1σ for the sets of potential parameters with $s = 5$ and 1, respectively. A neighbour list was used for efficiency. The systems were equilibrated from an initial face-centered lattice at $T^\star = 1.0$ and $T^\star$ was gradually reduced. At each $T^\star$ value studied, at least 1×10^6 VMMC cycles were used for equilibration, which was followed by a production stage consisting of 5×10^5 cycles for high values of $T^\star$ and 1.5×10^6 cycles for lower values of $T^\star$.

Brownian Dynamics

Brownian dynamics (BD) simulations were undertaken in the canonical ensemble with $N = 864$ triblock patchy particles. The simulations were conducted in a cubic box under periodic bound-

ary conditions using the minimum image convention. In these simulations the particle positions and orientations were propagated following a widely used BD algorithm.[196] The orientational degrees of freedom were represented by unit vectors. The translational and rotational diffusion coefficients at infinite dilution are given by appropriate Stokes' laws with sticky boundary conditions. For BD simulations, the time is expressed in the units of σ^2/D_0^t, where D_0^t is the translational diffusion coefficient at infinite dilution. The potential energy, force and torque were calculated using a spherical cut-off of radii 1.3σ and 2.1σ for the sets of parameters $s = 5$ and 1, respectively. A neighbour list was used for efficiency. The systems were equilibrated from an initial face-centred cubic lattice at $T^\star = 1.0$ and $T^\star$ gradually reduced. At each value of $T^\star$ studied, a minimum of 2×10^7 steps were used for equilibration, followed by a production stage of of 1×10^7 steps. Below a reduced temperature of $T^\star = 0.10$ a time step of $\Delta t = 5 \times 10^{-5}$ in the reduced unit was used, for all other values of $T^\star$ a timestep of $\Delta t = 10^{-5}$ in the reduced unit was used.

Steinhardt Local Bond Order Parameter

We calculated various Steinhardt local bond-orientational order parameters, based on spherical harmonics, as diagnostics for identifying ad distinguishing between crystal structures.[261,262] To identify both the body-centred cubic and simple cubic crystal structures we calculated the following averaged Steinhardt local bond-orientational order parameters for $l = 4$ and $l = 6$:[263]

$$\bar{q}_l(i) = \sqrt{\frac{4\pi}{2l+1} \sum_{m=-l}^{+l} |\bar{q}_{lm}(i)|^2} \tag{6.6}$$

where,

$$\bar{q}_{lm}(i) = \frac{1}{\tilde{N}_b(i)} \sum_{k=0}^{\tilde{N}_b(i)} q_{lm}(k) \tag{6.7}$$

Here, by summing over $k = 0$ to $\tilde{N}_b(i)$ when calculating $\bar{q}_{lm}(i)$, we take into account all of the neighbours of particle i as well as the particle i itself. This averaging process, which considers both the first and the second shell around a particle, was shown to considerably

improve the accuracy in distinguishing among body-centred cubic, face-centred cubic, simple cubic and hexagonally close packed crystal structures.[263]

In order to specifically distinguish between the cubic diamond (DC) crystal and hexagonal diamond (DH) crystal, we calculated the complex conjugate scalar product $\tilde{\boldsymbol{q}}_3(i) \cdot \tilde{\boldsymbol{q}}_3^{\star}(j)$.[11,85] For every particle i its four nearest neighbours were considered to define the normalised seven-component complex vector $\tilde{\boldsymbol{q}}_3(i)$ with components

$$\tilde{q}_{3m}(i) = \frac{q_{3m}(i)}{\left[\sum_{m=-3}^{3} |q_{3m}(i)|^2\right]}. \tag{6.8}$$

When the probability distribution of the complex conjugate scalar product $\tilde{\boldsymbol{q}}_3(i) \cdot \tilde{\boldsymbol{q}}_3^{\star}(j)$ is plotted for these two crystals, in their perfect forms both show a peak at -1, but the presence of peak around -0.115 is a signature of the hexagonal diamond crystal.[11] In the perfect DC crystal all four neighbours j of each particle i are so arranged such that $\tilde{\boldsymbol{q}}_3(i) \cdot \tilde{\boldsymbol{q}}_3^{\star}(j) = -1$, where as for the perfect DH crystal each particle i has three neighbours for which $\tilde{\boldsymbol{q}}_3(i) \cdot \tilde{\boldsymbol{q}}_3^{\star}(j) = -1$ and one such that $\tilde{\boldsymbol{q}}_3(i) \cdot \tilde{\boldsymbol{q}}_3^{\star}(j) = -0.115$.[11]

Tetrahedral and Octahedral Orientational Order Parameter

Clusters of 4 or 6 particles were identified in order to determine the number of tetrahedra or octahedra formed in the respective system. The cluster identification was carried out using a threshold value for the distance between the centres of patch A on two neighbouring particles, below which the particles were taken to belong to the same cluster. While examining a cluster of 4 or 6 particles in order to assess whether the particles have a tetrahedral or octahedral arrangement, we employed the following orientational order parameter q:[264,265]

$$q = 1 - \frac{3}{8} \sum_{j=1}^{N_b-1} \sum_{k=j+1}^{N_b} (\cos\psi_{jk} + \frac{1}{3})^2, \tag{6.9}$$

where N_b is the number of particles in the cluster under consideration and ψ_{jk} is the angle subtended at the centre of the cluster by the two vectors joining the centre to particles j and k. In the case of a perfect tetrahedron $q = 1$ with $N_b = 4$; for a perfect octahedron $q = 0$ with

$N_b = 6$.[266] We used threshold values to identify a cluster as tetrahedron or an octahedron.

6.3 Results

In the present study, we used a hierarchy of patch-patch interactions, $\epsilon_{AA} > \epsilon_{AB} > \epsilon_{BB}$, where ϵ_{ij} is the depth of the potential due to the patch i - patch j interaction when the patches face each other, together with screened electrostatic repulsion between the middle bands. **Figure 6.2** demonstrates the different interactions between the designer patchy particles considered here. **Figure 6.3** shows the most stable structures for certain size-selected clusters on the respective potential energy surfaces for two sets of potential parameters: (1) $\epsilon_{AA} = 5$, $\epsilon_{BB} = 1$, $\alpha = 80°$, $\beta = 40°$, $s = 5$, and $\kappa = 100$; (2) $\epsilon_{AA} = 5$, $\epsilon_{BB} = 1$, $\alpha = 85°$, $\beta = 40°$, $s = 1$, and $\kappa = 100$. For both parameter sets, a remarkable two-level structural hierarchy is on display via distinct colloidal molecules at the intermediate level in the form of tetrahedra and octahedra respectively. We determined the sets of parameters that support such striking structural hierarchy by employing the method of basin-hopping global optimisation to identify the global minima on the potential energy surface for size-selected clusters. While the key to the observed structural hierarchy is the hierarchy of patch-patch interaction strengths, the morphology of the colloidal molecules, which essentially serve as the secondary building blocks, is governed by the width of the stronger patch and the range of the patch-patch interactions. A longer range for the patch-patch interactions, indicated by a smaller value of the parameter s (see **Figure 6.2**), and a slightly larger width for the stronger patch favour increased coordination, resulting in the formation of larger clusters at the intermediate level. The closed-loop structure formed with the tetrahedral clusters, as shown in **Figure 6.3**, resembles a 6-membered ring in terms of the secondary building blocks in the so-called 'chair' form. The 'boat' form, shown in **Figure 6.4**, was also found with negligible difference in potential energy. The formation of such ring structures suggested the appealing prospect of hierarchical self-assembly of the patchy particles into open lattices with local tetrahedral order,[267] especially diamond crystals.[11,12,85,106]

In the context of the promising results obtained in global optimisation runs for size selected clusters, it was imperative that the assembly of these patchy particles be studied in periodic systems, while gradually decreasing the reduced temperature $T^\star$. In the following, we present our results obtained from three series of virtual-move Monte Carlo (VMMC) and Brownian

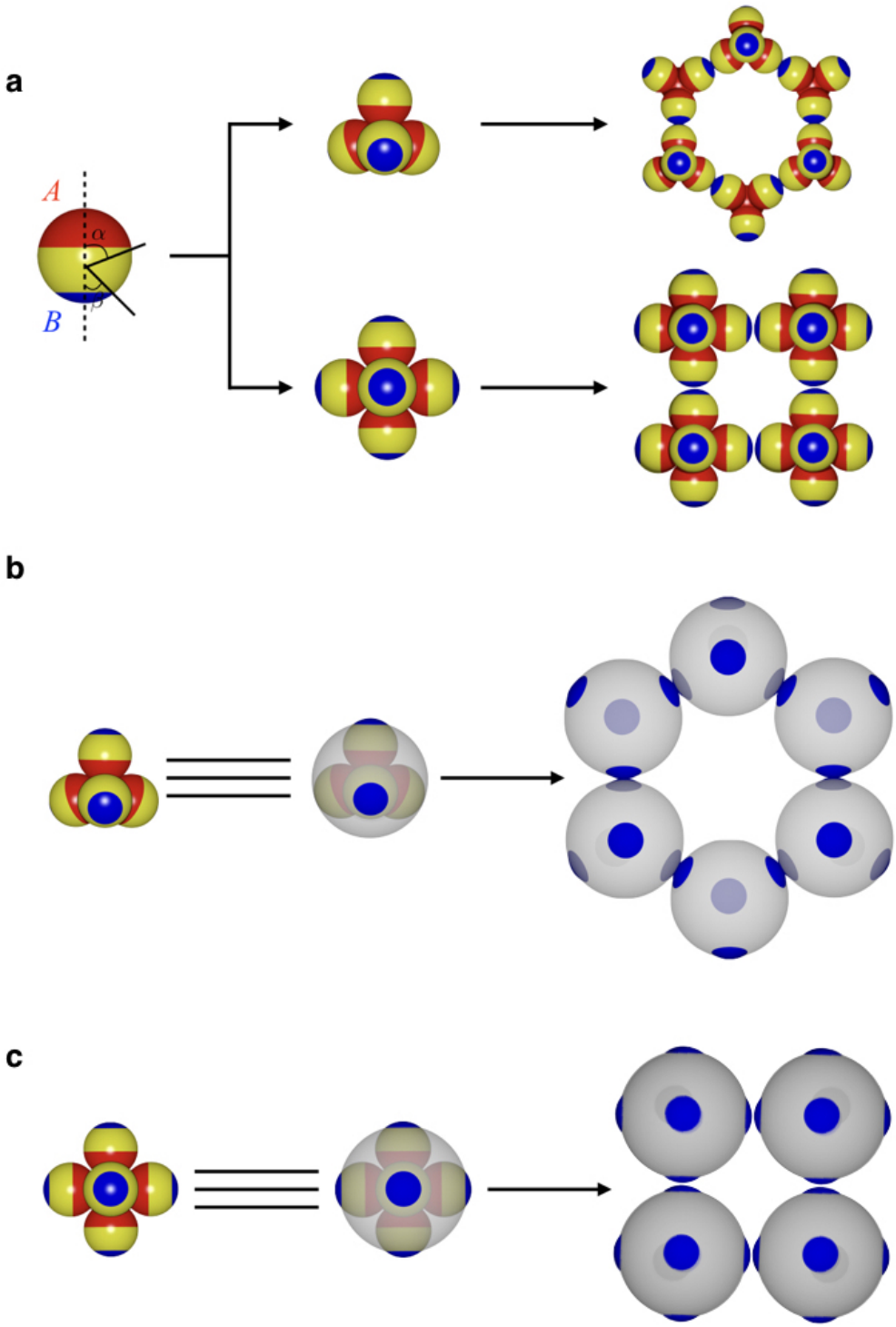

Figure 6.3: The most stable structures for size-selected clusters of patchy particles under consideration for two sets of model parameters. **a.** For one set, $\epsilon_{AA} = 5$, $\epsilon_{BB} = 1$, $\alpha = 80°$, $\beta = 40°$, $\kappa = 100$, and $s = 5$, a ring-like structure is formed for $N = 24$ with tetrahedral subunits (top). For the other set, $\epsilon_{AA} = 5$, $\epsilon_{BB} = 1$, $\alpha = 85°$, $\beta = 40°$, $\kappa = 100$, and $s = 1$, octahedral subunits appear in a structure of four-fold symmetry (bottom). **b.** The ring structure in a reduced representation, showing spheres with tetrahedral patches centred at the geometric centres of the tetrahedral subunits and having the same orientations. **c.** The structure with four-fold symmetry in a reduced representation, showing spheres with octahedral patches centred at the geometric centres of the octahedral subunits and having the same orientations.

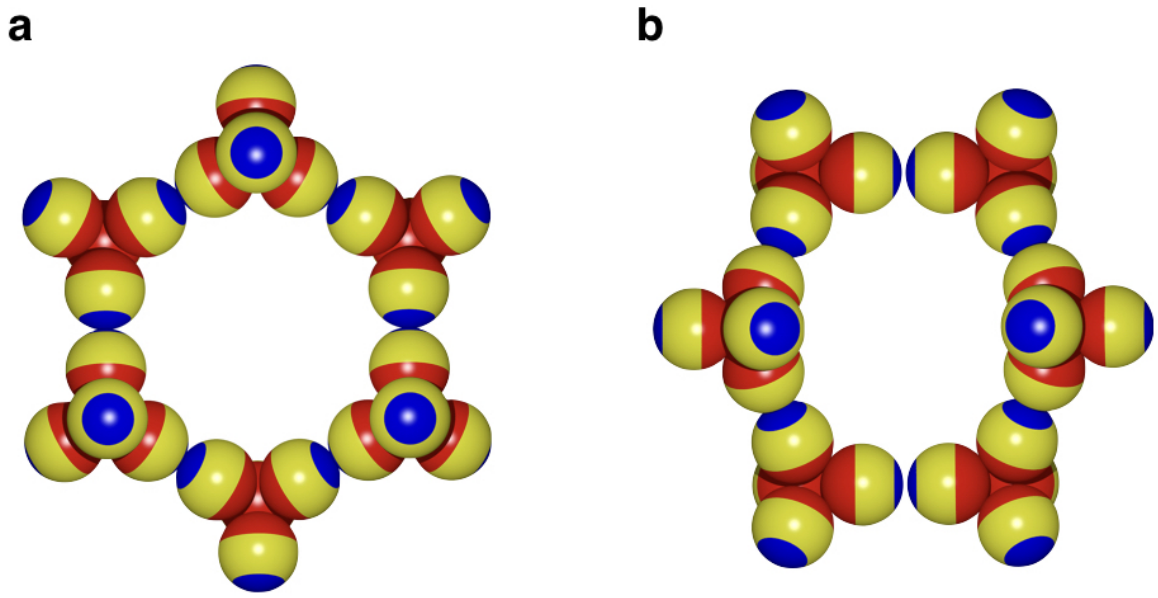

Figure 6.4: Two most stable structures for the 24-particle cluster of triblock patchy particles for the set of potentials parameters: $\epsilon_{AA} = 5$, $\epsilon_{BB} = 1$, $\alpha = 80°$, $\beta = 40°$, $\kappa = 100$, and $s = 5$. The ring-like structures are formed with tetrahedral subunits in 'chair' (**a.**) and 'boat' (**b.**) conformations.

dynamics (BD) simulations of $N = 500$ and $N = 864$ patchy particles respectively, in periodic systems at two different volume fractions, to unambiguously validate our hypothesis.

6.3.1 Diamond Cubic Colloidal Crystal

Figures 6.5 and **6.6** show the VMMC results for the first set of potential parameters at the volume fraction $\phi = 0.2$. Visual inspection revealed the formation of tetrahedral clusters via patch A - patch A interactions. We identified these tetrahedral clusters by means of a local order parameter q.[265] As $T^\star$ was gradually lowered, concomitant with the drop in the average potential energy per particle we observed a growth in the number of tetrahedral clusters N_{Td} as shown in **Figure 6.5a**. It is remarkable that the tetrahedral clusters were eventually formed in nearly 100% yield; such a self-limited assembly producing clusters of uniform size and shape is a crucial step for hierarchical self-assembly.[253] **Figure 6.5a** also shows that the average energy per particle, $V/(N\epsilon_{\mathrm{Y}})$, rather gradually decreases with the growth in N_{Td} through an intermediate range of values for $T^\star$ before showing a small discontinuity at lower values of $T^\star$. This discontinuous change was an indication for a structural transition taking place.

We calculated the pair distribution function, which is shown in **Figure 6.5b** at certain

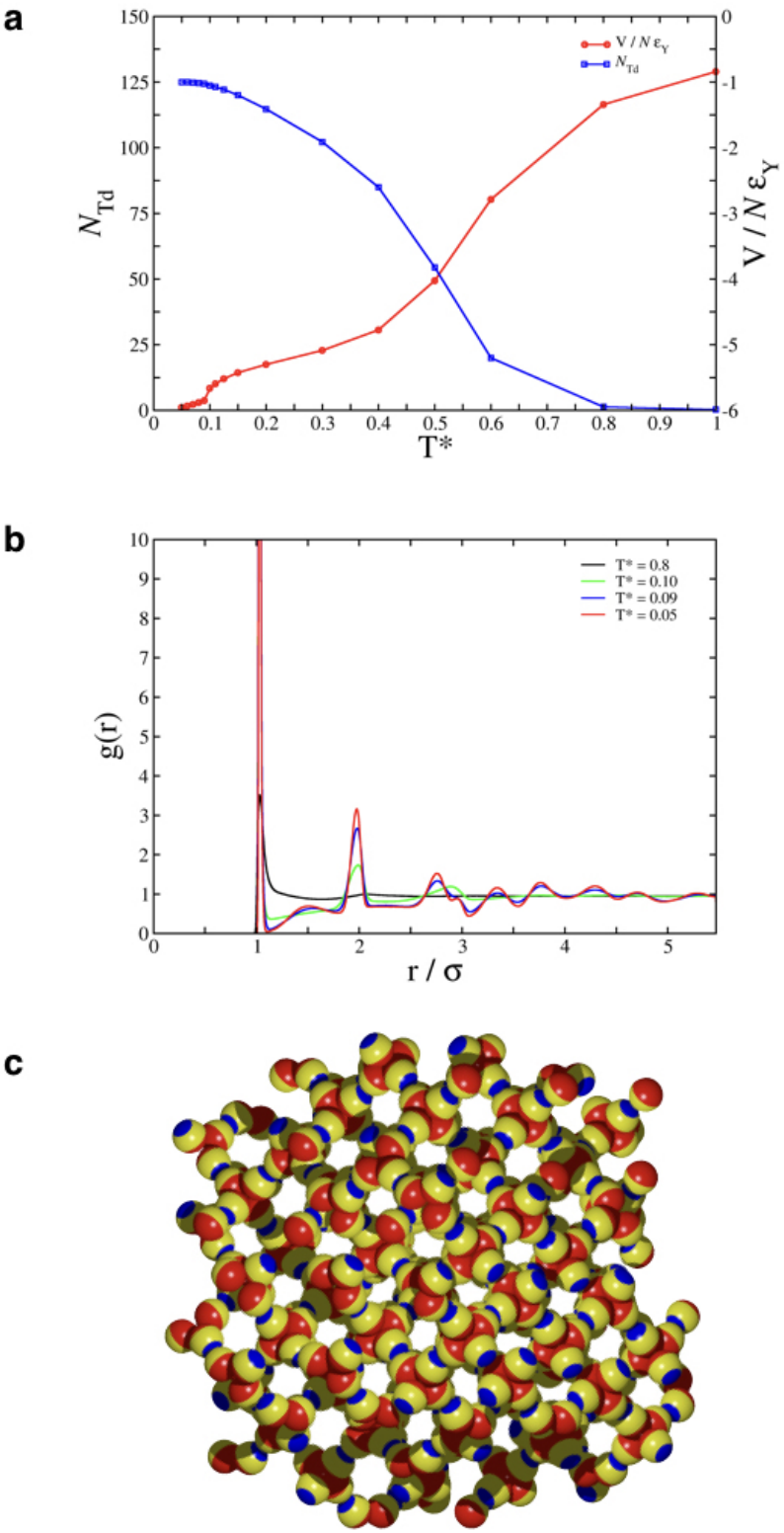

Figure 6.5: A two-level structural hierarchy emerging from the hierarchical self-assembly of patchy triblock colloidal particles. **a.** The average potential energy per particle and the number of tetrahedral clusters formed, shown on two different scales, as a function of the reduced temperature $T^{\star}$, for a 500-particle system at the volume fraction $\phi = 0.2$. **b.** The pair distribution function for the patchy particles at four different reduced temperatures. **c.** A snapshot of a typical configuration at $T^{\star} = 0.05$, illustrating a two-level structural hierarchy into a colloidal crystal via tetrahedra.

representative temperatures, in order to characterise this structural transition. At $T^\star = 0.09$, long-range correlations develop, indicating the emergence of a long-range order, which becomes more pronounced as $T^\star$ is further lowered. A snapshot of a typical configuration at $T^\star = 0.05$, shown in **Figure 6.5c**, reveals crystalline order, which is also evident in **Figure 6.6a**, where we use a reduced representation for clarity. In this reduced representation, we replace the tetrahedral clusters formed at the first level of assembly with spheres having four patches arranged tetrahedrally, their geometric centres coinciding and their orientations kept identical. The second level of assembly was driven by the weaker patch B - patch B interactions. The smaller patch width of patch B resulted in fewer "bonds" formed via these interactions; each patch B in fact formed only one bond with another patch B. Since the range of patch-patch interactions was taken to be identical for both patches A and B (**Figure 6.2**), the second level of assembly also resulted in a particularly pronounced first peak in the pair distribution function (**Figure 6.5b**), which continued to become stronger with the enhancement of the crystalline order below $T^\star = 0.09$.

In **Figure 6.6b**, we show the pair distribution function calculated with the geometric centres of the tetrahedral clusters, present in nearly 100% yield, at certain representative values of $T^\star$ along with the pair distribution function for a perfect cubic diamond lattice. **Figure 6.7** shows a perfect cubic diamond lattice, which can be viewed as a face-centred cubic lattice with half of its tetrahedral sites occupied, in our reduced representation. It is evident that the peaks are centred around those characteristic of a perfect cubic diamond crystal for an appropriately adjusted unit cell length. The probability distribution of the complex conjugate scalar product between the Steinhardt local bond order parameters of two neighbouring particles i and j, $\tilde{\boldsymbol{q}}_3(i) \cdot \tilde{\boldsymbol{q}}_3^\star(j)$, is shown in **Figure 6.6c**. The distribution with a peak around -1 is characteristic of a cubic diamond crystal as opposed to a hexagonal diamond crystal, which, in addition, has a characteristic peak around -0.115.[11]

The hierarchical self-assembly of a cubic diamond crystal is also observed when $T^\star$ is rapidly reduced in only two steps for VMMC simulations of $N = 500$, first to a value of $T^\star = 0.2$ and then to $T^\star = 0.09$, allowing for the two-level assembly to take place. Figure 6.8 shows the corresponding analysis for the rapidly cooled system. The pair distribution function, calculated with the geometric centres of tetrahedral centres for the rapidly cooled system (**Figure 6.8a**),

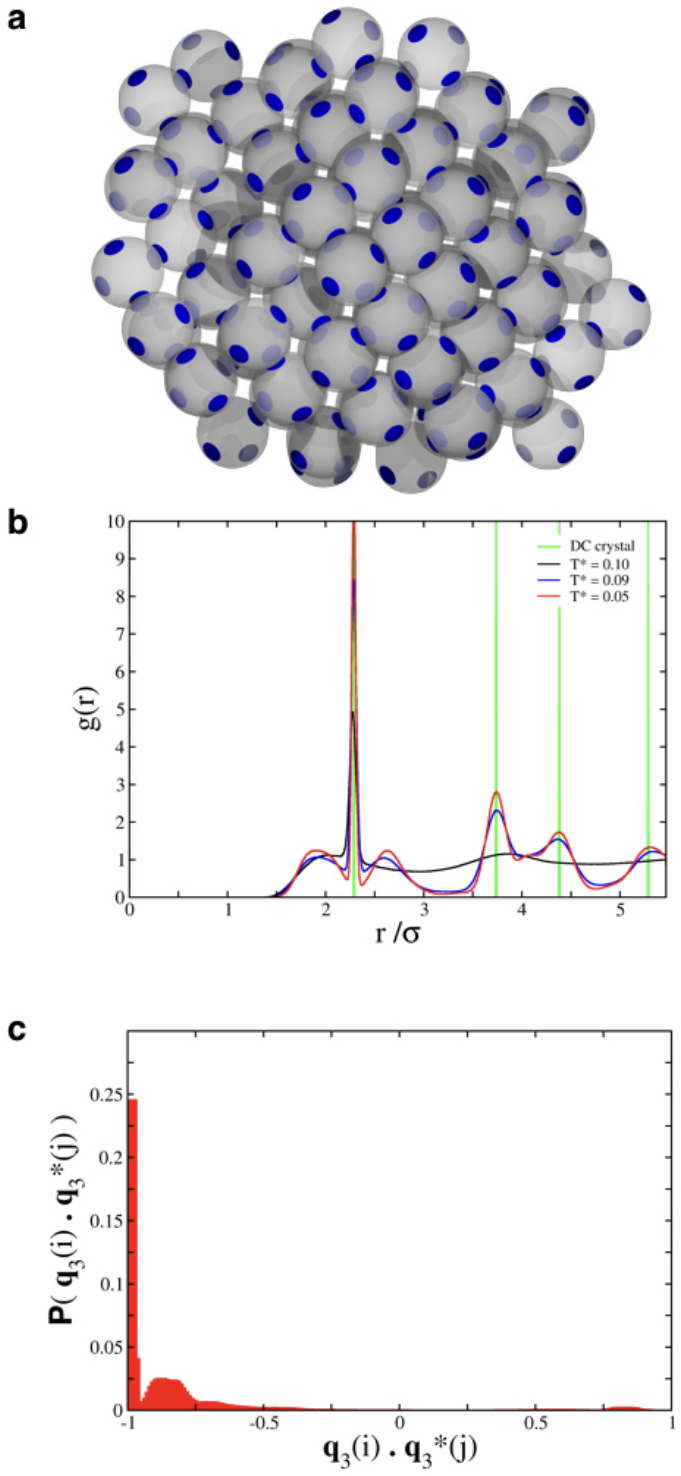

Figure 6.6: Hierarchical self-assembly of patchy triblock colloidal particles into a cubic diamond crystal via tetrahedral clusters. **a**. A snapshot of a typical configuration at $T^\star = 0.05$ in a reduced representation showing a cubic diamond crystal formed by tetrahedra. **b**. The pair distribution function for the geometric centres of the tetrahedral clusters for configurations at three different temperatures and for a configuration corresponding to a perfect cubic diamond crystal. **c**. The probability distribution of the complex conjugate scalar product between the local bond order parameters of two neighbouring particles i and j, $\tilde{\boldsymbol{q}}_3(i) \cdot \tilde{\boldsymbol{q}}_3^\star(j)$, for the configurations at $T^\star = 0.05$. A peak around -1 is a characteristic of a cubic diamond lattice.

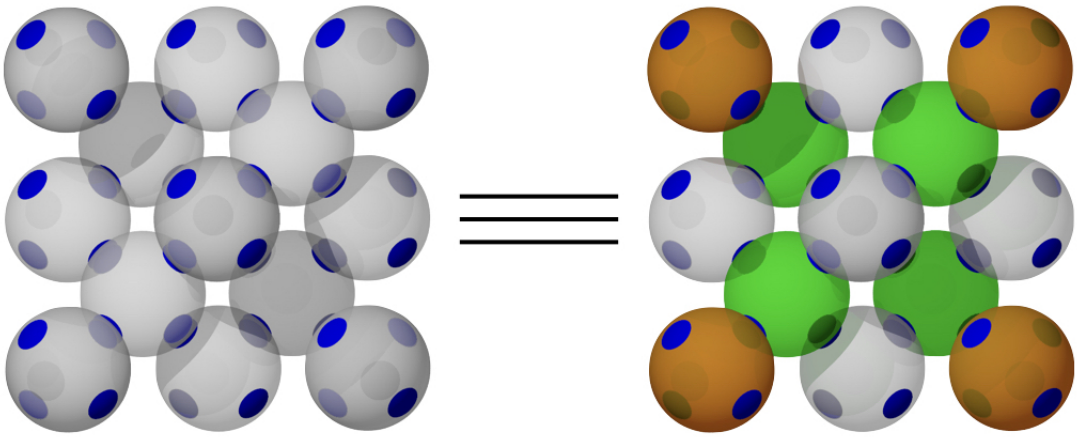

Figure 6.7: A perfect cubic diamond lattice formed by patchy particles, each with four patches in tetrahedral symmetry. On the right, the same structure is shown with colour-coding to highlight distinct sites: vertex sites (orange), face-centred sites (grey), and tetrahedral sites (green).

highlights the emergence of long-range correlations and long-range order as the temperature changes from $T^\star = 0.2$ to $T^\star = 0.09$. The emergence of long-range order is confirmed upon visual inspection of a typical configuration at $T^\star = 0.09$, **Figure 6.8c** and **d**, revealing crystalline order. The probability distribution of the complex conjugate of the Steinhardt bond order parameter, **Figure 6.8b**, also indicates that the colloidal crystal obtained upon rapid cooling exhibits cubic diamond structure. The success of this two-step temperature control protocol to induce the self-assembly of the cubic diamond crystal with a two-level structural hierarchy led us to exploit such a protocol to assess the robustness of the assembly behavior over the parameter space, which is rather large. Some systematic variation of the parameters around the this set of parameters in particular was undertaken because of special interest in bottom-up realization of a cubic diamond colloidal crystal. Given the span of the parameter space, this scan was not exhaustive. Our results, summarized in **Table 6.1**, nevertheless show that a reasonable spread of the parameter space supports the two-level self-assembly behavior into cubic diamond crystals via tetrahedral clusters.

Chen *et al.* suggest that the triblock patchy particles considered in their experimental work can nowadays be synthesized with high fidelity and monodispersity, including fairly precise control on the patch sizes.[97] The patch size was uniform within an uncertainty of less than 5° for the triblock patchy particles they synthesized.[97] We therefore considered Gaussian distributions for patch sizes, having mean values of 80° and 40° for patch A and patch B, respectively,

α	β	ϵ_{AA}	κ
60			
70	30		
75	35	2.5	50
80	40	5	100
85	45	7.5	200
90	50		

Table 6.1: A summary of systematic variation of the parameters undertaken in virtual-move Monte Carlo simulations following a two-step temperature-control protocol. One parameter was varied at a time with reference to the first set of parameter values, which appear in black along a row. The different values of a given parameter appear along a column and are color coded. The entries are in green if the formation of the cubic diamond crystal with a two-level structural hierarchy was observed in the simulations; the entries are in orange if the crystal formation was not observed but tetrahedral clusters were present in high yields ($> 90\%$); if even the tetrahedral clusters were not observed in sufficient yields, the entries are in red.

and each having a standard deviation of $5/3°$, in order to allow for some polydispersity. We followed the two-step temperature-quench protocol with polydispersity in both patches, keeping the remaining parameters of the first set identical. A rapid cooling protocol thus led to the emergence of crystalline order similar to what we observed for the monodisperse case, **Figure 6.9**. Our results therefore demonstrate that our bottom-up route to colloidal crystals with a two-level structural hierarchy self-assembled from triblock patchy particles shows some tolerance to polydispersity in the patch sizes comparable to the state-of-the-art fabrication.

In addition to VMMC simulations of $N = 500$ patchy triblock colloidal particles, BD simulations of $N = 864$ particles were also undertaken. It was important to carry out BD simulations in order to conclusively determine whether the dynamical pathways involve stagewise assembly. A pertinent question was whether a cluster-move algorithm such as VMMC biased the system here to form clusters in the first instance based on energetics, and thus favoured staged assembly. Although VMMC can be used to approximate real dynamics given an appropriate choice of parameters, here VMMC was implemented primarily for the enhanced sampling from equilibrium distribution, achieved through cluster moves.

Figure 6.10 shows the results for the BD simulations. **Figure 6.10a** shows the number of tetrahedra formed, and also compares the evolution of the average energy per particle $V/(N\epsilon_{\mathrm{Y}})$ for BD and VMMC simulations, as a function of $T^{\star}$. As previously stated, tetrahedral clusters were identified using the local order parameter q. Here, tetrahedral clusters were again formed in near 100% yield, crucial for hierarchical self-assembly. Furthermore, the correspondence of

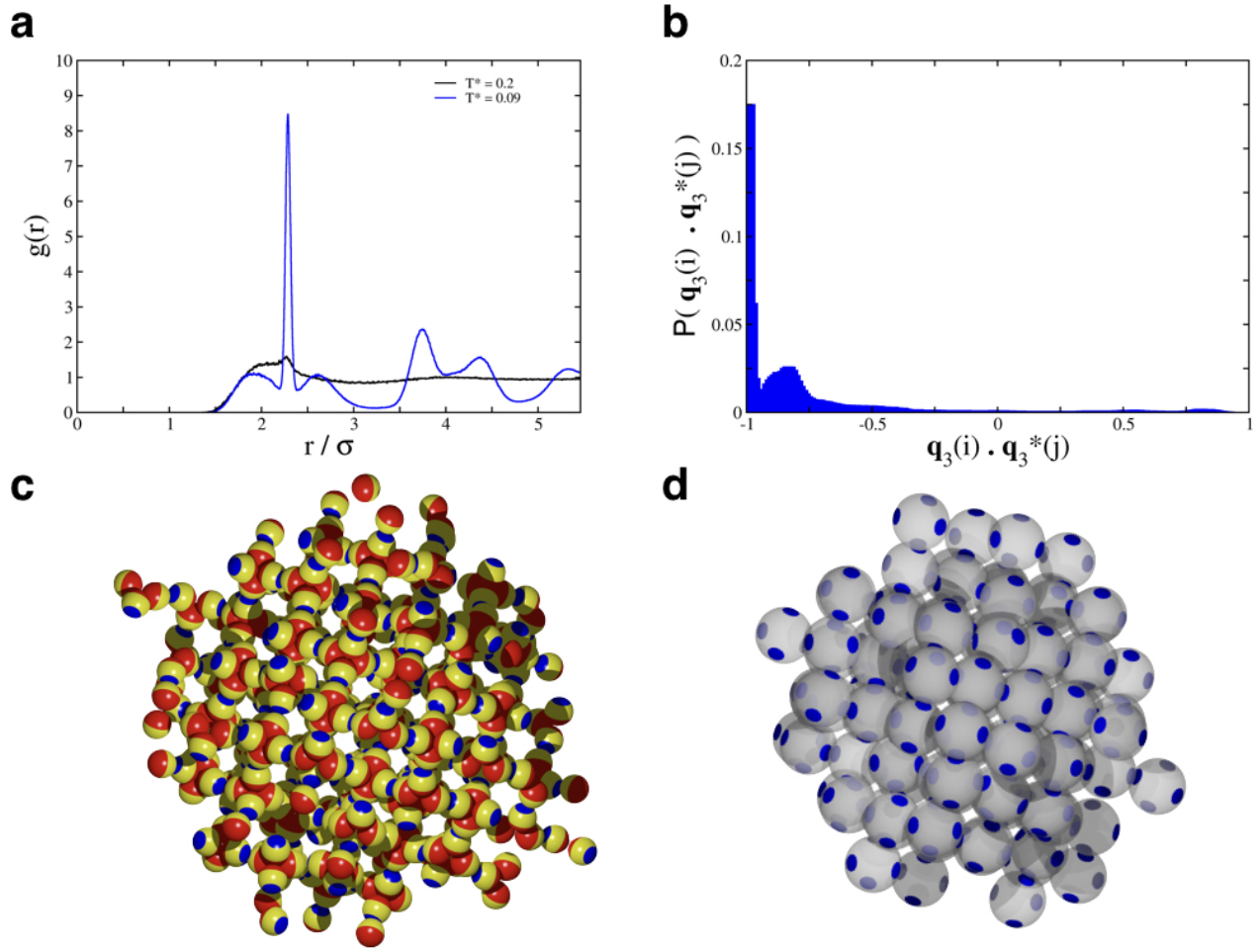

Figure 6.8: The hierarchical assembly of patchy triblock colloidal particles upon rapid cooling. **a**. The pair distribution function for the geometric centres of tetrahedral clusters at $T^\star = 0.2$ (black) and $T^\star = 0.09$ (blue). **b**. The probability distribution of the complex conjugate scalar product between the local bond order parameters of two neighbouring particles i and j, $\tilde{\boldsymbol{q}}_3(i) \cdot \tilde{\boldsymbol{q}}_3^\star(j)$ for the configurations at $T^\star = 0.09$. **c**. A snapshot of a typical configuration at $T^\star = 0.09$ demonstrating the two-level structural hierarchy achieved upon rapid cooling. **d**. The reduced representation of a typical snapshot at $T^\star = 0.09$ highlighting the cubic diamond nature of the colloidal crystal obtained.

the average energy per particle $V/(N\epsilon_{\mathrm{Y}})$ in both simulation methods, except at very low $T^\star$ values, is noteworthy confirming effective sampling at thermal equilibrium by both methods over most of the temperature range. A gradual decrease in the average per particle energy was observed for intermediate values of $T^\star$ along with a small discontinuity at lower values of $T^\star$ in the BD simulations. As with the VMMC simulations, the discontinuous change was an indicator for a structural change taking place. **Figure 6.10b** shows a snapshot of a typical configuration at $T^\star = 0.05$ for the BD simulations. Although not as ordered as that observed in VMMC simulations (**Figure 6.5c**), a degree of crystallinity within the $N = 864$ system can be discerned. This was confirmed upon calculation of the pair distribution function for

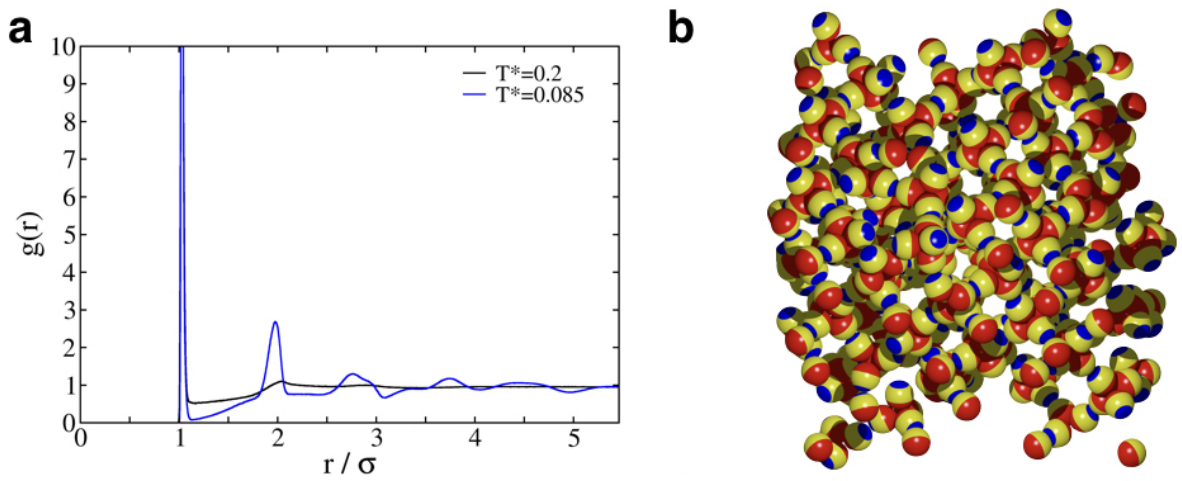

Figure 6.9: The two-level hierarchical self-assembly of triblock patchy particles into a colloidal cubic diamond crystal, observed in the presence of polydispersity in patch sizes when a two-step temperature control protocol was followed. **a.** The pair distribution function g(r) for the patchy particles at two different reduced temperatures, with allowance for polydispersity in both patch sizes. **b.** A snapshot of a typical configuration at $T^{\star} = 0.085$, illustrating a two-level structural hierarchy into a cubic diamond crystal via tetrahedra.

the geometric centres of the tetrahedral clusters, shown in **Figure 6.10c**. In **Figure 6.10c** the pair distribution function obtained from the BD simulations is also compared to that of the VMMC simulations. Here, the presence of long-range order for the structure formed in BD simulations is observed. In addition, the pair distribution function also demonstrates considerable overlap with that calculated for VMMC simulations and therefore exhibits peaks in positions characteristic of a diamond cubic lattice. Our BD simulations thus unequivocally demonstrate that the cubic diamond lattice was self-assembled from triblock patchy particles hierarchically.

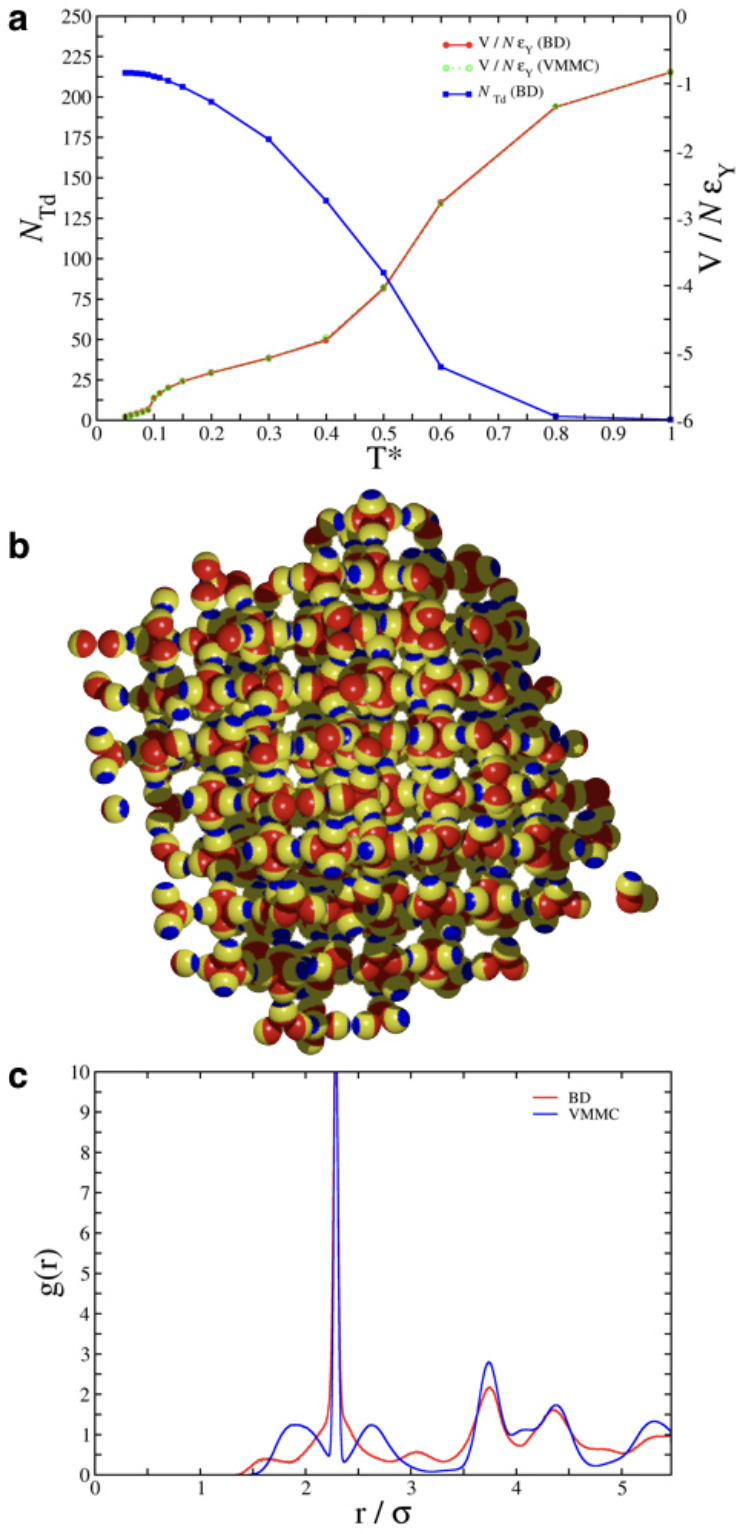

Figure 6.10: The two-level hierarchical self-assembly of patchy triblock particles observed in BD simulations. **a.** The average potential energy per particle and the number of tetrahedral clusters, on two different scales, as a function of the reduced temperature $T^\star$, for an 864-particle system at a volume fraction of $\phi = 0.2$. **b.** A snapshot of a typical configuration at $T^\star = 0.05$ for BD simulations, displaying two-level structural hierarchy. **c.** The pair distribution function for the geometric centres of tetrahedral clusters at $T^\star = 0.05$.

6.3.2 Body-Centred Cubic Colloidal Crystal

Here the results obtained for the second parameter set, when simulated under periodic boundary conditions at a volume fraction of $\phi = 0.3$, are presented. The earlier global optimisation runs identified, for this parameter set, the global minimum to consist of repeating octahedral units for the $N = 48$ cluster, as shown in **Figure 6.3**. **Figure 6.11a** shows that the average energy per particle gradually falls with the drop of $T^\star$ as the patchy particles form bonds via the stronger and wider patches, resulting in the formation of discrete octahedral clusters.We characterised the octahedral clusters by means of the local order parameter q.[266] The number of octahedral clusters in the system gradually grows and eventually the system effectively consists of octahedral clusters formed again in nearly 100% yield. The pair distribution function for the patchy particles reveals the emergence of long-range correlations at $T^\star = 0.2$, implying a second level of assembly of octahedral clusters via the interaction of the weaker and narrower patches (**Figure 6.11b**). This is confirmed by visual inspection. A typical low temperature configuration is shown in two different representations (**Figure 6.11c** and **Figure 6.12a**), which suggest that the octahedral clusters behave as the secondary building blocks for the second level of assembly.

We calculated the pair distribution function for the geometric centres of the octahedral clusters, present in nearly 100% yield, at low values of $T^\star$. In this analysis, we also observed an emergence of long-range correlations at $T^\star = 0.2$ (**Figure 6.12b**). At this value of $T^\star$, the peaks are centred around those characteristic of a perfect body-centred cubic (bcc) crystal for an appropriately adjusted unit cell length. This observation implies the formation of a bcc crystal by the octahedral clusters at the second level of assembly. This was confirmed by our analysis in terms of the local bond-orientational order parameters $\bar{q}_l(i)$ for $l = 4$ and 6. We considered the distribution of $\bar{q}_4$ and $\bar{q}_6$ calculated for individual centres of octahedral clusters.[263] The distribution, shown in Figure 6.12c, is consistent with that of a bcc crystal, providing confirmation to our analysis in terms of the pair distribution function for the geometric centres of the octahedral clusters. Given that the range of the patch-patch interactions is relatively longer in this case corresponding to a smaller value of the parameter s, such interactions are more likely to be realisable with nano-scale building blocks. It is of interest to note that nano-octahedra with short-range repulsive interactions were found to self-assemble into a

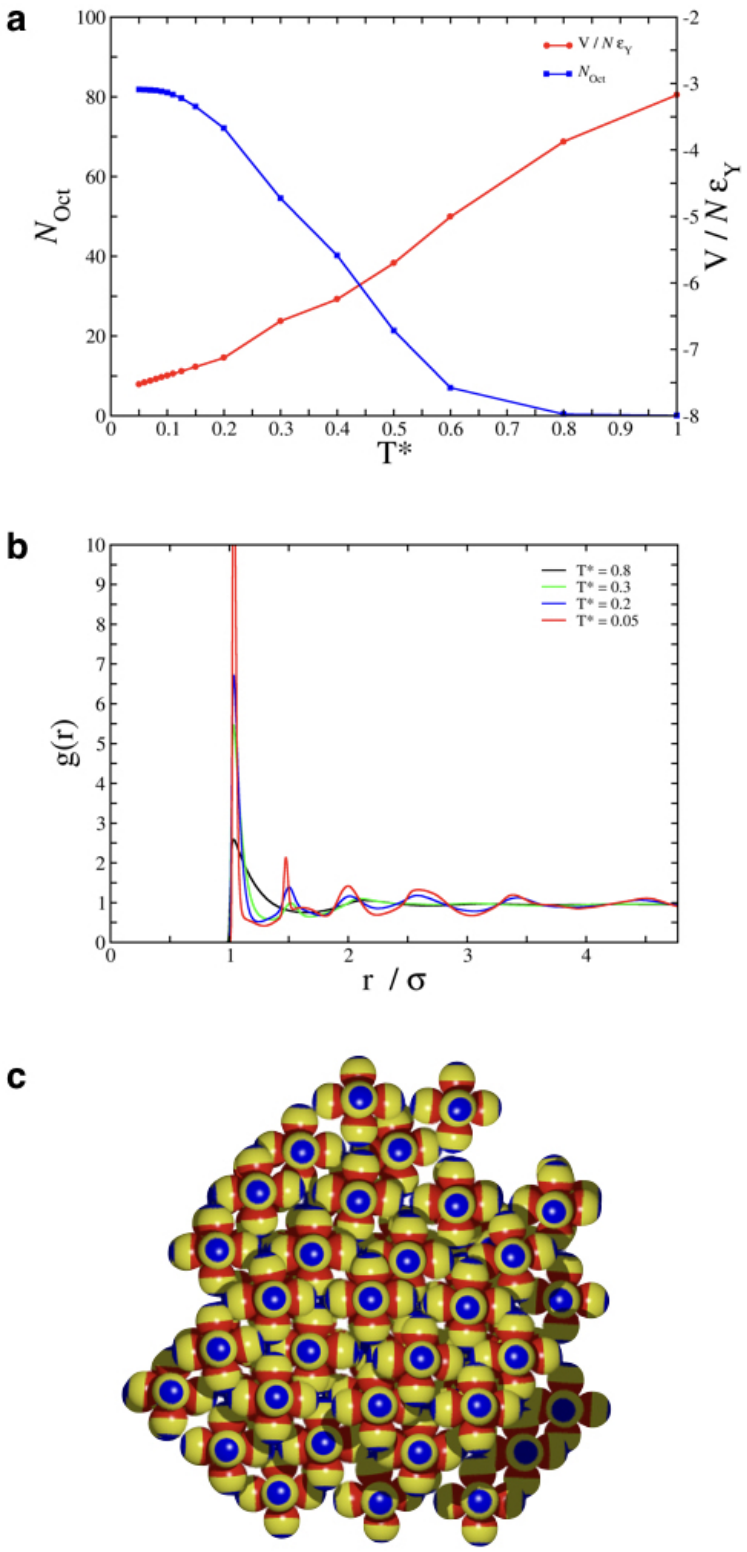

Figure 6.11: A two-level structural hierarchy emerging from the hierarchical self-assembly of patchy triblock colloidal particles. **a.** The average potential energy per particle and the number of octahedra formed, shown on two different scales, as a function of the reduced temperature $T^\star$ for a 500-particle system at the volume fraction $\phi = 0.3$. **b.** The pair distribution function for the patchy particles at four different reduced temperatures. **c.** A snapshot of a typical configuration at $T^\star = 0.05$, illustrating a two-level structural hierarchy into a colloidal crystal via octahedra.

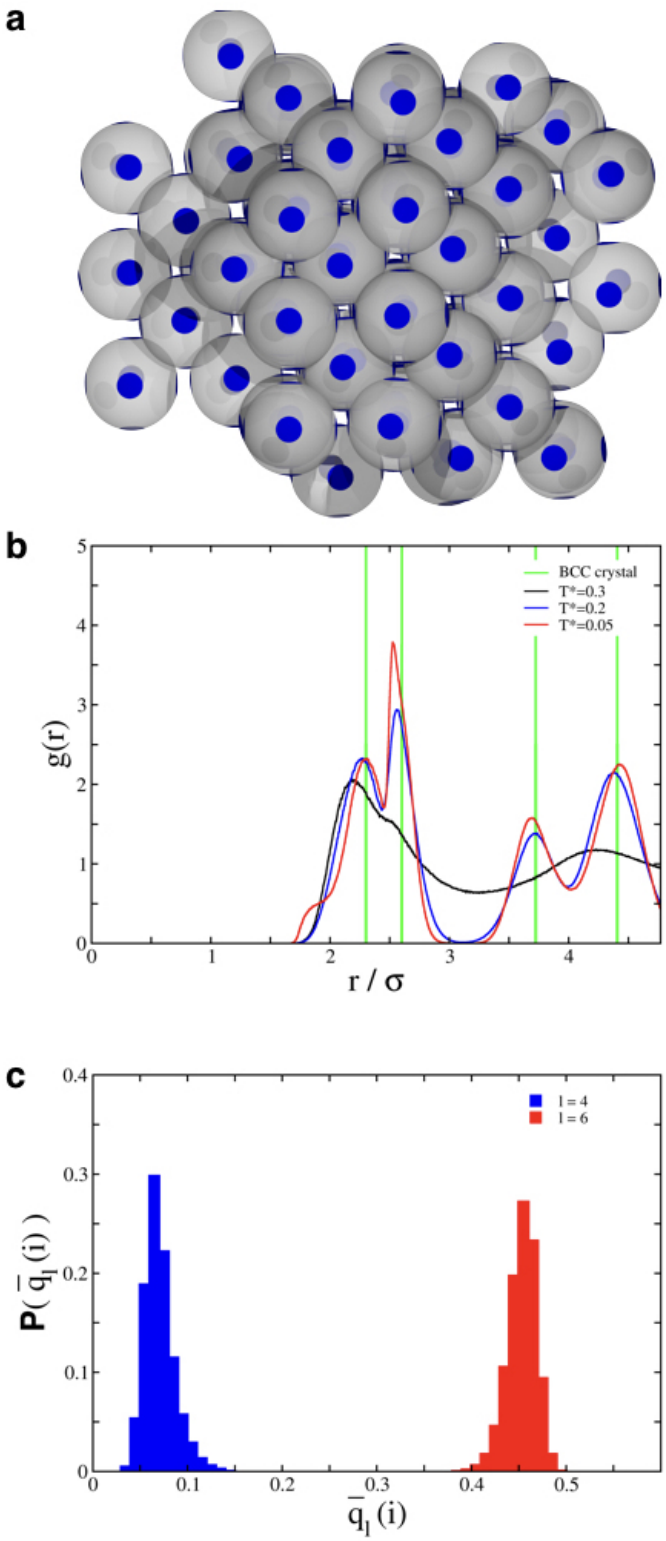

Figure 6.12: Hierarchical self-assembly of patchy triblock colloidal particles into a body-centred cubic crystal via octahedral clusters. **a**. A snapshot of a typical configuration at $T^\star = 0.05$ in a reduced representation showing a body-centred cubic crystal formed by octahedra. **b**. The pair distribution function for the geometric centres of the octahedral clusters for configurations at three different temperatures and for a configuration corresponding to a perfect body-centred cubic crystal. **c**. The probability distribution of the local bond-orientational order parameters $\bar{q}_l(i)$ for $l = 4$ and 6 for octahedral subunits for the configurations at $T^\star = 0.05$. The distributions are characteristics of a body-centred cubic lattice.

bcc crystal,[268] and so do nearly perfect octahedra obtained via truncation of hard tetrahedra at low densities.[269]

For the second stage of assembly to lead to the formation of a colloidal crystal, it is crucial that clusters of uniform size and shape are formed at the first level. In fact, we here considered the arrangements of the geometric centres of the polyhedral clusters in order to identify the crystal structures. Our simulations demonstrate that the width of the stronger patch is a critical parameter along with a hierarchy of interaction strengths to meet this objective. For example, a half-angle of 80° instead of 85° for the stronger patch width with $s = 1$ resulted in a mixture of tetrahedral and octahedral clusters in bulk simulations, prohibiting the second level of assembly into a colloidal crystal. However, the global optimisation runs for a finite-size system of $N = 48$ particles found the most stable structure to be consisting of only octahedral repeat units for the 80° case with $s = 1$. Our bulk simulations also reveal that the ratio $\epsilon_{AA}/\epsilon_{BB}$ is crucial for the second level of assembly. For $\epsilon_{AA} = 5$ and $\epsilon_{BB} = 2.5$, we did not observe any crystalline order at lower values of $T^\star$ for either of the two sets of model parameters; instead we observed disordered structures mostly with secondary building blocks. This observation is in line with findings previously reported,[97,235] and the proposed design rules for hierarchical self-assembly outlined here. A weaker interaction strength drives the second level of assembly efficiently via reversible bond formation, which allows the kinetic traps due to wrong contacts to be negotiated effectively.

Brownian dynamic simulations of $N = 864$ patchy triblock colloidal particles with patch widths $\alpha = 85°$, $\beta = 40°$ and $s = 1$ at the volume fraction $\phi = 0.3$ were also undertaken. Here, we sought to re-affirm the generality of the proposed design principles and further validate the hypothesised hierarchical self-assembly pathway predicted for this system. **Figure 6.13a** compares the evolution of the average per particle energy ($V/N\epsilon_{\mathrm{Y}}$) for both VMMC and BD simulations, clearly highlighting the close correspondence between the states of thermal equilibrium sampled by the two simulation methods, as $T^\star$ is lowered. A typical low temperature configuration, **Figure 6.13b**, demonstrates the hierarchical nature of the colloidal crystal ascertained via BD simulations. The octahedral clusters can be easily identified and seen to be acting as building blocks upon which the second level of hierarchical assembly, into the body-centred cubic structure, occurs. **Figure 6.13c** compares the pair distribution functions of the

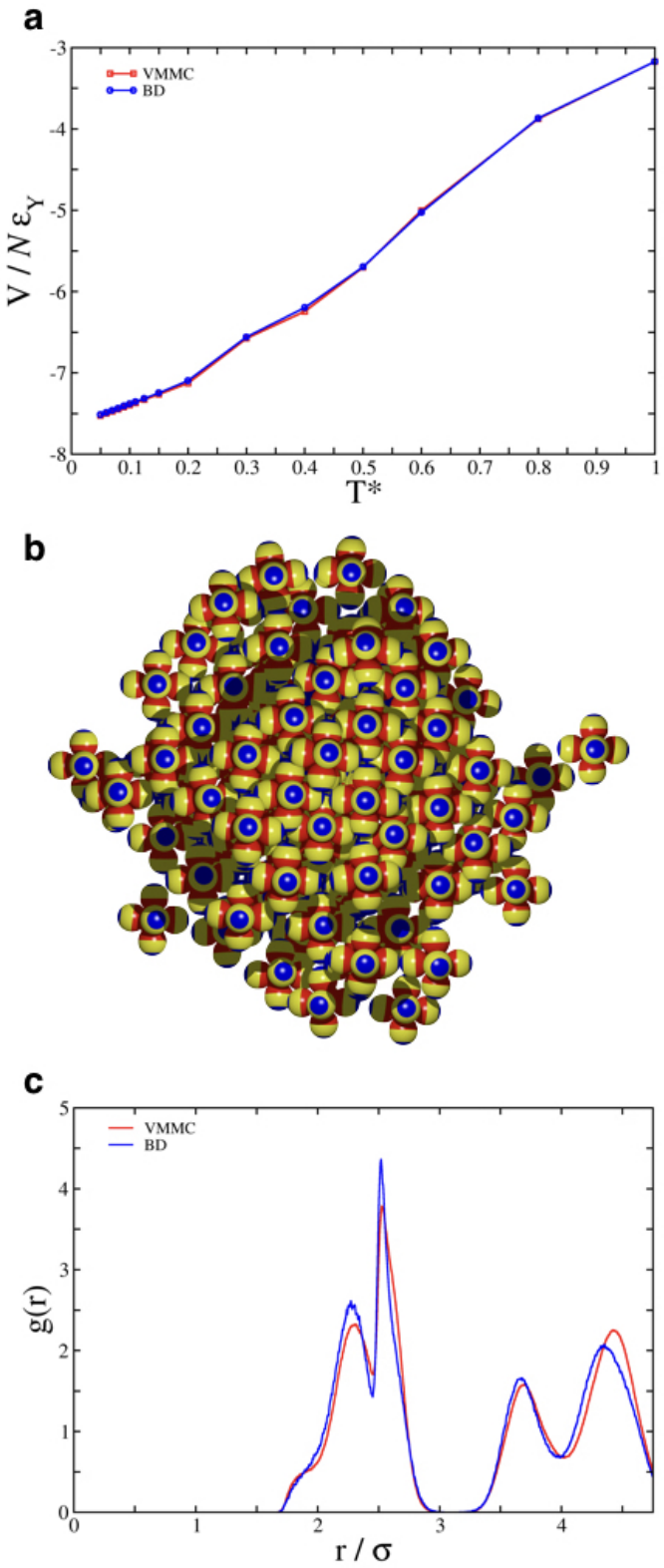

Figure 6.13: A comparison of the hierarchical self-assembly of patchy triblock colloidal particles into a body-centred cubic crystal as observed in VMMC and BD simulations. **a.** The evolution of the average energy per particle as a function of the reduced temperature $T^\star$, VMMC (red) and BD (blue). **b.** A typical configuration at $T^\star = 0.05$ taken from the BD simulation of $N = 864$ particles, demonstrating the hierarchical self-assembly of a colloidal crystal via octahedral clusters. **c.** The pair distribution functions for the geometric centres of the octahedral clusters for VMMC (red) and BD (blue) simulations at $T^\star = 0.05$.

geometric centres of octahedral clusters for both VMMC and BD simulations at a temperature of $T^\star = 0.05$. The strong overlap and characteristic peak positions of the pair distribution functions for between the VMMC and BD simulations confirms the body-centred cubic order.

6.3.3 Simple Cubic Colloidal Crystal

Here the results from Brownian dynamics simulations of the $N = 864$ system for the second set of parameters in a periodic cubic box at a volume fraction of $\phi = 0.2$ are presented. **Figure 6.14a** shows the average potential energy per particle and the number of discrete octahedral clusters formed as a function of the reduced temperature $T^\star$. The local order parameter q was used to identify octahedral clusters.[266] As before, octahedral clusters again form in near 100% yield. **Figure 6.14b** presents the pair distribution function for the triblock patchy particles at certain representative temperatures, highlighting the emergence of long-range correlations at a reduced temperature of $T^\star = 0.15$. The long-range correlations are suggestive of a second level of assembly of the octahedral clusters driven by the interactions between the weaker narrow patches. This was confirmed upon visual inspection. **Figure 6.14c** shows a typical low-temperature configuration for $N = 864$ system of triblock patchy particles at $T^\star = 0.05$.

The pair distribution function for the geometric centres of the octahedral clusters, present in near 100% yield at low temperatures, is shown for three temperatures in **Figure 6.14d**. The emergence of long-range correlations is again observed at a reduced temperature of $T^\star = 0.15$. **Figure 6.14d** also shows the characteristic peak positions for a simple cubic crystal with an appropriately adjusted cell length. It is evident that the peaks of the pair distribution function for the geometric centres closely correspond to those characteristic of a perfect simple cubic crystal. The prominent shoulder present on the first peak of the pair distribution plot of **Figure 6.14d** can be easily explained in conjunction with the low configuration snapshot (**Figure 6.14c**). In **Figure 6.14c** it is clear that some octahedral units sit within the voids of the simple cubic lattice. This is due to the volume fraction of $\phi = 0.2$ being too high to form the 'perfect' simple cubic crystal. The presence of octahedral units within these voids of the simple cubic lattice produces the shoulder observed on the first peak of the pair distribution function (**Figure 6.14d**). A body-centred cubic crystal can be seen as two interpenetrating simple cubic lattices. Having observed the hierarchical self-assembly of a body-centred cubic

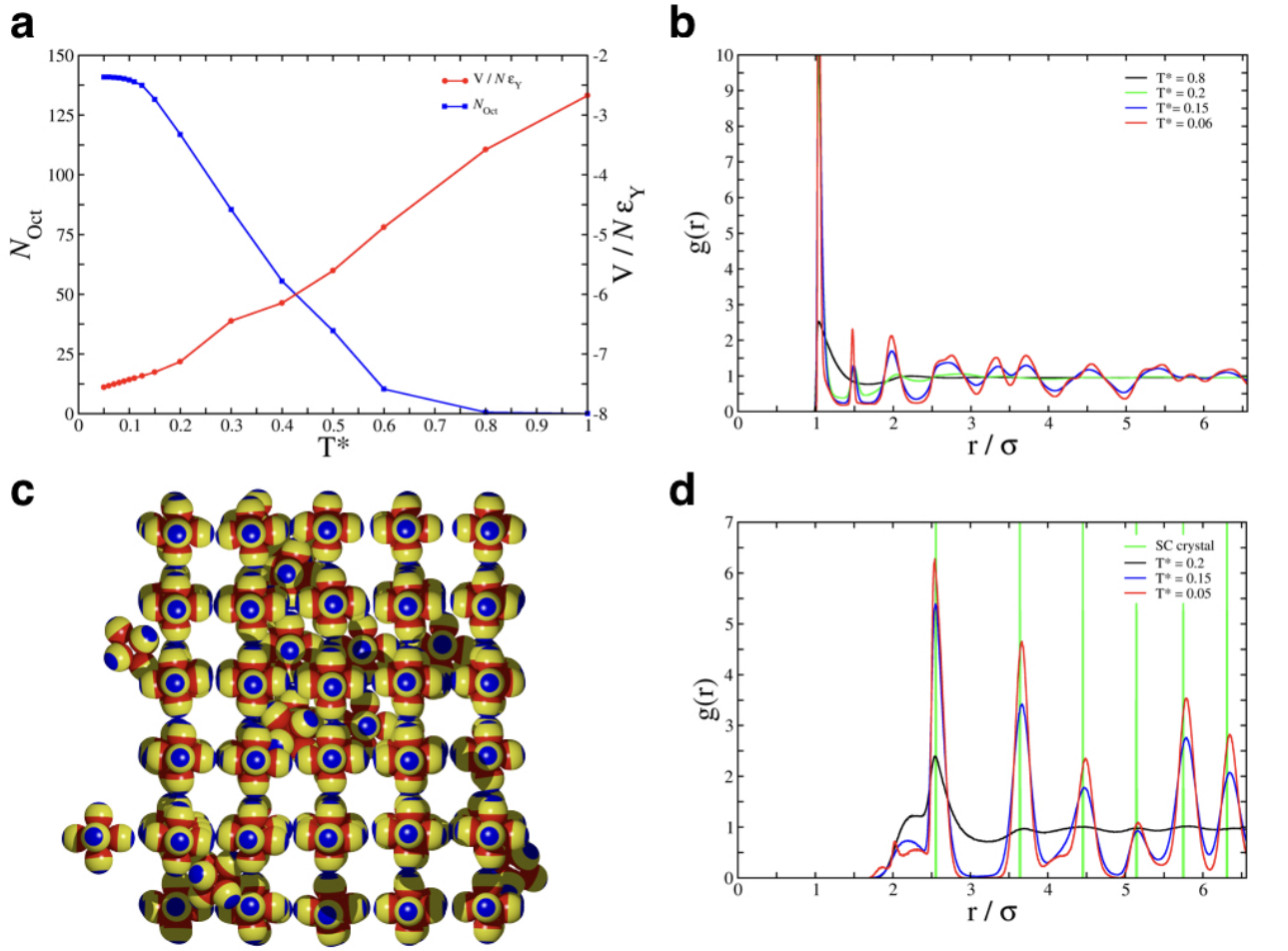

Figure 6.14: A two level structural hierarchy emerging from the hierarchical self-assembly of patch triblock particles. **a.** The average potential energy per particle and the number of octahedral clusters formed, shown on two different scales, as a function of the reduced temperature $T^{\star}$, for a 864-particle system at the volume fraction $\phi = 0.2$. **b.** The pair distribution function for patchy particles at four different reduced temperatures. **c.** A snapshot of a typical configuration at $T^{\star} = 0.05$, exhibiting a two-level structural hierarchy into a colloidal crystal via octahedra. **d.** The pair distribution function for the geometric centres of the octahedral clusters for configurations at three different temperatures and for a configuration corresponding to a perfect simple cubic crystal.

crystal via octahedral clusters at $\phi = 0.3$, it is therefore reasonable to observe the self-assembly of a simple cubic colloidal crystal for a lower value of ϕ.[258]

Here, we have demonstrated the hierarchical self-assembly of triblock patchy particles into three distinct colloidal crystals, namely cubic diamond, body-centred cubic and simple cubic crystals, using our model. All of these crystals have been self-assembled in two stages, the first stage giving rise to clusters of uniform size and shape, which serve as the building blocks for the next stage of assembly into respective crystals. The patch width α of the stronger patch and the range of the patch-patch interaction governed by the parameter s are crucial to determine the shape and size of the clusters. The patch width β of the weaker patch determines how

these clusters coordinate through the next stage of assembly. While these model parameters are especially critical to determine the morphology of the crystals with two-level structural hierarchy, the open crystals formed also depend on the volume fraction ϕ, as it effects both the bonding probability at a given $T^\star$, and the ability of the system to form interpenetrating networks,[258] as observed here with formation of the body centred cubic and simple cubic crystals at different volume fractions.

6.4 Conclusion

In summary, we have demonstrated the feasibility of programming hierarchical self-assembly of colloidal building blocks with a generic design rule that prescribes the use of a hierarchy of interaction strengths. Such a generic design rule for hierarchical self-assembly can be exploited to fabricate colloidal superstructures of unprecedented complexity. In particular, we exploited the design principle, realised with triblock patchy particles that closely resemble those synthesised recently,[97] to show hierarchical self-assembly into a cubic diamond colloidal crystal, a body-centred cubic and simple cubic colloidal crystal via tetrahedral and octahedral clusters, respectively. The use of colloidal building blocks with only two patches to form a cubic diamond colloidal crystal via a hierarchical self-assembly scheme makes it a novel yet promising route for the experimental realisation of photonic crystals with a band gap in the visible region in the foreseeable future. This route relaxes the stringent requirement on the fidelity of particle synthesis associated with the fabrication of precisely tetrahedral patches.[93]

Chapter 7

Conclusions

7.1 Summary

The primary goal of this thesis has been to design anisotropic colloidal building blocks *in silico* to encode hierarchical self-assembly. The key to this multiscale design problem is to improve our understanding of the multitude of colloidal interactions at play often in the presence of more than one anisotropy attribute. Such understanding is crucial to programme colloidal self-assembly into a target structure that is not only thermodynamically favourable but also kinetically accessible. This task is even more challenging in the context of hierarchical self-assembly, given multiple time- and length-scales involved therein. A radical improvement in the ability to synthesise complex colloidal particles in recent years has brought about a paradigm shift in the field of colloidal self-assembly, setting a platform for ambitious goals for bottom-up fabrication of novel materials. The studies undertaken in this thesis are thus of topical interest, from the perspective of both fundamentals and applications.

This thesis presents a body of work, which employed a variety of computational techniques to address the challenges that programming hierarchical self-assembly for colloidal building blocks faces. A close connection with contemporary experimental research was maintained throughout. **Chapter 3** and **Chapter 4** report, based on global optimisation and Monte Carlo studies, the self-assembly of designer charge-stabilised colloidal magnetic particles into a number of supracolloidal polyhedra for size-selected clusters. These polyhedra each display a remarkable two-level structural hierarchy. The design space was found to support self-assembled polyhedra, which are of very different morphologies, namely hollow spheroidal and tubular

structures, involving the formation of subunits of three-fold and four-fold rotational symmetry, respectively. In pursuit of hollow spheroidal structures in particular, inspiration was drawn from viral capsids, which show spectacular examples of structural hierarchy. The charge-stabilised colloidal magnetic particles considered here closely resemble those synthesised by Sacanna *et al.* using an iron oxide inclusion buried beneath the surface of an organo-silica polymer sphere.[176] Upon controlling salt concentration in the medium, these particles were shown to readily self-assemble into triangular motifs.[176] The particles were occasionally found to form square-planar motifs as well.

In **Chapter 4**, the dominant pathways for self-assembly into these polyhedra were also characterised using the discrete path sampling method. The pathways revealed two distinct mechanisms – a staged or hierarchical pathway for a hollow spheroidal polyhedron and a growth mechanism via sequential attachment of the subunits for a tubular structure. It is likely that the structural features of the distinct morphologies play some role in determining the self-assembly mechanisms. The hollow tubular structure can in principle be formed from any number of tetramer units and therefore growth can continue in a sequential manner uninhibited. However, the hollow spheroidal structures can only form from specific numbers of triangular units. A staged pathway in which the required number of triangular units are formed first thus appears to be more conducive.

Chapter 5 examines the kinetic accessibility of a number of hollow spheroidal structures as a design parameter is varied. To this end, the study used a number of computational methods, namely basin-hopping global optimisation, standard and advanced Monte Carlo techniques, and umbrella sampling technique. For a staged assembly pathway, the structure, which derived the strongest energetic stability from the first stage of assembly and the weakest from the second stage, was found to be most kinetically accessible. It was anticipated that such an optimal design principle would have general implications for programming hierarchical self-assembly schemes for micro- and nanoparticles.

Building on these findings, we introduce a generic design principle that exploits a hierarchy of interaction strengths and employ this design principle in computer simulations, using virtual-move Monte Carlo technique and Brownian Dynamics method for periodic systems. Our simulations demonstrate the hierarchical self-assembly of triblock patchy colloidal particles into a

variety of colloidal crystals via distinct small clusters of uniform size and shape, the so-called "colloidal molecule". The ability to form the clusters in the self-limited way is critical to the success of this design principle. Such a conceptual design framework opens up the prospects of reliably encoding hierarchical self-assembly of colloidal particles into an unprecedented level of sophistication. Moreover, the design framework underpins a novel bottom-up route to cubic diamond colloidal crystals, which have remained elusive despite being much sought after for their attractive photonic applications.

7.2 Outlook

In this thesis, two distinct model systems, namely charge-stabilised colloidal magnetic particles with a shifted dipole and triblock patchy particles, are studied to programme structural hierarchy via small colloidal clusters. Such clusters mimic the symmetry of molecular structures, and are often referred to as "colloidal molecules". It is important to recognise that both of these model systems, which drew motivation from recently synthesised colloidal particles,[176,237] involve some form of *patchiness*. The charged-stabilised colloidal magnetic particles considered here can be viewed to have *magnetic patches*, as per the description of Sacanna *et al.* In contrast, our triblock patchy particles have the conventional *chemical patches* due to heterogeneous surface chemistry. In this context, a pertinent question is whether patchiness is essential for hierarchical self-assembly via *colloidal molecules*. This question calls for further investigation. A plausible route to structural hierarchy in the absence of patchiness could be via shape anisotropy.

It will be of interest to study the charge-stabilised colloidal magnetic particles under periodic boundary conditions to investigate the bulk behaviour. Here a relevant question is whether or not the bulk phase is comprised of discrete hollow spheroidal structures. The software *PaSSion* developed in-house can be extended to carry out VMMC simulations. Such simulations will, however, require an appropriate treatment of long-ranged dipolar interactions. Alternatively, one could also consider performing Brownian Dynamics simulations. The dynamical simulations will be rather involved, necessitating a quaternion based Brownian dynamics algorithm and the calculations of forces and torques for spherical particles with magnetic dipoles shifted away from the centre.

VMMC simulations conducted in the NPT ensemble would be particularly useful, leading to the identification of the ideal packing fractions for crystal formation.

An exciting line of inquiry concerns the characterisation of the dynamical pathways to the colloidal crystals self-assembled from triblock patchy particles via colloidal molecules, reported in **Chapter 6** based on Brownian dynamics simulations. The Brownian dynamics trajectories unequivocally demonstrates that the pathways are hierarchical, i.e. proceeds stage-wise via the formation of colloidal molecules at the first stage. However, fundamental questions in regard to these pathways remain; the answers to these questions will be crucial to control the kinetic of crystallisation. It is likely that a "nucleation and growth" mechanism is operational here. Determining whether the nucleation phenomena observed align with the existing qualitative picture of nucleation provided by classical nucleation theory (CNT), or perhaps relates to scenarios beyond CNT, would be of great interest.[231]

Given the directional nature of the patch-patch interactions, evidence supporting the theory of "oriented attachment" for crystal growth could be a possible scenario.[270]

Understanding the dynamical pathways will be crucial to achieving better control over crystallisation.

While the computational studies presented in this thesis were conducted in close connection with experimental research, idealised monodisperse systems were studied. For the complex colloidal particles considered here, the origin of polydispersity is not restricted to size distribution only. In view of this scenario, it will be of interest to assess in future studies the robustness of the designed self-assembly schemes with respect to polydispersity, at least in the most crucial parameters.

Finally, the body of work presented in thesis reports on progress made in the context of programming colloidal self-assembly to realise two-level structural hierarchy via *colloidal molecules*. The quest for bottom-up routes to multi-level structural hierarchies continues.

Bibliography

[1] V. J. Anderson and H. N. W. Lekkerkerker, *Nature*, 2002, **416**, 811–815.

[2] W. Poon, *Science*, 2004, **304**, 830–831.

[3] S. C. Glotzer and M. J. Solomon, *Nat. Mater.*, 2007, **6**, 557–562.

[4] S.-M. Yang, S.-H. Kim, J.-M. Lim and G.-R. Yi, *J. Mater. Chem.*, 2008, **18**, 2177–2190.

[5] A. B. Pawar and I. Kretzschmar, *Macromol. Rapid Commun.*, 2010, **31**, 150–168.

[6] F. Li, D. P. Josephson and A. Stein, *Angew. Chem. Int. Ed.*, 2011, **50**, 360–388.

[7] S. Sacanna and D. J. Pine, *Curr. Opin. Colloid. Interface Sci.*, 2011, **16**, 96–105.

[8] W. B. Rogers, W. M. Shih and V. N. Manoharan, *Nat. Rev. Mater.*, 2016, **1**, 364–368.

[9] G. M. Whitesides and B. Grzybowski, *Science*, 2002, **295**, 2418.

[10] Z. Zhang, A. S. Keys, T. Chen and S. C. Glotzer, *Langmuir*, 2005, **21**, 409–413.

[11] F. Romano, E. Sanz and F. Sciortino, *J. Chem. Phys.*, 2011, **134**, 174502.

[12] É. Ducrot, M. He, G.-R. Yi and D. J. Pine, *Nat. Mater.*, 2017.

[13] J.-G. Park, S.-H. Kim, S. Magkiriadou, T. M. Choi, Y.-S. Kim and V. N. Manoharan, *Agnew. Chem. Int. Ed.*, 2014, **53**, 2899 –2903.

[14] W. Liu, M. Tagawa, H. L. Xin, T. Wang, H. Emamy, H. Li, K. G. Yager, F. W. Starr, A. V. Tkachenko and O. Gang, *Science*, 2016, **351**, 582–586.

[15] A. van Blaaderen, *Science*, 2003, **301**, 470–471.

[16] V. N. Manoharan, *Science*, 2015, **349**, 1253751.

[17] Y. A. Urzhumov, G. Shvets, J. Fan, F. Capasso, D. Brandl and P. Nordlander, *Opt. Express*, 2007, **15**, 14129–14145.

[18] A. Alù and N. Engheta, *Opt. Express*, 2009, **17**, 5723–5730.

[19] J. A. Fan, C. Wu, K. Bao, J. Bao, R. Bardhan, N. J. Halas, V. N. Manoharan, P. Nordlander, G. Shvets and F. Capasso, *Science*, 2010, **328**, 1135–1138.

[20] S. N. Sheikholeslami, H. Alaeian, A. L. Koh and J. A. Dionne, *Nano Lett.*, 2013, **13**, 4137–4141.

[21] N. B. Schade, M. C. Holmes-Cerfon, E. R. Chen, D. Aronzon, J. A. Fan, F. Capasso and V. N. Manoharan, *Phys. Rev. Lett.*, 2013, **110**, 148303.

[22] L. Cademartiri and K. J. M. Bishop, *Nat Mater*, 2015, **14**, 2–9.

[23] V. N. Manoharan, M. T. Elsesser and D. J. Pine, *Science*, 2003, **301**, 483–487.

[24] D. J. Wales and J. P. K. Doye, *J. Phys. Chem. A*, 1997, **111**, 5111–5116.

[25] A. I. Campbell, V. J. Anderson, J. S. Van Duijneveldt and P. Bartlett, *Phys. Rev. Lett.*, 2005, **94**, 1–5.

[26] F. Sciortino, P. Tartaglia and E. Zaccarelli, *J. Phys. Chem. B*, 2005, **109**, 21942–21953.

[27] A. Malins, S. R. Williams, J. Eggers, H. Tanaka and C. P. Royall, *J. Phys. Condens. Matter*, 2009, **21**, 425103.

[28] G. Meng, N. Arkus, M. P. Brenner and V. N. Manoharan, *Science*, 2010, **327**, 560–563.

[29] C. L. Klix, K. Murata, H. Tanaka, S. R. Williams, A. Malins and C. P. Royall, *Sci. Rep.*, 2013, **3**, 2072.

[30] D. J. Wales, *ChemPhysChem*, 2010, **11**, 2491–2494.

[31] R. W. Perry, M. C. Holmes-Cerfon, M. P. Brenner and V. N. Manoharan, *Phys. Rev. Lett.*, 2015, **114**, 1–5.

[32] D. J. Kraft, W. S. Vlug, C. M. Van Kats, A. Van Blaaderen, A. Imhof and W. K. Kegel, *J. Am. Chem. Soc.*, 2009, **131**, 1182–1186.

[33] Y. Wang, D. R. Breed, V. N. Manoharan, L. Feng, A. D. Hollingsworth, M. Weck and D. J. Pine, *Nature*, 2012, **491**, 51–56.

[34] N. Arkus, V. N. Manoharan and M. P. Brenner, *Phys. Rev. Lett.*, 2009, **103**, 118303.

[35] F. Calvo, J. P. K. Doye and D. J. Wales, *Nanoscale*, 2012, **4**, 1085.

[36] J. W. R. Morgan and D. J. Wales, *Nanoscale*, 2014, **6**, 10717–10726.

[37] D. J. Kraft, J. Groenewold and W. K. Kegel, *Soft Matter*, 2009, **5**, 3823.

[38] A. Perro, E. Duguet, O. Lambert, J. C. Taveau, E. Bourgeat-Lami and S. Ravaine, *Angew. Chemie - Int. Ed.*, 2009, **48**, 361–365.

[39] F. Ma, D. T. Wu and N. Wu, *J. Am. Chem. Soc.*, 2013, **135**, 7839–7842.

[40] A. Desert, C. Hubert, Z. Fu, L. Moulet, J. Majimel, P. Barboteau, A. Thill, M. Lansalot, E. Bourgeat-Lami, E. Duguet and S. Ravaine, *Angew. Chemie - Int. Ed.*, 2013, **52**, 11068–11072.

[41] T. S. Skelhon, Y. Chen and S. a. F. Bon, *Soft Matter*, 2014, **10**, 7730–7735.

[42] C. A. Silvera Batista, R. G. Larson and N. A. Kotov, *Science*, 2015, **350**, 1242477.

[43] C. L. Phillips, E. Jankowski, B. J. Krishnatreya, K. V. Edmond, S. Sacanna, D. G. Grier, D. J. Pine and S. C. Glotzer, *Soft Matter*, 2014, **10**, 7468–7479.

[44] M. E. Leunissen, R. Dreyfus, R. Sha, T. Wang, N. C. Seeman, D. J. Pine and P. M. Chaikin, *Soft Matter*, 2009, **5**, 2422.

[45] Z. Zeravcic and M. P. Brenner, *Proc. Natl. Acad. Sci.*, 2014, **111**, 1748–1753.

[46] H. Tanaka, Z. Zeravcic and M. P. Brenner, *Phys. Rev. Lett.*, 2016, **117**, 1–5.

[47] Z. Zeravcic and M. P. Brenner, *Proc. Natl. Acad. Sci.*, 2017, **114**, 4342–4347.

[48] S. Granick, S. Jiang and Q. Chen, *Phys. Today*, 2009, **62**, 68–69.

[49] L. Hong, A. Cacciuto, E. Luijten and S. Granick, *Langmuir*, 2008, **24**, 621–625.

[50] D. J. Kraft, R. Ni, F. Smallenburg, M. Hermes, K. Yoon, D. A. Weitz, A. van Blaaderen, J. Groenewold, M. Dijkstra and W. K. Kegel, *Proc. Natl. Acad. Sci. USA*, 2012, **109**, 10787–10792.

[51] F. Sciortino, A. Giacometti and G. Pastore, *Phys. Rev. Lett.*, 2009, **103**, 1–4.

[52] F. Sciortino, A. Giacometti and G. Pastore, *Phys. Chem. Chem. Phys.*, 2010, **12**, 11869.

[53] N. Kern and D. Frenkel, *J. Chem. Phys.*, 2003, **118**, 9882–9889.

[54] G. Munaò, P. O'Toole, T. S. Hudson, D. Costa, C. Caccamo, F. Sciortino and A. Giacometti, *J. Phys. Condens. Matter*, 2015, **27**, 234101.

[55] D. Zerrouki, J. Baudry, D. Pine, P. Chaikin and J. Bibette, *Nature*, 2008, **455**, 380–382.

[56] D. Chakrabarti, S. N. Fejer and D. J. Wales, *Proc. Natl. Acad. Sci. USA*, 2009, **106**, 20164–20167.

[57] D. Chakrabarti and D. J. Wales, *Soft Matter*, 2011, **7**, 2325.

[58] Q. Chen, J. K. Whitmer, S. Jiang, S. C. Bae, E. Luijten and S. Granick, *Science*, 2011, **331**, 199–202.

[59] J. W. R. Morgan, D. Chakrabarti, N. Dorsaz and D. J. Wales, *ACS Nano*, 2013, **7**, 1246–1256.

[60] S. N. Fejer, D. Chakrabarti, H. Kusumaatmaja and D. J. Wales, *Nanoscale*, 2014, **6**, 9448–9456.

[61] J. D. Bernal, *Proc. R. Soc. Lond. A*, 1964, **280**, 299–322.

[62] K. L. Thompson, M. Williams and S. P. Armes, *J. Colloid Interface Sci.*, 2014, **447**, 217–228.

[63] A. D. Dinsmore, M. F. Hsu, M. G. Nikolaides, M. Marquez, A. R. Bausch and D. A. Weitz, *Science*, 2002, **298**, 1006–1009.

[64] A. W. Wilber, J. P. K. Doye, A. A. Louis, E. G. Noya, M. A. Miller and P. Wong, *J. Chem. Phys.*, 2007, **127**, 1–12.

[65] A. W. Wilber, J. P. K. Doye and A. A. Louis, *J. Chem. Phys.*, 2009, **131**, 175101.

[66] D. Morphew and D. Chakrabarti, *Nanoscale*, 2015, **18**, 8343–8350.

[67] C. H. J. Evers, J. a. Luiken, P. G. Bolhuis and W. K. Kegel, *Nature*, 2016, **534**, 364–368.

[68] D. Morphew and D. Chakrabarti, *Soft Matter*, 2016, **12**, 9633–9640.

[69] D. L. Caspar and A. Klug, *Cold Spring Harb. Symp. Quant. Biol.*, 1962, **27**, 1–24.

[70] R. P. Sear, *J. Chem. Phys.*, 1999, **111**, 4800–4806.

[71] E. G. Teich, G. V. Anders, D. Klotsa, J. Dshemuchadse and S. C. Glotzer, *Proc. Natl. Acad. Sci.*, 2015, **I**, 1–10.

[72] A. B. Hopkins, F. H. Stillinger and S. Torquato, *J. Math. Phys.*, 2010, **51**, 043302.

[73] A. B. Hopkins, F. H. Stillinger and S. Torquato, *Phys. Rev. E - Stat. Nonlinear, Soft Matter Phys.*, 2011, **83**, 011304.

[74] J. Yan, M. Bloom, S. C. Bae, E. Luijten and S. Granick, *Nature*, 2012, **491**, 578–582.

[75] J. J. Crassous, A. M. Mihut, E. Wernersson, P. Pfleiderer, J. Vermant, P. Linse and P. Schurtenberger, *Nat. Commun.*, 2014, **5**, 5516.

[76] P. N. Pusey and W. van Megen, *Nature*, 1986, **320**, 340–342.

[77] P. N. Pusey, E. Zaccarelli, C. Valeriani, E. Sanz, W. C. K. Poon and M. E. Cates, *Philos. Trans. R. Soc. A Math. Phys. Eng. Sci.*, 2009, **367**, 4993–5011.

[78] B. J. Alder and T. E. Wainwright, *J. Chem. Phys.*, 1957, **27**, 1208–1209.

[79] W. W. Wood and J. D. Jacobson, *J. Chem. Phys.*, 1957, **27**, 1207–1208.

[80] S. Auer and D. Frenkel, *Nature*, 2001, **409**, 1020–1023.

[81] S. Auer and D. Frenkel, *Nature*, 2001, **413**, 711–713.

[82] U. Gasser, *Science*, 2001, **292**, 258–262.

[83] M. S. Elliot, S. B. Haddon and W. C. Poon, *J. Phys. Condens. Matter*, 2001, **13**, L553–L558.

[84] R. P. Sear, *J. Phys.: Condens. Matter*, 2007, **19**, 033101.

[85] Z. Zhang, A. S. Keys, T. Chen and S. C. Glotzer, *Langmuir*, 2005, **21**, 11547–11551.

[86] E. G. Noya, C. Vega, J. P. Doye and A. A. Louis, *J. Chem. Phys.*, 2010, **132**, 234511.

[87] J. P. K. Doye, A. A. Louis, I.-C. Lin, L. R. Allen, E. G. Noya, A. W. Wilber, H. C. Kok and R. Lyus, *Phys. Chem. Chem. Phys.*, 2007, **9**, 2197.

[88] I. Saika-Voivod, F. Smallenburg and F. Sciortino, *J. Chem. Phys.*, 2013, **139**, 234901.

[89] F. Romano, E. Sanz and F. Sciortino, *J. Chem. Phys.*, 2010, **132**, 184504.

[90] G. Doppelbauer, E. G. Noya, E. Bianchi and G. Kahl, *J. Phys. Condens. Matter*, 2012, **24**, 284124.

[91] E. Bianchi, G. Doppelbauer, L. Filion, M. Dijkstra and G. Kahl, *J. Chem. Phys.*, 2012, **136**, 214102.

[92] F. Romano and F. Sciortino, *Nat. Commun.*, 2012, **3**, 975.

[93] Z. Gong, T. Hueckel, G.-R. Yi and S. Sacanna, *Nature*, 2017.

[94] Q. Chen, S. C. Bae and S. Granick, *Nature*, 2011, **469**, 381–384.

[95] Z. He and I. Kretzschmar, *Langmuir*, 2013, **29**, 15755–15761.

[96] F. Romano and F. Sciortino, *Nat. Mater.*, 2011, **10**, 171–173.

[97] Q. Chen, S. C. Bae and S. Granick, *J. Am. Chem. Soc.*, 2012, **134**, 11080–11083.

[98] K. Miszta, J. de Graaf, G. Bertoni, D. Dorfs, R. Brescia, S. Marras, L. Ceseracciu, R. Cingolani, R. van Roij, M. Dijkstra and L. Manna, *Nat. Mater.*, 2011, **10**, 872–876.

[99] M. Grunwald and P. L. Giessler, *ACS Nano*, 2014, **8**, 5891–5897.

[100] J. T. McGinley, I. C. Jenkins, T. Sinno and J. C. Crocker, *Soft Matter*, 2013, **9**, 9119.

[101] J. T. McGinley, Y. Wang, I. C. Jenkins, T. Sinno and J. C. Crocker, *ACS Nano*, 2015, **9**, 10817–10825.

[102] M. B. Zanjani, I. C. Jenkins, J. C. Crocker and T. Sinno, *ACS Nano*, 2016, **10**, 11280–11289.

[103] A.-P. Hynninen, J. H. J. Thijssen, E. C. M. Vermolen, M. Dijkstra and A. van Blaaderen, *Nat. Mater.*, 2007, **6**, 202–205.

[104] G. Avvisati, T. Dasgupta and M. Dijkstra, *ACS Nano*, 2017, **11**, 7702–7709.

[105] É. Ducrot, M. He, G.-R. Yi and D. J. Pine, *Nat. Mater.*, 2017, **16**, 652–657.

[106] Y. Wang, I. C. Jenkins, J. T. McGinley, T. Sinno and J. C. Crocker, *Nat. Commun.*, 2017, **8**, 14173.

[107] *Advanced Computer Simulation Approaches for Soft Matter Sciences*, ed. C. Holm and K. Kremer, Springer-Verlag, Berlin Heidelberg, 2005, vol. I-III.

[108] S. M. Woodley and C. R. A. Catlow, *Phys. Chem. Chem. Phys.*, 2014, DOI: 10.1039/c4cp90126f.

[109] C. N. Likos, *Riv. Del Nuovo Cim.*, 2014, **37**, 124–180.

[110] B. Derjaguin and L. Landau, *Acta Physico Chemica URSS*, 1941, **14**, 633–662.

[111] *Theory of the stability of lyophobic colloid*, ed. E. J. W. Verwey and J. T. G. Overbeek, Elsevier, Amsterdam, 1948.

[112] M. O. Robbins, K. Kremer and G. S. Grest, *J. Chem. Phys.*, 1988, **88**, 3286–3312.

[113] S. Hamaguchi, R. T. Farouki and D. H. E. Dubin, *Phys. Rev. E*, 1997, **56**, 4671–4682.

[114] E. J. Meijer and F. E. Azhar, *J. Chem. Phys.*, 1996, **106**, 4678–4683.

[115] F. El Azhar, M. Baus, J.-P. Ryckaert and E. J. Meijer, *J. Chem. Phys.*, 2000, **112**, 5121.

[116] A.-P. Hynninen and M. Dijkstra, *Phys. Rev. E*, 2003, **68**, 021407.

[117] Y. Monovoukas and A. P. Gast, *J. Colloid Interface Sci.*, 1989, **128**, 533–548.

[118] E. B. Sirota, H. D. Ou-Yang, S. K. Sinha, P. M. Chaikin, J. D. Axe and Y. Fujii, *Phys. Rev. Lett.*, 1989, **62**, 1524–1527.

[119] H. J. Schöpe, T. Decker, T. Palberg, T. Decker and T. Palberg, *J. Chem. Phys.*, 1998, **109**, 10068–10074.

[120] D. Chakrabarti, H. Kusumaatmaja, V. Rühle and D. J. Wales, *Phys. Chem. Chem. Phys.*, 2014, **16**, 5014–5025.

[121] H. Goldstein, C. P. Poole and J. L. Safko, *Classical Mechanics*, Addison Wesley, 2002.

[122] D. Chakrabarti *et al.*, 2014, `GlOSP`: A program for `Gl`obal `O`ptimisation for `S`tructure `P`rediction, http://stchem.bham.ac.uk/~dchakrabarti/glosp.html, accessed: January 04, 2018.

[123] D. Chakrabarti and D. J. Wales, *Phys. Chem. Chem. Phys.*, 2009, **11**, 1970–1976.

[124] W. R. Hamilton, *Proc. R. Irish Acad.*, 1844, **2**, 424–434.

[125] C. F. F. Karney, *J. Mol. Graph. Mod.*, 2007, **25**, 595–604.

[126] D. Wales, *Energy Landscapes: Applications to Clusters, Biomolecules and Glasses*, Cambridge University Press, 2003.

[127] F. H. Stillinger and T. A. Weber, *Science*, 1984, **225**, 983–989.

[128] J. T. Ngo, J. Marks and M. Karplus, in *Computational Complexity, Protein Structure Prediction, and the Levinthal Paradox*, ed. K. M. Merz and S. M. Le Grand, Birkhäuser Boston, Boston, MA, 1994, pp. 433–506.

[129] D. E. Goldberg, *Read. Addison-Wesley*, 1989.

[130] D. J. Wales and H. A. Scheraga, *Science*, 1999, **285**, 1368–1372.

[131] R. Johnston, *Dalt. Trans.*, 2003, 4193–4207.

[132] Z. Li and H. A. Scheraga, *Proc. Natl. Acad. Sci. USA*, 1987, **84**, 6611–6615.

[133] C. G. Broyden, *IMA J. Appl. Math.*, 1970, **6**, 76–90.

[134] R. Fletcher, *Comput. J.*, 1970, **13**, 317–322.

[135] D. Goldfarb, *Math. Comput.*, 1970, **24**, 23–26.

[136] D. F. Shanno, *Math. Comput.*, 1970, **24**, 647–656.

[137] D. C. Liu and J. Nocedal, *Math. Program.*, 1989, **45**, 503–528.

[138] D. Frenkel and B. Smit, *Acad. Press*, 2001.

[139] N. Metropolis, A. W. Rosenbluth, M. N. Rosenbluth, A. H. Teller and E. Teller, *J. Chem. Phys.*, 1953, **21**, 1087–1092.

[140] D. Chakrabarti *et al.*, 2014, `PaSSion`: A `Package` for `Soft` Matter `Simulation`, http://stchem.bham.ac.uk/~dchakrabarti/passion.html, accessed: January 04, 2018.

[141] J.-Y. Trosset and H. A. Scheraga, *J. Comput. Phys.*, 1999, **20**, 412–427.

[142] S. Whitelam and P. L. Geissler, *J. Chem. Phys.*, 2007, **127**, 15401.

[143] S. Whitelam, E. H. Feng, M. F. Hagan and P. L. Geissler, *Soft Matter*, 2009, **5**, 1251.

[144] Š. Růžička and M. P. Allen, *Phys. Rev. E*, 2014, **89**, 033307.

[145] Š. Růžička and M. P. Allen, *Phys. Rev. E*, 2014, **90**, 33302.

[146] R. H. Swendsen and J.-S. Wang, *Phys. Rev. Lett.*, 1987, **58**, 86–88.

[147] F. Niedermayer, *Phys. Rev. Lett.*, 1988, **61**, 2026–2029.

[148] U. Wolff, *Phys. Rev. Lett.*, 1989, **62**, 361–364.

[149] D. Wu, D. Chandler and B. Smit, *J. Phys. Chem.*, 1992, **96**, 4077–4083.

[150] J. Liu and E. Luijten, *Phys. Rev. Lett.*, 2004, **92**, 035504.

[151] J. Liu and E. Luijten, *Phys. Rev. E - Stat. Nonlinear, Soft Matter Phys.*, 2005, **71**, 1–12.

[152] T. Biyikoğlu and J. Leydold, *J. Comb. Theory. Ser. B*, 2007, **97**, 159–174.

[153] D. J. Evans, *Mol. Phys*, 1977, **34**, 317–325.

[154] G. M. Torrie and J. P. Valleau, *J. Comp. Phys.*, 1977, **23**, 187–199.

[155] S. Kumar, D. Bouzida, R. H. Swendsen, P. A. Kollman and J. M. Rosenberg, *J. Comp. Chem.*, 1992, **13**, 1011–1021.

[156] B. Roux, *Comp. Phys. Comm.*, 1995, **91**, 275–282.

[157] H. W. Kroto, J. R. Heath, S. C. O'Brien, R. F. Curl and R. E. Smalley, *Nature*, 1985, **318**, 162–163.

[158] A. Muller, *Science*, 2003, **300**, 749–750.

[159] J. Song, L. Pu, J. Zhou, B. Duan and H. Duan, *ACS Nano*, 2013, **7**, 9947–9960.

[160] C. Song, Y. Wang and N. L. Rosi, *Angew. Chemie - Int. Ed.*, 2013, **52**, 3993–3995.

[161] A. Benz, S. Campione, S. Liu, I. Montaño, J. F. Klem, A. Allerman, J. R. Wendt, M. B. Sinclair, F. Capolino and I. Brener, *Nat. Commun.*, 2013, **4**, year.

[162] L. R. MacGillivray and J. L. Atwood, *Ang. Chem. Int. Ed*, 1999, **38**, 1018–1033.

[163] A. D. Dinsmore, M. F. Hsu, M. G. Nikolaides, M. Marquez, A. R. Bausch and D. A. Weitz, *Science*, 2002, **298**, 1006–1009.

[164] Y. He, T. Ye, M. Su, C. Zhang, A. E. Ribbe, W. Jiang and C. Mao, *Nature*, 2008, **452**, 198–201.

[165] R. P. Goodman, M. Heilemann, S. Doose, C. M. Erben, A. N. Kapanidis and A. J. Turberfield, *Nature Nanotechnology*, 2008, **3**, 93–96.

[166] A. W. Wilber, J. P. K. Doye, A. A. Louis and A. C. F. Lewis, *J. Chem. Phys.*, 2009, **131**, 175102.

[167] G. M. Whitesides and M. Boncheva, *Proc. Natl. Acad. Sci.*, 2002, **99**, 4769–4774.

[168] S. Sacanna, M. Korpics, K. Rodriguez, L. Colón-Meléndez, S.-H. Kim, D. J. Pine and G.-R. Yi, *Nat. Commun.*, 2013, **4**, 1688.

[169] Y. Min, M. Akbulut, K. Kristiansen, Y. Golan and Y. Israelachvili, *Nat. Mater.*, 2008, **7**, 527–538.

[170] V. N. Manoharan and D. J. Pine, *MRS Bull.*, 2004, **29**, 91–95.

[171] M. A. Miller and D. J. Wales, *J. Phys. Chem. B*, 2005, **109**, 23109–23112.

[172] Z. Zhang and S. C. Glotzer, *Nano. Lett.*, 2004, **44**, 1407–1413.

[173] E. G. Noya, C. Vega, J. P. K. Doye and A. A. Louis, *J. Chem. Phys.*, 2010, **132**, 234511.

[174] K. Van Workum and J. F. Douglas, *Phys. Rev. E - Stat. Nonlinear, Soft Matter Phys.*, 2006, **73**, 1–17.

[175] A. Baskin, W.-Y. Lo and P. Kral, *ACS Nano*, 2012, **6**, 6083–6090.

[176] S. Sacanna, L. Rossi and D. J. Pine, *J. Am. Chem. Soc.*, 2012, **134**, 6112–6115.

[177] A. Yethiraj and A. van Blaaderen, *Nature*, 2003, **421**, 513–517.

[178] L. H. M. Wang and Y. Yin, *Mater. Today*, 2013, **16**, 110–116.

[179] J. Yan, K. Chaudhary, S. C. Bae, J. A. Lewis and S. Granick, *Nat. Commun.*, 2013, **4**, 1516.

[180] R. M. Erb, H. S. Son, B. Samanta, V. M. Rotello and B. B. Yellen, *Nature*, 2009, **457**, 999–1002.

[181] J. E. Martin, R. A. Anderson and C. P. Tigges, *J. Chem. Phys*, 1998, **108**, 7787–7890.

[182] J. E. Martn, E. Venturini, G. L. Gulley and J. Williamson, *Phys. Rev. E*, 2004, **69**, 21508.

[183] L. Rovigatti, J. Russo and F. Sciortino, *Phys. Rev. Lett*, 2011, **107**, 237801.

[184] A. P. Hynninen and M. Dijkstra, *Phys. Rev. Lett*, 2005, **94**, 138303.

[185] A. P. Hynninen and M. Dijkstra, *Phys. Rev. E*, 2005, **72**, 51402.

[186] V. Malik, A. V. Petukhov, L. He, Y. Yin and M. Schmidt, *Langmuir*, 2012, **28**, 14777–14783.

[187] G. M. P. Keim and H. H. von Grunberg, *Phys. Rev. E*, 2007, **75**, 31402.

[188] L. Baraban, D. Makarov, M. Albrecht, N. Rivier, P. Liederer and A. Ebe, *Phys. Rev. E*, 2008, **77**, 31407.

[189] S. K. Smoukov, S. Gangwal, M. Marquez and O. D. Velev, *Soft Matter*, 2009, **5**, 1285–1292.

[190] P. Tierno, *Phys. Chem. Chem. Phys.*, 2014.

[191] P. R. Cromwell, *(Cambridge Univ. Press. Cambridge, 1997)*.

[192] S. Kantorovich, R. Weeber, J. J. Cerda and C. Holm, *Soft Matter*, 2011, **7**, 5217–5227.

[193] B. G. P. van Ravensteijn, M. Kamp, A. van Blaaderen and W. K. Kegel, *Chem. Mater.*, 2013, **25**, 4348–4353.

[194] C. N. Likos, *Phys. Rep.*, 2001, **348**, 267–439.

[195] D. N. Theodorou and U. W. Suter, *Macromolecules*, 1985, **18**, 1206–1214.

[196] M. J. G. Meriguet and P. Turq, *J. Chem. Phys.*, 2004, **121**, 6078–6085.

[197] S. L. Tripp, R. E. Dunin-Borkowski and A. Wei, *Angew. Chemie Int. Ed.*, 2003, **42**, 5591–5593.

[198] A. I. Abrikosov, S. Sacanna, A. P. Philipse and P. Linse, *Soft Matter*, 2013, **9**, 8904–8913.

[199] L. Rossi, J. G. Donaldson, J.-M. Meijer, A. V. Petukhov, D. Kleckner, S. S. Kantorovich, W. T. M. Irvine, A. P. Philipse and S. Sacanna, *Soft Matter*, 2018, **14**, 1080–1087.

[200] E. Sanz and D. Marenduzzo, *J. Chem. Phys.*, 2010, **132**, 194102.

[201] T. Autenrieth, A. Robert, J. Wagner and G. Grubel, *J. Appl. Crystallogr.*, 2007, **40**, 250–253.

[202] S. Whitelam and P. L. Geissler, *J. Chem. Phys.*, 2007, **127**, 15401.

[203] D. N. Theodorou and U. W. Suter, 1985, **6**, 1206–1214.

[204] M. F. Hagan, O. M. Elrad and R. L. Jack, *J. Chem. Phys.*, 2011, **135**, 104115.

[205] J. J. Juarez and M. A. Bevan, *Adv. Funct. Mater.*, 2012, **22**, 3833–3839.

[206] D. Klotsa and R. L. Jack, *J. Chem. Phys*, 2013, **138**, 94502.

[207] L. Di Michele, F. Varrato, J. Kotar, S. H. Nathan, G. Foffi and E. Eiser, *Nat. Commun.*, 2013, **4**, 1–7.

[208] F. Li, D. P. Josephson and A. Stein, *Angew. Chemie - Int. Ed.*, 2011, **50**, 360–388.

[209] J. Zhang, E. Luijten and S. Granick, *Annu. Rev. Phys. Chem.*, 2015, **66**, 581–600.

[210] P. Fratzl and R. Weinkamer, *Prog. Mater. Sci.*, 2007, **52**, 1263–1334.

[211] S. Whitelam and R. L. Jack, *Annu. Rev. Phys. Chem.*, 2015, **66**, 143–163.

[212] W. M. Jacobs and D. Frenkel, *J. Am. Chem. Soc.*, 2016, **138**, 2457–2467.

[213] Y. Hsia, J. B. Bale, S. Gonen, D. Shi, W. Sheffler, K. K. Fong, U. Nattermann, C. Xu, P.-S. Huang, R. Ravichandran, S. Yi, T. N. Davis, T. Gonen, N. P. King and D. Baker, *Nature*, 2016, 1–12.

[214] A. I. Abrikosov, S. Sacanna, A. P. Philipse and P. Linse, *Soft Matter*, 2013, **9**, 8904.

[215] M. Klinkigt, R. Weeber, S. Kantorovich and C. Holm, *Soft Matter*, 2013, **9**, 3535.

[216] A. B. Yener and S. H. L. Klapp, *Soft Matter*, 2016, **12**, 2066–2075.

[217] J. Yan, S. C. Bae and S. Granick, *Adv. Mater.*, 2015, **27**, 874–879.

[218] T. K. Haxton and S. Whitelam, *Soft Matter*, 2013, **9**, 6851.

[219] D. J. Wales, *Mol. Phys.*, 2002, **100**, 3285–3305.

[220] G. Henkelman and H. Jónsson, *J. Chem. Phys.*, 1999, **111**, 7010–7022.

[221] S. A. Trygubenko and D. J. Wales, *J. Chem. Phys.*, 2004, **120**, 2082.

[222] L. J. Munro and D. J. Wales, *Phys. Rev. B*, 1999, **59**, 3969–3980.

[223] X. Li, *J. Graph. Tools*, 2007, **12**, 1–6.

[224] D. Lui and J. Nocedal, 1989, **45**, 503–528.

[225] J. Nocedal, *Math. Comput.*, 1980, **35**, 773–773.

[226] J. M. Carr and D. J. Wales, *J. Phys. Chem. B*, 2008, **112**, 8760–8769.

[227] D. A. Evans and D. J. Wales, *J. Chem. Phys.*, 2004, **121**, 1080–1090.

[228] E. W. Dijkstra, *Numer. Math.*, 1959, **1**, 269–271.

[229] J.-Y. Trosset and H. A. Scheraga, *J. Comput. Chem.*, 1999, **20**, 412–427.

[230] D. Chakrabarti, H. Kusumaatmaja, V. Rühle and D. J. Wales, *Phys. Chem. Chem. Phys.*, 2014, **16**, 5014–5025.

[231] S. Whitelam and R. L. Jack, *Annu. Rev. Phys. Chem.*, 2015, **66**, 143–163.

[232] W. M. Jacobs and D. Frenkel, *J. Am. Chem. Soc.*, 2016, **138**, 2457–2467.

[233] Y. Inokuma, M. Kawano and M. Fujita, *Nat. Chem.*, 2011, **3**, 349–358.

[234] N. Yanai and S. Granick, *Angew. Chem. Int. Ed.*, 2012, **51**, 5638–5641.

[235] D. Morphew and D. Chakrabarti, *Curr. Opin. Colloid Interface Sci.*, 2017, **30**, 70–80.

[236] A. H. Gröschel, A. Walther, T. I. Löbling, F. H. Schacher, H. Schmalz and A. H. E. Müller, *Nature*, 2013.

[237] Q. Chen, S. C. Bae and S. Granick, *J. Am. Chem. Soc.*, 2012, **134**, 11080–11083.

[238] M. Grünwald and P. L. Geissler, *ACS Nano*, 2014, **8**, 5891–5897.

[239] N. Vogel, S. Utech, G. T. England, T. Shirman, K. R. Phillips, N. Koay, I. B. Burgess, M. Kolle, D. a. Weitz and J. Aizenberg, *Proc. Natl. Acad. Sci.*, 2015, **112**, 201506272.

[240] D. Frenkel and D. J. Wales, *Nat. Mater.*, 2011, **10**, 410–411.

[241] R. L. Baldwin, *Nature*, 1994, **369**, 183–184.

[242] J. M. Fletcher, R. L. Harniman, F. R. H. Barnes, A. L. Boyle, A. Collins, J. Mantell, T. H. Sharp, M. Antognozzi, P. J. Booth, N. Linden, M. J. Miles, R. B. Sessions, P. Verkade and D. N. Woolfson, *Science*, 2013, **340**, 595–599.

[243] T. Douglas, *Science*, 2006, **312**, 873–875.

[244] M. F. Hagan, *Adv. Chem. Phys.*, 2014, **155**, 1–68.

[245] S. Faez, Y. Lahini, S. Weidlich, R. F. Garmann, K. Wondraczek, M. Zeisberger, M. A. Schmidt, M. Orrit and V. N. Manoharan, *ACS Nano*, 2015, **9**, 12349–12357.

[246] G. M. Torrie and J. P. Valleau, *J. Comput. Phys.*, 1977, **23**, 187–199.

[247] S. Kumar, J. M. Rosenberg, D. Bouzida, R. H. Swendsen and P. A. Kollman, *J. Comput. Chem.*, 1992, **13**, 1011–1021.

[248] B. Roux, *Comput. Phys. Commun.*, 1995, **91**, 275–282.

[249] D. Law-Hine, A. K. Sahoo, V. Bailleux, M. Zeghal, S. Prevost, P. K. Maiti, S. Bressanelli, D. Constantin and G. Tresset, *J. Phys. Chem. Lett.*, 2015, **6**, 3471–3476.

[250] W. B. Rogers, W. M. Shih and V. N. Manoharan, 2016, **1**, 16008.

[251] J. T. McGinley, Y. Wang, I. C. Jenkins, T. Sinno and J. C. Crocker, *ACS Nano*, 2015, **9**, 10817–10825.

[252] Y. Wang, Y. Wang, D. R. Breed, V. N. Manoharan, L. Feng, A. D. Hollingsworth, M. Weck and D. J. Pine, *Nature*, 2012, **491**, 51–55.

[253] T. D. Nguyen, B. A. Schultz, N. A. Kotov and S. C. Glotzer, *Proc. Natl. Acad. Sci. USA*, 2015, **112**, E3161–E3168.

[254] K. M. Ho, C. T. Chan and C. M. Soukoulis, *Phys. Rev. Lett.*, 1990, **65**, 3152–3155.

[255] M. Maldovan and E. L. Thomas, *Nat. Mater.*, 2004, **3**, 593–600.

[256] A. M. Kalsin, M. Fialkowski, M. Paszewski, S. K. Smoukov, K. J. M. Bishop and B. A. Grzybowski, *Science*, 2006, **312**, 420–424.

[257] W. Liu, M. Tagawa, H. L. Xin, T. Wang, H. Emamy, H. Li, K. G. Yager, F. W. Starr, A. V. Tkachenko and O. Gang, *Science*, 2016, **351**, 3–8.

[258] F. Smallenburg, L. Filion and F. Sciortino, *Nat. Phys.*, 2014, **10**, 653–657.

[259] F. Smallenburg and F. Sciortino, *Nat. Phys.*, 2013, **9**, 554–558.

[260] E. Bianchi, R. Blaak and C. N. Likos, *Phys. Chem. Chem. Phys.*, 2011, **13**, 6397–6410.

[261] P. J. Steinhardt, D. R. Nelson and M. Ronchetti, *Phys. Rev. B*, 1983, **28**, 784–805.

[262] P. Rein ten Wolde, M. J. Ruiz-Montero and D. Frenkel, *J. Chem. Phys.*, 1996, **104**, 9932–9947.

[263] W. Lechner and C. Dellago, *J. Chem. Phys.*, 2008, **129**, 114707.

[264] P.-L. CHAU and A. J. HARDWICK, *Mol. Phys.*, 1998, **93**, 511–518.

[265] J. Errington and P. Debenedetti, *Nature*, 2001, **409**, 318–321.

[266] S. Caravati, M. Bernasconi, T. D. Kühne, M. Krack and M. Parrinello, *Appl. Phys. Lett.*, 2007, **91**, 171906.

[267] X. Mao, Q. Chen and S. Granick, *Nat Mater*, 2013, **12**, 217–222.

[268] J. Zhang, Z. Luo, Z. Quan, Y. Wang, A. Kumbhar, D. M. Smilgies and J. Fang, *Nano Lett.*, 2011, **11**, 2912–2918.

[269] P. F. Damasceno, M. Engel and S. C. Glotzer, *ACS Nano*, 2012, **6**, 609–614.

[270] D. Li, M. Nielsen, J. Lee, C. Frandsen, J. F. Banfield and J. J. De Yoreo, *Science*, 2012, **336**, 1014–1018.